Generating and verifying entangled-itinerant microwave fields

by

H. S. Ku

B.S., National Taiwan University, 2003

A thesis submitted to the

Faculty of the Graduate School of the

University of Colorado in partial fulfillment

of the requirements for the degree of

Doctor of Philosophy

Department of Physics

2014

This thesis entitled:
Generating and verifying entangled-itinerant microwave fields
written by H. S. Ku
has been approved for the Department of Physics

_____

Prof. Konrad W. Lehnert

_____

Prof. James K. Thompson

Date _____

The final copy of this thesis has been examined by the signatories, and we find that both the content and the form meet acceptable presentation standards of scholarly work in the above mentioned discipline.

Ku, H. S. (Ph.D., Physics)

Generating and verifying entangled-itinerant microwave fields

Thesis directed by Prof. Prof. Konrad W. Lehnert

This thesis presents the experimental achievements of (1) generating entangled-microwave fields propagating on two physically separate transmission lines and (2) verifying the entangled states with efficient measurements. Shared entanglement between two parties is an essential resource for quantum information processing and quantum communication protocols. Experimentally, entangled pairs of electromagnetic fields can be realized by distributing a squeezed vacuum over two separated modes. As a result, entanglement is revealed by the strong cross-correlations between specific quadratures of the two modes. Although it is possible to verify the presence of entanglement with low-efficiency quadrature measurements, higher detection efficiencies are desired for performing protocols that exploit entanglement with high fidelity.

In the microwave regime, Josephson parametric amplifiers (JPAs) fulfill the two major tasks mentioned above: JPAs prepare the required squeezed states to generate entanglement and enable us to perform efficient quadrature measurements. Therefore, for the purposes of entanglement generation and verification, ultralow-noise–frequency-tunable JPAs have been developed. Additionally, to increase the efficiency of entanglement generation, we integrate JPAs with two on-chip microwave passive components, a directional coupler and a quadrature hybrid, to form an entangler circuit. The two-mode entangled states are created at the two output modes of the entangler and are measured with a two-channel measurement apparatus where each of the two channels incorporates a JPA as a single-quadrature preamplifier. By employing this measurement scheme, the two measured quadratures of the two output modes can be chosen independently of each other, enabling a full characterization of the two-mode state. To definitively demonstrate the two-mode entanglement, I prove that the measured quadrature variances satisfy the inseparability criterion.

Dedication

To my lovely family.

Acknowledgements

It has been a fantastic journey towards my Ph.D. in the last seven years. I would like to give my gratitude to many people for their invaluable help and support.

Foremost, I would like to thank my amazing Ph.D. advisor Prof. Konrad Lehnert. It would not be possible for me to finish this thesis and complete my Ph.D. without him. His passion and dedication to science have always encouraged me. Furthermore, I very much appreciate that he has always been patient and helpful on every question I asked. I am also thankful for his great feedback on my writings and presentations.

Besides my advisor, I would like to thank the rest of my Comps III and/or thesis committee: Prof. James Thompson, Prof. Murray Holland, Prof. Charles Rogers, Prof. Kent Irwin, and Prof. Zoya Popovic. for their insightful feedback on my work.

I appreciate all the contributions from my collaborators in NIST to the entanglement project, including the fabrication group: Kent Irwin, Gene Hilton, and Leila Vale. They have given me suggestions on my circuit designs and fabricated my devices. I want to thank Stephen Russek who has helped me on making calibrated microwave measurements. I am also grateful to the NIST theorists: Emanuel Knill and Scott Glancy. They have provided me with a deeper understanding my data and helped me to analyze my measurement results.

I have also had the pleasure to work with many great post-docs: François Mallet, John Teufel, Tobias Donner, Tauno Palomaki, Michael Schroer, and Joe Kerckhoff. They are supportive and willing to share their knowledge with me. In particular, I want to thank François Mallet who led me in the initial phase of this project.

My special thanks go out to my lab-mates Manuel Castellanos-Beltran and Will Kindel. Manuel instructed me when I joined the group and taught me how to design and operate the wonderful Josephson parametric amplifier. Will was my best partner in the lab. His brilliant ideas inspired me many times, and his friendly and fun personality makes me always enjoy my time working with him.

Additionally, I would like to thank everyone else who has been a member of Lehnert lab with me: Nathan Flowers-Jacobs, Jennifer Harlow, Scott Hoch, Reed Andrews, Adam Reed, Brad Mitchell, Mehmet Ali Anil, and Gerwin Koolstra. They all have enriched my life in the Lehnert lab.

I would also like to thank the shops staff of JILA who aided me in accomplishing my work. In particular, I owe thanks to Hans Green who helped us to construct the experimental facility and Julie Phillips who read and gave suggestions on editing this thesis.

Finally, I would like to thank my family and all my friends who have shared the frustrations and joyfulness of my Ph.D. journey.

Contents

Chapter

Tables

Table

Figures

Figure

Chapter 1

Introduction

Quantum entanglement is one of the most peculiar phenomena of quantum mechanics. When two physical systems share entanglement, a measurement on one system appears to determine the state of the other system. Entanglement originates from the principle of quantum superposition. In quantum theory, a system is allowed to be in a linear superposition of all theoretically possible states. As a result, entanglement exists when the quantum state of a composite system cannot be independently described by the individual states of the subsystems. When the system is in an entangled state, the correlations between the subsystems are stronger than any that could possibly be generated by classical means.

In 1935, the notion of the entanglement appeared in the famous paper published by Einstein, Podolsky, and Rosen (EPR) [1] to identify the incompleteness of the quantum theory. They showed that the strong correlations possessed by the EPR entangled states violate the local realist view of causality, thus arguing that quantum mechanics was an incomplete theory. For the next 30 years, this argument seemed to be a purely philosophical debate, as one could recover the local realist view of causality by the unappealing introduction of hidden variables. In 1964, however, Bell derived an inequality that all local realistic models, including hidden variables theories, have to obey [2]. Since then, there have been many experimental studies of entangled systems yielding results that are inconsistent with local realism but consistent with orthodox quantum mechanics.

Recently, entanglement has been recognized as an important resource for quantum information processing [3, 4, 5]. When two parties share entanglement, many powerful quantum com-

munication protocols are available to them. For example, they may communicate with security guaranteed by physical laws [6, 7, 8], they may encode data more densely than classical bounds [9, 10, 11], and they may create entanglement between two parties that never interact with each other [12, 13, 14, 15]. Moreover, one party can transfer a quantum state to another by transmitting only classical information, a protocol known as quantum teleportation [16, 17, 18]. The teleportation protocol can even be extended to realize error-correction schemes [19, 20, 21]. Shared entanglement also has a potential application in building a general quantum information processor that is structured as a distributed machine comprising many well-isolated copies of a high-fidelity quantum register [22, 23].

EPR-type entanglement can be implemented by utilizing the wave properties of electromagnetic fields [24]. In the EPR paper, the correlations lie in the continuous basis of the position and momentum of particles. The quadrature amplitudes of electromagnetic fields, which are the sine and cosine components of oscillating waves, are analogous to those continuous variables of particles. One can harness the wave-like continuous nature of electromagnetic fields for quantum information processing. To implement this so-called continuous-variable approach of quantum information processing, the squeezed state of an electromagnetic mode, a state which has less uncertainty than the vacuum fluctuation in one of its quadratures, is the key ingredient. Another important technique is the ability to perform efficient measurements on the quadratures of quantum states.

The field of continuous-variable quantum information processing using propagating light fields has made remarkable achievements. In optics, the squeezed state of light can be generated in an on-demand fashion by parametric down-conversion [25, 26, 27, 28]. Furthermore, the required measurements can be performed using efficient photodetectors [29]. Thanks to these useful experimental techniques, squeezed state generation [30, 31], quantum state tomography [32, 33, 34], entanglement generation [35, 36, 37], quantum teleportation [38, 39], and error correction [40, 41, 42] have all been demonstrated with optical fields.

At microwave frequencies, the field is less advanced because of the more recent development of efficient measurement schemes. The parametric amplification process was first investigated

in electrical circuits by Yurke for efficient microwave amplification and therefore measurements [43, 44, 45, 46]. Here the necessary nonlinearity for having the parametric gain is provided by superconducting Josephson junctions [47]. Because of the successful development of quantum information processing with superconducting circuits [48, 49], the interest in developing quantum-limited microwave measurements has been growing rapidly in the past few years. Efficient measurements with Josephson junctions based parametric amplifiers have recently been implemented in many experimental groups [50, 51, 52, 53, 54, 55, 56] and shown to improve the signal-to-noise ratio for readout of microwave-frequency superconducting quantum bits (qubits) [57, 58, 59, 60, 61, 62]. Ultralow-noise microwave measurements are desirable for a variety of applications such as for nanomechanical resonators [63, 64, 65], magnetometry [66, 67], quantum feedback [68, 69, 70, 71], the search for dark matter (axions) [72], and detection schemes in astrophysics [73]. Furthermore, parametric devices can also be used to process quantum noise for generating squeezed states [46, 53, 74] that are the primary resources for generating entanglement [4].

Entanglement between physically distinct itinerant microwave modes has been an important subject of recent experimental studies [75, 76, 77, 78]. In microwave-superconducting qubit circuits, the quantum registers that have the longest coherence time are built from centimeter-sized microwave cavities containing a few qubits [79]. Itinerant microwave modes are the media by which one can establish and exploit entanglement among such registers. Moreover, on the way to pursuing propagating-microwave entanglement, we also master the manipulation and measurement of itinerant microwave fields.

In this work, I generate a two-mode entangled state by combining a quadrature-squeezed state and vacuum on a microwave hybrid. The input squeezed state is prepared by squeezing quantum noise with a Josephson parametric amplifier (JPA). The output state that emerges at the two output ports of the hybrid is a two-mode entangled state. This entanglement can be distributed to two distant parties who perform quantum-communication protocols using shared entanglement.

I verify the presence of entanglement by performing single-quadrature measurements simultaneously on the two separate modes. While it is possible to verify the presence of entanglement with

low efficiency measurements [80, 81, 82, 83, 84], to perform quantum protocols such as teleportation or error correction requires a high detection efficiency [38, 85]. I improve my measurement quantum efficiencies by employing two JPAs as ultralow-noise preamplifiers for the two amplifier chains of the two measurement channels. Moreover, by comparing this efficient measurement apparatus to the measurement scheme used in [75], the measurement bases (which are the quadrature phases of the two modes in our measurement scheme) can be independently chosen. This independent control ability allows us to fully characterize the two-mode state. With the aid of JPAs, we definitively demonstrate entanglement with suitable entanglement criteria [86, 87, 88] without correcting for measurement inefficiencies.

Thesis overview

In this thesis, I present two major experimental achievements on developing microwave quantum information processing. The first experiment is a quantum tomography of microwave-squeezed states [89]. In the tomography experiment, by using the JPAs, we demonstrate both the squeezed state generation and the quantum state measurements. I then combine the necessary microwave passive components [90] with noise-improved JPAs to perform the microwave two-mode entanglement experiment [91].

The thesis is organized as follows: In chapter 2, I review the basic quantum-optics theory with an emphasis on the continuous-variable formalism. I start with the introduction of the quantized-electromagnetic fields and then describe the theory for manipulating the quantum states of electromagnetic fields. I also discuss the theory of a two-mode entanglement for a continuous variable system and the associated entanglement criteria. In chapter 3, I provide a quantum description of the JPAs. I first review the basic Josephson junction theory. I then discuss the quantum formalism of the electrical circuit. Following that, I explain the operations of the JPAs in the formalism of the input-output theory. In chapter 4, I present my work on designing and testing of two microwave passive components, a 20 dB directional coupler and a quadrature hybrid. These two passive components are integrated with the JPAs to form a chip for generating the two-mode

entangled state. In chapter 5, I present our noise-improved designs of JPAs to be incorporated in the two-mode entanglement experiment. In chapter 6, I present squeezed state tomography. In this experiment, the squeezed state generated by a JPA is measured by a microwave amplifier chain that employs a JPA as the preamplifier. I then apply the maximum-likelihood method to reconstruct a quantum phase-space representation of the state, called the Wigner function of the squeezed state. In chapter 7, I present our work of creating entanglement between two physically separate transmission lines. The generated entangled state is measured with a two-channel efficient microwave quadrature measurement apparatus, which allows me to directly observe the fulfillment of the entanglement criterion without correcting for the measurement inefficiencies. Finally, I conclude this thesis in chapter 8 by suggesting future directions for developing microwave quantum information processing.

Chapter 2

Continuous-variable quantum optics

When quantizing classical electromagnetism, the electromagnetic field is described as a collection of quantum harmonic oscillators indexed by their oscillation frequencies. The oscillation energy in each mode is quantized, and the excitations per mode are discrete entities called photons. One natural description of the field is to represent its state with the number of excitations in each oscillating mode. This representation is useful for the experiments where photon-number resolving detectors are available. However, in the case of measuring large photon numbers or microwave photons, it is a technical challenge to implement such photon-counting devices. A more appropriate representation for these situations uses the field variables, such as quadrature amplitudes of the electromagnetic fields, as quantum observables. These field observables have continuous, rather than discrete, eigenvalues. Although they are not discrete, their quantum properties are exhibited by their fluctuations, which are limited by the Heisenberg uncertainty principle.

In this chapter, I introduce the quantum optics theory focused on the description with continuous variables. In the first part, I present the definitions of the quadrature operators and introduce various basic quantum states of electromagnetic fields. Following that I introduce the so-called Wigner function representation of the quantum states, which is an experimentally useful representation. In the second part, I describe the basic devices that enable us to prepare quantum states, to perform linear operations, and to make measurements. Finally, I explain the scheme I use to generate two-mode entangled states, which have quantum correlations between field observables, and discuss the criteria used to verify such entangled states.

2.1 Introduction to continuous-variable quantum optics

Continuous-variable quantum optics describes the states of electromagnetic fields in terms of continuous quadrature observables [4]. These quadrature observables of electromagnetic fields are mathematically equivalent to the position and momentum observables of a mechanical oscillator. Because the primary schemes for measuring microwave fields use linear amplifiers to measure quadrature amplitudes [49], the continuous variable description is particularly useful for conducting experiments with microwave fields. In this section, I introduce the quantum description of electromagnetic fields with an emphasis on the formalism with continuous quadrature variables. I first briefly review the definitions of quadrature operators. Second I discuss various important quantum states that have distinct noise distributions of the quadrature variables. Finally, I explain how to use a mathematical function to represent these quantum states.

2.1.1 Quadrature operators

Consider a noninteracting quantized-electromagnetic field; its Hamiltonian can be written in the form [92]

$$\hat{H} = \sum_{k=1}^{N} \hat{H}_k = \sum_{k=1}^{N} \hbar\omega_k(\hat{a}_k^\dagger \hat{a}_k + \frac{1}{2}), \tag{2.1}$$

which describes a system of N quantum harmonic oscillator modes with mode index k. Here, $\hat{a}_k$ and $\hat{a}_k^\dagger$ are the annihilation and the creation operators of one photon in mode k, and they obey the bosonic commutation relations:

$$[\hat{a}_k, \hat{a}_{k'}^\dagger] = \delta_{kk'}, \quad [\hat{a}_k, \hat{a}_{k'}] = [\hat{a}_k^\dagger, \hat{a}_{k'}^\dagger] = 0. \tag{2.2}$$

The Hermitian product $\hat{a}_k^\dagger \hat{a}_k$ is the number operator $\hat{n}_k$, and its eigenstates are labeled $|n_k\rangle$, where

$$\hat{n}_k |n_k\rangle = n_k |n_k\rangle \tag{2.3}$$

constitute a basis of the Hilbert space $\mathcal{H}_k$, and where n_k denotes the number of photons in the mode k. Apparently, the number state $|n_k\rangle$ is also the energy eigenstate with an energy eigenvalue $E_{n_k} = \hbar\omega_k(n_k + 1/2)$. For each mode k, there exists a lowest-energy state $|0_k\rangle$ such that $\hat{a}_k |0_k\rangle = 0$.

The state $|0_k\rangle$ is called the vacuum state, and it has the lowest-energy eigenvalue $\hbar\omega_k/2$. Any number state $|n_k\rangle$ can then be generated by the repeated action of the creation operator $\hat{a}_k^\dagger$ on the vacuum. Although the number state has a well-defined photon energy, it is not a state of a well-defined electric field. Consequently, the phase of the field for the number state is randomly distributed, as illustrated in Fig. 2.1(a).

From the experimental point of view, in the frequency range where photodetectors are available, the number-state basis can be a proper formalism to describe an electromagnetic field. However, at microwave frequencies, such photo-counting devices are difficult to implement [93]. Instead of measuring photon numbers, quadrature amplitudes are easier to measure with the aid of a linear amplifier. Therefore, we use the two quadrature amplitudes x and y as the experimental observables. They are eigenvalues of the quadrature operators $\hat{X}$ and $\hat{Y}$ defined as [1]

$$\hat{X} = \frac{1}{\sqrt{2}}(\hat{a} + \hat{a}^\dagger), \tag{2.4}$$

$$\hat{Y} = \frac{1}{\sqrt{2}i}(\hat{a} - \hat{a}^\dagger). \tag{2.5}$$

Essentially, the two Hermitian operators $\hat{X}$ and $\hat{Y}$ are the dimensionless position and momentum of a mechanical oscillator. The physical concept of the quadrature amplitudes can be illuminated by looking at a single-mode-noninteracting electric-field operator at a specific position in space in the Heisenberg picture (for a single polarization):

$$\hat{E}(t) = E_0(\hat{a}\mathrm{e}^{-i\omega t} + \hat{a}^\dagger \mathrm{e}^{i\omega t}), \tag{2.6}$$

$$= \sqrt{2}E_0(\hat{X}\cos(\omega t) + \hat{Y}\sin(\omega t)), \tag{2.7}$$

where E_0 is a prefactor having the dimension of a electric field. It is apparent that the operators $\hat{X}$ and $\hat{Y}$ represent the in-phase and out-of-phase quadrature amplitudes of the single-mode field with respect to a classical reference wave $\cos(\omega t)$, respectively. The choice of the reference wave is arbitrary. Generally, the electric field operator can be written as

$$\hat{E}(t) = \sqrt{2}E_0(\hat{X}_\theta \cos(\omega t - \theta) + \hat{Y}_\theta \sin(\omega t - \theta)), \tag{2.8}$$

[1] From now on, I will drop the index k for the discussion of a single-mode field.

where the operators $\hat{X}_\theta$ and $\hat{Y}_\theta$ are

$$\hat{X}_\theta = \frac{1}{\sqrt{2}}(\hat{a}\mathrm{e}^{-i\theta} + \hat{a}^\dagger \mathrm{e}^{i\theta}), \tag{2.9}$$

$$\hat{Y}_\theta = \frac{1}{\sqrt{2}i}(\hat{a}\mathrm{e}^{-i\theta} - \hat{a}^\dagger \mathrm{e}^{i\theta}), \tag{2.10}$$

with quadrature phase $\theta \in [0, \pi]$. These general quadrature operators are rotations of the operators $\hat{X}$ and $\hat{Y}$

$$\begin{pmatrix} \hat{X}_\theta \\ \hat{Y}_\theta \end{pmatrix} = \begin{pmatrix} \cos\theta & \sin\theta \\ -\sin\theta & \cos\theta \end{pmatrix} \begin{pmatrix} \hat{X} \\ \hat{Y} \end{pmatrix}, \tag{2.11}$$

in quadrature phase space. Therefore, I refer to $\hat{X}_\theta$ and $\hat{Y}_\theta$ as the rotated quadrature operators.

As I have mentioned before, the two quadrature observables x and y have continuous spectra, and their quantum behaviors are due to the fact that they are a pair of canonically conjugate variables. The operators $\hat{X}$ and $\hat{Y}$ (as well as $\hat{X}_\theta$ and $\hat{Y}_\theta$) obey the canonical commutation relation

$$[\hat{X}, \hat{Y}] = i. \tag{2.12}$$

As a result, quantum mechanics places a limit on the accuracy of a simultaneous measurement of the two quadrature amplitudes according to the corresponding Heisenberg uncertainty principle

$$\langle (\Delta\hat{X})^2 \rangle \langle (\Delta\hat{Y})^2 \rangle \geq \frac{1}{4}, \tag{2.13}$$

where $\langle (\Delta\hat{O})^2 \rangle$ is the variance of a operator $\hat{O}$ defined as: $\langle (\Delta\hat{O})^2 \rangle = \langle (\hat{O} - \langle \hat{O} \rangle)^2 \rangle = \langle \hat{O}^2 \rangle - \langle \hat{O} \rangle^2$, with $\langle \hat{O} \rangle$ representing the expectation value of the operator $\hat{O}$.

With Eqs. (2.4)–(2.5), the expectation values of quadrature amplitudes and quadrature variances of a vacuum state can be calculated to be

$$\langle \hat{X} \rangle_{\mathrm{vac}} = \langle \hat{Y} \rangle_{\mathrm{vac}} = 0, \tag{2.14}$$

$$\langle (\Delta\hat{X})^2 \rangle_{\mathrm{vac}} = \langle (\Delta\hat{Y})^2 \rangle_{\mathrm{vac}} = \tfrac{1}{2}. \tag{2.15}$$

As expected, the vacuum state has zero average values and uniform fluctuations over all quadrature phases. Thus, I can pictorially represent a vacuum state as a filled circle centered at the origin in an $X-Y$ plane called phase space [Fig. 2.1(b)]. Furthermore, the vacuum fluctuation balances the uncertainty product [Eq. (2.13)], and the vacuum state has the minimum uncertainty.

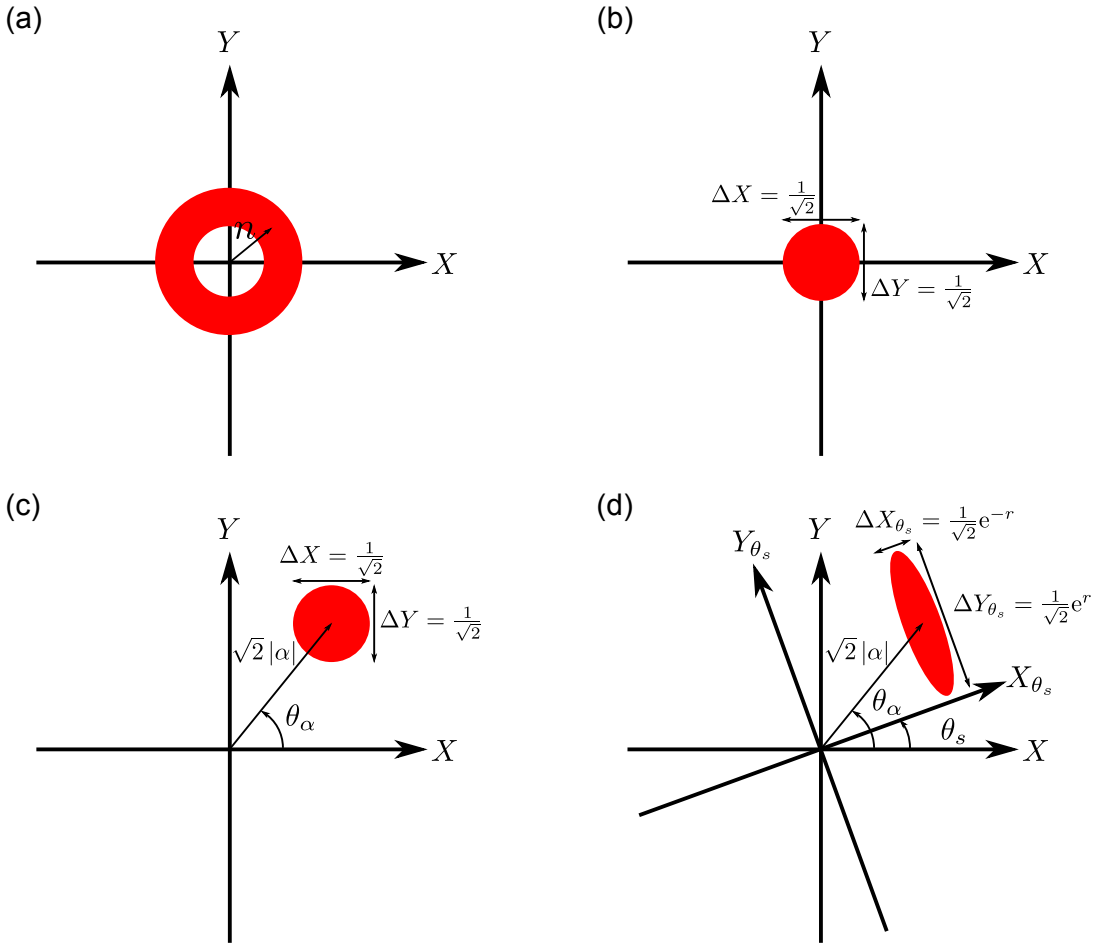

Figure 2.1: Phase-space portraits of various quantum states. Quantum states of electromagnetic fields can be graphically represented on the (X, Y) phase planes with the color area representing uncertainty. (a) A number state $|n\rangle$ is represented as a circle of radius n, where the uncertainty in n is zero but the uncertainty in phase is 2π. (b) A vacuum state $|0\rangle$ is represented as a color-filled circle centered at origin. The uncertainty is equal in any quadrature direction. (c) A coherent state $|\alpha\rangle$ is represented with a displaced vacuum circle. (d) A displaced-squeezed vacuum state $|\alpha, \zeta\rangle$ is represented with a displaced ellipse where the major and minor axes represent the amplified and squeezed quadratures, respectively.

2.1.2 Quantum states of electromagnetic fields

After introducing the number state and the quadrature operators, I present two more sets of important quantum states of electromagnetic fields: the coherent state and the squeezed state. I also introduce the density operator for describing an ensemble of states and discuss the thermal state as an example of using the density operator.

Coherent state

A classical-like state of a harmonic oscillator is the eigenstate of the annihilation operator, which is called the coherent state $|\alpha\rangle$ [94] in which

$$\hat{a}\,|\alpha\rangle = \alpha\,|\alpha\rangle\,, \tag{2.16}$$

where α is an arbitrary complex number. The expectation values of quadrature amplitudes and quadrature variances of the coherent state can be calculated as

$$\langle\hat{X}\rangle_\alpha = \sqrt{2}\mathrm{Re}(\alpha), \quad \langle\hat{Y}\rangle_\alpha = \sqrt{2}\mathrm{Im}(\alpha), \tag{2.17}$$

$$\langle(\Delta\hat{X})^2\rangle_\alpha = \langle(\Delta\hat{Y})^2\rangle_\alpha = \tfrac{1}{2}. \tag{2.18}$$

It is shown that the coherent state has an average amplitude $\sqrt{2}\,|\alpha|$ and the same fluctuation as the vacuum. Thus, a coherent state can be viewed as a vacuum state displaced by a magnitude $\sqrt{2}\,|\alpha|$ in the phase space [Fig. 2.1(c)]. Theoretically, the coherent state is generated by the unitary displacement operator $\hat{D}(\alpha) = \mathrm{e}^{\alpha\hat{a}^\dagger - \alpha^*\hat{a}}$ acting on vacuum

$$|\alpha\rangle = \hat{D}(\alpha)\,|0\rangle\,. \tag{2.19}$$

The reason $\hat{D}(\alpha)$ is a displacement operator can be seen from its effect on the annihilation and creation operators

$$\hat{D}^\dagger(\alpha)\hat{a}\hat{D}(\alpha) = \hat{a} + \alpha, \tag{2.20}$$

$$\hat{D}^\dagger(\alpha)\hat{a}^\dagger\hat{D}(\alpha) = \hat{a}^\dagger + \alpha^*, \tag{2.21}$$

indicating that the displacement operator displaces $\hat{a}$ by the complex number α. The coherent states have many interesting properties that have been extensively discussed in the literature [95, 96]. An

important feature is that coherent states are the closest quantum approximation to the classical notion of a spectrally pure sinusoidal wave. Moreover, coherent states can be naturally generated from experiments, because the steady state of a driven-damped harmonic oscillator, when the oscillator loses energy to a zero-temperature bath, surprisingly is a pure coherent state.

Squeezed state

Another important set of nonclassical states are squeezed states, which are states that have less uncertainty than vacuum fluctuation in one quadrature, at the expense of exhibiting enhanced noise in the other quadrature. Similar to the coherent states, a squeezed vacuum state can be generated by applying the unitary squeezing operator $\hat{S}(\zeta) = \mathrm{e}^{\frac{1}{2}(\zeta^* \hat{a}^2 - \zeta \hat{a}^{\dagger 2})}$ on a vacuum state

$$|\zeta\rangle = \hat{S}(\zeta)\,|0\rangle\,, \tag{2.22}$$

where $\zeta = r\mathrm{e}^{i2\theta_s}$. The squeezing parameter r determines the amount of the variance reduction in the squeezed quadrature whose direction is defined by the angle θ_s [Fig. 2.1(d)]. The squeezing operator $\hat{S}$ yields the transformation on the annihilation and creation operators

$$\hat{S}^\dagger(\zeta)\hat{a}\hat{S}(\zeta) = \hat{a}\cosh r - \hat{a}^\dagger \mathrm{e}^{i2\theta_s}\sinh r, \tag{2.23}$$

$$\hat{S}^\dagger(\zeta)\hat{a}^\dagger\hat{S}(\zeta) = \hat{a}^\dagger\cosh r - \hat{a}\mathrm{e}^{-i2\theta_s}\sinh r. \tag{2.24}$$

To see the squeezing effect from the squeezing operator $\hat{S}$, the variances of the rotated quadrature operators of a squeezed vacuum state are calculated with $\theta = \theta_s$

$$\langle(\Delta\hat{X}_{\theta_s})^2\rangle_\zeta = \frac{1}{2}\mathrm{e}^{-2r}, \tag{2.25}$$

$$\langle(\Delta\hat{Y}_{\theta_s})^2\rangle_\zeta = \frac{1}{2}\mathrm{e}^{2r}. \tag{2.26}$$

Thus these results illustrate that the squeezing operator attenuates the quadrature variance of $\hat{X}_{\theta_s}$ and amplifies the variance of $\hat{Y}_{\theta_s}$. A more general squeezed state can be generated by first squeezing the vacuum and then displacing it, i.e.,

$$|\alpha,\zeta\rangle = \hat{D}(\alpha)\hat{S}(\zeta)\,|0\rangle\,, \tag{2.27}$$

a process shown in Fig. 2.1(d). Squeezed states have many applications in optical communication [97, 98], optical measurement [99], and quantum information processing[4]. Most importantly, the squeezed states are important resources for continuous-variable entanglement, which is discussed in Sec. 2.3.

Thermal state

The states I have discussed so far (number state, coherent state, and squeezed state) are all pure states that can be described by state vectors $|\Psi\rangle$. To describe a statistical ensemble of pure states, I introduce density operator defined as

$$\hat{\rho} = \sum_i p_i \left|\Psi_i\right\rangle \left\langle\Psi_i\right|, \tag{2.28}$$

where p_i is the probability of the system being in its ith state $|\Psi_i\rangle$ of the ensemble. For this statistical mixture, the ensemble average of an operator $\hat{O}$ can be calculated by the trace of the product of the density operator $\hat{\rho}$ and the operator $\hat{O}$

$$\langle\hat{O}\rangle = \mathrm{Tr}\{\hat{\rho}\hat{O}\}. \tag{2.29}$$

As an application of using the density operator, I consider a single-mode field in thermal equilibrium at temperature T. The density operator to describe this thermal field is

$$\hat{\rho}_{\mathrm{Th}} = \sum_n p_n \left|n\right\rangle \left\langle n\right|, \tag{2.30}$$

where p_n is the probability that the mode is thermally excited in the nth excited state. From statistical mechanics, we have

$$p_n = \frac{\mathrm{e}^{-E_n/k_{\mathrm{B}}T}}{\sum_n \mathrm{e}^{-E_n/k_{\mathrm{B}}T}} = \frac{\mathrm{e}^{-n\hbar\omega/k_{\mathrm{B}}T}}{\mathrm{e}^{\hbar\omega/k_{\mathrm{B}}T} - 1}, \tag{2.31}$$

where $E_n = \hbar\omega(n + 1/2)$ is the energy of the nth excited state.

2.1.3 Phase space representation: Wigner function

In classical physics, a state of a one-dimensional system can be represented as one point (q, p) in its phase space (the $q - p$ plane). For an ensemble of states, the statistics of the system

can be described by a phase-space probability distribution $W(q,p)$ that quantifies the probability of finding a specific state (q,p) with a simultaneous measurement of q and p. By knowing the distribution $W(q,p)$, all statistical properties can be calculated. In other words, the phase-space distribution describes the state of the ensemble in classical physics. It is more difficult to apply the same concept to quantum physics, because the Heisenberg uncertainty principle prevents us from making simultaneous measurements of q and p precisely. Consequently, a quantum phase-space distribution could become negative or ill-behaved; hence such distributions are called quasi-probability distributions. Nevertheless, the purpose of the quantum mechanical formalism is to make statistical predictions of the observations. The quantum phase-space distribution $W(q,p)$ is still useful to us for calculating observable quantities in a classical-like fashion.

Basically, there are infinite ways of defining a quantum phase-space distribution, simply because there is no method to uniquely define a proper distribution. I discuss one particular phase-space distribution—the Wigner function—because it has a direct relationship to my quadrature measurements. The Wigner function is the first quasi-probability distribution introduced into quantum mechanics by Wigner in 1932 [100]. It is a phase-space representation of a density operator $\hat{\rho}$ defined as[2]

$$W(x,y) = \frac{1}{2\pi}\int_{-\infty}^{\infty} \mathrm{e}^{iyz}\,\langle x-\frac{z}{2}|\,\hat{\rho}\,|x+\frac{z}{2}\rangle\;\mathrm{d}z. \tag{2.32}$$

An extensive literature about the Wigner function and its properties exists [101]. Here, I review only the basic properties. First, the Wigner function is real for a Hermitian density operator $\hat{\rho}$

$$W^*(x,y) = W(x,y), \tag{2.33}$$

and is normalized as

$$\int_{-\infty}^{\infty}\int_{-\infty}^{\infty} W(x,y)\,\mathrm{d}x\mathrm{d}y = 1. \tag{2.34}$$

These two features show that the Wigner function resembles a probability distribution. More importantly, the Wigner function links the density operator $\hat{\rho}$ (which represents the quantum state)

[2] For now on I will use the quadrature observables x and y to represent the dimensionless position and momentum q and p.

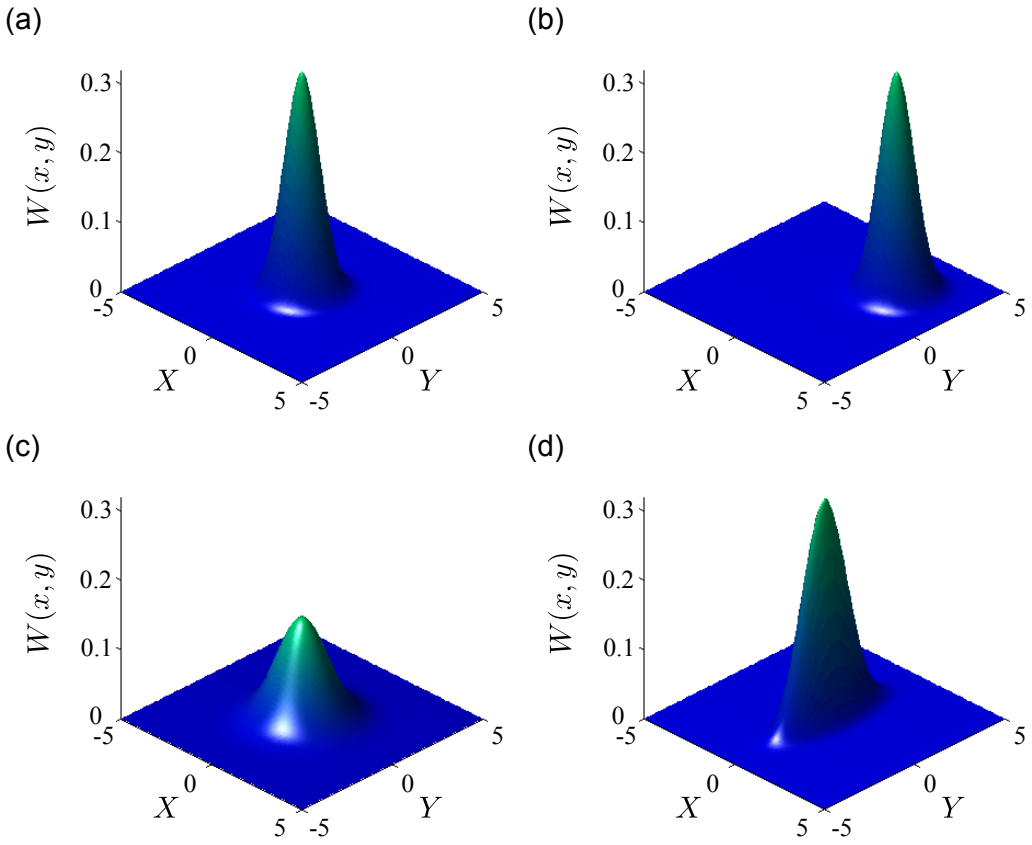

Figure 2.2: Wigner functions of various Gaussian states. Wigner functions of (a) a vacuum state, (b) a coherent state with $\alpha = \sqrt{2}(1+i)$, (c) a thermal state with $\frac{\hbar\omega}{k_{\mathrm{B}}T} = 1$, and (d) a squeezed vacuum state with $r = 0.5$.

to the observations by the marginal distribution of $W(x, y)$:

$$\int_{-\infty}^{\infty} W(x, y)\,\mathrm{d}y = \langle x|\,\hat{\rho}\,|x\rangle = \mathrm{pr}(x), \tag{2.35}$$

$$\int_{-\infty}^{\infty} W(x, y)\,\mathrm{d}x = \langle y|\,\hat{\rho}\,|y\rangle = \mathrm{pr}(y). \tag{2.36}$$

Both formulas show that the probability distribution of the x (y) quadrature $\mathrm{pr}(x)$ [$\mathrm{pr}(y)$] can be calculated by the integration of the Wigner function along the orthogonal y (x) quadrature. Generally, the probability distribution of a rotated quadrature x_θ is

$$\mathrm{pr}(x_\theta) \equiv \langle x|\,\hat{U}(\theta)\hat{\rho}\hat{U}^\dagger(\theta)\,|x\rangle = \int_{-\infty}^{\infty} W(x\cos\theta - y\sin\theta, x\sin\theta + y\cos\theta)\,\mathrm{d}y, \tag{2.37}$$

where $\hat{U}(\theta) = \mathrm{e}^{-i\theta\hat{a}^\dagger\hat{a}}$ is the phase-shifting operator that transforms the annihilation operator as $\hat{U}^\dagger(\theta)\hat{a}\hat{U}(\theta) = \hat{a}\mathrm{e}^{-i\theta}$. Note that although the marginal distributions of the Wigner function yield the correct quadrature probability distributions, the Wigner function itself is not a true probability distribution, because it can take on negative values for some quantum states.

As mentioned before, a quasi-probability distribution can be used to make quantum mechanical predictions. By using the Wigner function, the quantum expectation values of operators can be calculated by the so-called Weyl correspondence [102], i.e.,

$$\mathrm{Tr}\,\{\,\hat{\rho}\mathcal{S}(\hat{X}^m\hat{Y}^n)\,\} = \int_{-\infty}^{\infty}\int_{-\infty}^{\infty} W(x, y)x^m y^n\,\mathrm{d}x\mathrm{d}y, \tag{2.38}$$

where $\mathcal{S}(\hat{X}^m\hat{Y}^n)$ symmetrizes all possible products of the m$\hat{X}$ and n$\hat{Y}$. For example, $\mathcal{S}(\hat{x}^2\hat{y})$ becomes $1/3(\hat{x}^2\hat{y} + \hat{x}\hat{y}\hat{x} + \hat{x}\hat{y}^2)$.

Here are some examples of the single-mode Wigner functions for the quantum states that are important to my experiment. The simplest example is the Wigner function for a vacuum state:

$$W(x, y)_{\mathrm{vac}} = \frac{1}{\pi}\mathrm{e}^{-(x^2+y^2)}. \tag{2.39}$$

As expected, it is a two-dimensional Gaussian distribution centered at the origin with isotropic quadrature variances $\langle(\Delta\hat{X}_\theta)^2\rangle = 1/2$ [Fig. 2.2(a)]. By displacing the Wigner function of a vacuum state with a coherent amplitude $\sqrt{2}\,|\alpha|$, I obtain the Wigner function of a coherent state $|\alpha\rangle$

[Fig. 2.2(b)]:

$$W(x,y)_\alpha = \frac{1}{\pi}\mathrm{e}^{-[(x-x_0)^2+(p-y_0)]^2}, \tag{2.40}$$

where $x_0 = \sqrt{2}\mathrm{Re}(\alpha)$, and $y_0 = \sqrt{2}\mathrm{Im}(\alpha)$. By scaling the quadrature variances of the vacuum Wigner function, I obtain the Wigner function of an ideal squeezed vacuum state [Fig. 2.2(d)]:

$$W(x,y)_s = \frac{1}{\pi}\mathrm{e}^{-(\mathrm{e}^{2r}x^2+\mathrm{e}^{-2r}y^2)}. \tag{2.41}$$

Apparently, we have $\langle(\Delta\hat{X})^2\rangle = (1/2)\mathrm{e}^{-2r}$ and $\langle(\Delta\hat{Y})^2\rangle = (1/2)\mathrm{e}^{2r}$ indicating the effect of quadrature squeezing.

For a single-mode thermal state in equilibrium at temperature T, the state is represented by its density operator Eq. 2.30 and its Wigner function can be calculated by Eq. (2.32). I then derive

$$W(x,y)_{\mathrm{Th}} = \frac{1}{\pi\coth\frac{\hbar\omega}{2k_{\mathrm{B}}T}}\mathrm{e}^{-\frac{1}{\coth\frac{\hbar\omega}{2k_{\mathrm{B}}T}}(x^2+y^2)}, \tag{2.42}$$

where k_{B} is the Boltzmann constant. It is also a Gaussian function but with larger uniform variances $\langle(\Delta\hat{X}_\theta)^2\rangle = (1/2)\coth\frac{\hbar\omega}{2k_{\mathrm{B}}T}$ than vacuum fluctuation [Fig. 2.2(c)].

The set of states with Gaussian quasi-probability distributions, such as vacuum, coherent, squeezed, and thermal states are Gaussian states. They are of particular importance in quantum information processing with a continuous variable system, because efficient implementations for generating, manipulating, and measuring them are available. Moreover, Gaussian states with feasible operations on them are sufficient to demonstrate some basic quantum communication protocols such as quantum teleportation and quantum error correction [4]. The full power of quantum information processing, however, requires non-Gaussian states. These states can be prepared either with sufficiently nonlinear measurements (such as photon counting) or equations of motion. However, in discussing Gaussian versus non-Gaussian states one should maintain a distinction between a state that has non-Gaussian statistical properties but that is a statistical mixture of Gaussian states, and a genuine non-Gaussian state, which cannot be described as a statistical mixture of Gaussian states. By non-Gaussian state, I mean the latter; these states have Wigner functions that take on negative values in particular regions of phase-space.

A Gaussian state is completely characterized by its statistical first and second moments of the quadrature operators. Generally, for a n-mode system, I can define the quadrature mean vector $\boldsymbol{\mu}$ and the quadrature covariance matrix $\boldsymbol{\Sigma}$ as

$$\boldsymbol{\mu} \equiv (\langle \hat{X}_1 \rangle, \langle \hat{Y}_1 \rangle, \ldots, \langle \hat{X}_n \rangle, \langle \hat{Y}_n \rangle), \tag{2.43}$$

$$\Sigma_{ij} \equiv \frac{1}{2} \langle \hat{Z}_i \hat{Z}_j + \hat{Z}_j \hat{Z}_i \rangle - \langle \hat{Z}_i \rangle \langle \hat{Z}_j \rangle, \quad Z_i \in \{\hat{X}_1, \hat{Y}_1, \ldots, \hat{X}_n, \hat{Y}_n\}. \tag{2.44}$$

The mean vector $\boldsymbol{\mu}$ can be arbitrarily adjusted by phase-space displacement operations [Eq. (2.20)] in each mode of the system to re-center its phase-space distribution at the origin. Under the displacement operation, any informationally relevant property, such as entropy or entanglement, is preserved. Therefore, from now on, I will assume $\boldsymbol{\mu} = (0, \ldots, 0)$ without any loss of generality. Then the Wigner function of an n-mode Gaussian state can be written in a compact form:

$$W(\mathbf{v}) = \frac{\mathrm{e}^{-\mathbf{v}\boldsymbol{\Sigma}^{-1}\mathbf{v}^T}}{\pi^n \sqrt{\det \boldsymbol{\Sigma}}}, \tag{2.45}$$

where $\mathbf{v} = (x_1, y_1, \ldots, x_n, y_n)$.

2.2 Quantum optical tools

In experimental quantum optics, various components are available for manipulating, transforming, and measuring quantum states of light fields. These components provide us with a useful toolbox for implementing continuous-variable quantum information processing. Basically, they can be categorized into linear passive components and active devices. The passive elements, such as beam splitters and phase shifters, allow us to perform interference operations or phase-space displacements. These operations involve a linear superposition between the annihilation operators $\hat{a}_j$ of the multiple input modes. The active devices usually utilize a nonlinear effect, such as parametric amplification, to generate squeezed light, which is an important ingredient in the generation of continuous-variable entanglement. To describe this squeezing operation, a linear superposition between $\hat{a}$'s and $\hat{a}^\dagger$'s is needed. Generally, the operations of combining, displacing, and squeezing

are all described by the linear unitary Bogoliubov transformation [103]

$$\hat{b}_i = \sum_j A_{ij}\hat{a}_j + B_{ij}\hat{a}_j^\dagger + \gamma_i, \tag{2.46}$$

with the matrices A and B satisfying $AB^T = (AB^T)^T$ and $AA^\dagger = BB^\dagger + I$ to preserve the bosonic commutation relations of $\hat{b}_i$. This input-output relation describes any combination of linear optical components and nonlinear squeezing devices. Moreover, the Bogoliubov transformations map Gaussian states onto Gaussian states. Hence, they are also referred to as Gaussian operations.

In this section, I now discuss two devices that perform the necessary Gaussian operations for a two-mode entanglement experiment: a beam splitter and a single-mode squeezer.

2.2.1 Quantum mechanical beam splitters

The first device is an optical beam splitter. A lossless quantum beam splitter is modeled as a four-port device with two input modes and two output modes (Fig. 2.3). In the Heisenberg picture, a beam-splitter transforms its input annihilation operators as

$$\begin{pmatrix} \hat{b}_1 \\ \\ \hat{b}_2 \end{pmatrix} = \begin{pmatrix} t_1 & r_2 \\ \\ r_1 & t_2 \end{pmatrix} \begin{pmatrix} \hat{a}_1 \\ \\ \hat{a}_2 \end{pmatrix}, \tag{2.47}$$

where t_i and r_i are the complex amplitude transmittance and reflectance of input port i. To preserve the bosonic commutation relations for the output modes

$$[\hat{b}_i, \hat{b}_j] = [\hat{b}_i^\dagger, \hat{b}_j^\dagger] = 0, \quad [\hat{b}_i, \hat{b}_j^\dagger] = \delta_{ij} \quad (i, j = 1, 2). \tag{2.48}$$

The beam splitter transformation matrix is unitary and results in the following relations

$$|t_1| = |t_2|\,,\ |r_1| = |r_2|\,,\ |t_1|^2 + |r_1|^2 = 1,\ t_1 r_2^* + r_1 t_2^* = 0,\ \text{and}\ t_1^* r_1 + r_2^* t_2 = 0. \tag{2.49}$$

By using the definitions of quadrature operators [Eqs. (2.4)–(2.5)], the beam splitter operation can

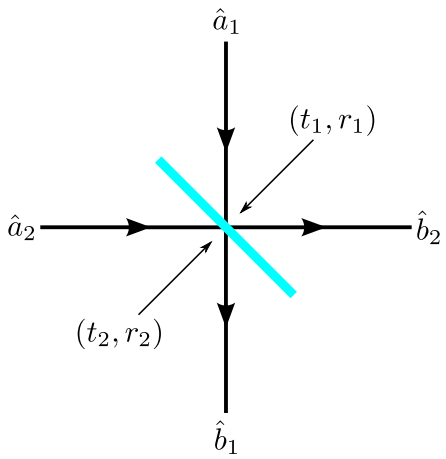

Figure 2.3: Schematic of a quantum beam splitter. The input modes $\hat{a}_1$ and $\hat{a}_2$ are scattered into output modes $\hat{b}_1$ and $\hat{b}_2$ with two sets of amplitude transmittances and reflectances (t_1, r_1) and (t_2, r_2).

be expressed as the transformation for the input to the output quadrature operators

$$\begin{pmatrix} \hat{X}_{b_1} \\ \hat{Y}_{b_1} \\ \hat{X}_{b_2} \\ \hat{Y}_{b_2} \end{pmatrix} = \begin{pmatrix} \mathrm{Re}(t_1) & -\mathrm{Im}(t_1) & \mathrm{Re}(r_2) & -\mathrm{Im}(r_2) \\ \mathrm{Im}(t_1) & \mathrm{Re}(t_1) & \mathrm{Im}(r_2) & \mathrm{Re}(r_2) \\ \mathrm{Re}(r_1) & -\mathrm{Im}(r_1) & \mathrm{Re}(t_2) & -\mathrm{Im}(t_2) \\ \mathrm{Im}(r_1) & \mathrm{Re}(r_1) & \mathrm{Im}(t_2) & \mathrm{Re}(t_2) \end{pmatrix} \begin{pmatrix} \hat{X}_{a_1} \\ \hat{Y}_{a_1} \\ \hat{X}_{a_2} \\ \hat{Y}_{a_2} \end{pmatrix}. \tag{2.50}$$

For example, a 50:50 beam splitter with $\pi/2$ phase shifts in the reflected waves has $t_1 = t_2 = 1/\sqrt{2},\ r_1 = r_2 = i/\sqrt{2}$. The input annihilation operators are transformed as

$$\hat{b}_1 = \frac{1}{\sqrt{2}}(\hat{a}_1 + i\hat{a}_2), \quad \hat{b}_2 = \frac{1}{\sqrt{2}}(i\hat{a}_1 + \hat{a}_2), \tag{2.51}$$

and the input and output quadratures are related by

$$\hat{X}_{b_1} = \frac{1}{\sqrt{2}}(\hat{X}_{a_1} - \hat{Y}_{a_2}), \tag{2.52}$$

$$\hat{Y}_{b_1} = \frac{1}{\sqrt{2}}(\hat{Y}_{a_1} + \hat{X}_{a_2}), \tag{2.53}$$

$$\hat{X}_{b_2} = \frac{1}{\sqrt{2}}(-\hat{Y}_{a_1} + \hat{X}_{a_2}), \tag{2.54}$$

$$\hat{Y}_{b_2} = \frac{1}{\sqrt{2}}(\hat{X}_{a_1} + \hat{Y}_{a_2}). \tag{2.55}$$

An important application of beam splitters is to perform balanced homodyne detection for measuring quadrature amplitudes with photon-counting devices. By directly shining a light field on a photodetector, we can only measure the intensity $I_a = c\,\langle \hat{a}_1^\dagger \hat{a}_1 \rangle$ of the field mode $\hat{a}_1$. To measure the quadrature amplitudes of mode $\hat{a}_1$, we can combine the signal field $\hat{a}_1$ with a strong coherent field $\hat{a}_2$ (local oscillator)[3] on a 50:50 beam splitter, as illustrated in Fig. 2.4. Two photodetectors are then placed at the two outputs, and the difference of the two output intensities ΔI is measured. By using Eq. (2.51), we can calculate

$$\Delta I = I_{b_1} - I_{b_2} = c\,\langle \hat{b}_1^\dagger \hat{b}_1 - \hat{b}_2^\dagger \hat{b}_2 \rangle = ci\,\langle \hat{a}_1^\dagger \hat{a}_2 - \hat{a}_1 \hat{a}_2^\dagger \rangle\,, \tag{2.56}$$

where c is a constant. Moreover, because mode $\hat{a}_2$ is in a coherent state $|\alpha_{\mathrm{LO}}\rangle$ with $\alpha_{\mathrm{LO}} = |\alpha_{\mathrm{LO}}|\,\mathrm{e}^{i\theta_{\mathrm{LO}}}$, we have

$$\Delta I = |\alpha_{\mathrm{LO}}|\,\langle \hat{a}_1 \mathrm{e}^{-i\theta} + \hat{a}_1^\dagger \mathrm{e}^{i\theta} \rangle = \sqrt{2}\,|\alpha_{\mathrm{LO}}|\,\langle \hat{X}_{a_1,\theta} \rangle\,, \tag{2.57}$$

[3] The signal and the local oscillator are assumed to have same frequencies, which makes this scheme a "homodyne" detection.

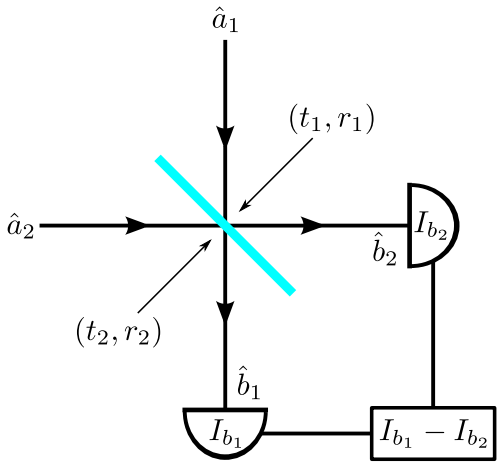

Figure 2.4: Schematic of the balanced homodyne detection. The signal mode $\hat{a}_1$ is combined with the local oscillator mode $\hat{a}_2$ on a 50:50 beam splitter. Two photodetectors measure the intensities I_{b_1} and I_{b_2} of the two output modes $\hat{b}_1$ and $\hat{b}_2$, respectively. The difference of the two intensities $I_{b_1} - I_{b_2}$ is proportional to the quadrature amplitude of the signal mode $\hat{a}_1$ with the quadrature phase θ, where θ is chosen by the phase of the local oscillator.

where $\theta = \theta_{\rm LO} + \pi/2$. Thus, by changing $\theta_{\rm LO}$, any quadrature amplitude of the signal mode $\hat{a}_1$ can be measured.

I further illustrate the usefulness of a beam splitter by discussing the output states of a beam splitter with two different types of inputs. For the first example, I consider a coherent state is incident on input port 2, while only vacuum is sent to input port 1. The initial state is $|0\rangle_{a_1}|\alpha\rangle_{a_2} = \hat{D}_{a_2}(\alpha)|0\rangle_{a_1}|0\rangle_{a_2}$. I use Eq. (2.51) to represent the displacement operator $\hat{D}_{a_2}(\alpha)$ in terms of the output mode operators and obtain the output state

$$|0\rangle_{a_1}|\alpha\rangle_{a_2} = \hat{D}_{a_2}(\alpha)|0\rangle_{a_1}|0\rangle_{a_2} \xrightarrow{\rm BS} \hat{D}_{b_1}(\frac{i\alpha}{\sqrt{2}})\hat{D}_{b_2}(\frac{\alpha}{\sqrt{2}})|0\rangle_{b_1}|0\rangle_{b_2} = |\frac{i\alpha}{\sqrt{2}}\rangle_{b_1}|\frac{\alpha}{\sqrt{2}}\rangle_{b_2}. \tag{2.58}$$

As expected, the result shows that the classical-like coherent input is evenly divided between the two outputs with a proper phase shift in the reflected wave. Moreover, the output state is simply a product state of the two output modes. This operation provides us a way to displace the input state at port 1 by sending in a coherent state at port 2. However, one disadvantage of using a balanced beam splitter is that half of the vacuum fluctuation is coupled from mode 2 to mode 1 as well. This coupled noise will degrade the information stored in the input state at port 1. To avoid having excess coupled noise, a better strategy is to use an asymmetric beam splitter with $t \gg r$ for performing the displacement operation. When using an asymmetric beam splitter, the output mode $\hat{b}_1$ can be approximated as

$$\hat{b}_1 = t_1\hat{a}_1 + r_2(\hat{a}_2 + \alpha) = t_1(\hat{a}_1 + \frac{r_2}{t_1}\alpha + \frac{r_2}{t_1}\hat{a_2}) \approx t_1(\hat{a}_1 + \frac{r_2}{t_1}\alpha), \tag{2.59}$$

where the coupled noise $\frac{r_2}{t_1}\hat{a_2}$ is neglected because of the small ratio between r_2 and t_1. As a result, by measuring only output mode 1, I obtain a nearly pure state that is the input state 1 displaced by $r_2/t_1\alpha$. I do not need to retain the output mode 2.

I consider next the example of injecting a single photon state into input port 2 and vacuum into input port 1. For this case, the initial state is $|0\rangle_{a_1}|1\rangle_{a_2} = \hat{a}_2^\dagger|0\rangle_{a_1}|0\rangle_{a_2}$, and the final state is obtained by using in $\hat{a}_2^\dagger = (i\hat{b}_1^\dagger + \hat{b}_2^\dagger)/\sqrt{2}$

$$|0\rangle_{a_1}|1\rangle_{a_2} = \hat{a}_2^\dagger|0\rangle_{a_1}|0\rangle_{a_2} \xrightarrow{\rm BS} \frac{1}{\sqrt{2}}(i\hat{b}_1^\dagger + \hat{b}_2^\dagger)|0\rangle_{b_1}|0\rangle_{b_2} = \frac{1}{\sqrt{2}}(i|1\rangle_{b_1}|0\rangle_{b_2} + |0\rangle_{b_1}|1\rangle_{b_2}). \tag{2.60}$$

Evidently, the incident photon is either transmitted or reflected. An interesting property of the output state is that it is a discrete-variable maximally entangled state. For a composite system, an entangled state is a quantum state that cannot be factored out into a product of states of the individual subsystem. As a result, the measurement on one subsystem determines the state of the others. In this example, the output state exhibits perfect correlations in the outcomes of measuring photon numbers of the two modes, i.e., given the photon number at output mode 1, the photon number at output mode 2 is certain.[4] By comparing this example to the previous one, which generates a product state with a coherent input, I illustrate the fact that it is necessary to have a nonclassical input state (more quantum than a coherent state) to generate a two-mode entangled state out of a beam splitter [104].

To fully characterize the density operator $\hat{\rho}_{12}$ of the entangled state [Eq. (2.60)], we need to measure both of the output modes. To illustrate this idea, I explicitly express the density operator $\hat{\rho}_{12}$ as

$$\hat{\rho}_{12} = \frac{1}{2}(|1\rangle_{b_1} \langle 1|_{b_1} \otimes |0\rangle_{b_2} \langle 0|_{b_2} + |0\rangle_{b_1} \langle 0|_{b_1} \otimes |1\rangle_{b_2} \langle 1|_{b_2} + i |1\rangle_{b_1} \langle 0|_{b_1} \otimes |0\rangle_{b_2} \langle 1|_{b_2} - i |0\rangle_{b_1} \langle 1|_{b_1} \otimes |1\rangle_{b_2} \langle 0|_{b_2}). \tag{2.61}$$

If I measure only output mode 1, the result is described by the reduced density operator $\hat{\rho}_1$ obtained by tracing over the unmeasured mode 2:

$$\hat{\rho}_1 = \mathrm{Tr}_2\{\hat{\rho}_{12}\} = \frac{1}{2}(|0\rangle_{b_1} \langle 0|_{b_1} + |1\rangle_{b_1} \langle 1|_{b_1}), \tag{2.62}$$

which is merely a statistical mixture, and the information of the off-diagonal coherence terms $|0\rangle_{b_1} \langle 1|_{b_1}$ and $|1\rangle_{b_1} \langle 0|_{b_1}$ is lost.

In summary, we can perform homodyne detection and phase-space displacement by using a beam splitter. Furthermore, a discrete-variable–two-mode entangled state can be generated at the outputs of a beam splitter with a single photon input. In the next section, I will explain that

[4] Obviously, product states such as $|0\rangle |1\rangle$ or $|1\rangle |0\rangle$ also exhibit correlations. However, these correlations are purely classical in the sense that the product states are only correlated with respect to the predetermined basis $\{|0\rangle,|1\rangle\}$. In contrast, an entangled state, such as $\frac{1}{\sqrt{2}}(|0\rangle |0\rangle + |1\rangle |1\rangle) = \frac{1}{\sqrt{2}}(|-\rangle |-\rangle + |+\rangle |+\rangle)$, is correlated in both bases $\{|0\rangle,|1\rangle\}$ and $\{|-\rangle,|+\rangle\}$, where $|\pm\rangle = \frac{1}{\sqrt{2}}(|0\rangle \pm |1\rangle)$ is the conjugate basis.

a continuous-variable–two-mode entangled state can also be generated by feeding squeezed states into a beam splitter.

2.2.2 Single-mode squeezers

The second device is a single-mode squeezer. It is the device that performs the squeezing operation [Eq. (2.23)] on the input mode. Specifically, the state that enters the squeezer is transformed where a specific quadrature is squeezed by some factor, and the orthogonal quadrature is amplified by the same factor. This process is a deterministic and reversible transformation; thus the total uncertainty is preserved. In optics, this transformation can be implemented via a degenerate optical parametric amplifier using a nonlinear optical $\chi^{(3)}$ process [105], or at microwave frequencies using the nonlinearity of a Josephson junction, as discussed in Ch. 3.

The generic input-output relation of an ideal single-mode squeezer is

$$\begin{pmatrix} \hat{b} \\ \hat{b}^\dagger \end{pmatrix} = \begin{pmatrix} \mathcal{G} & \mathcal{M} \\ \mathcal{M}^* & \mathcal{G}^* \end{pmatrix} \begin{pmatrix} \hat{a} \\ \hat{a}^\dagger \end{pmatrix}. \tag{2.63}$$

To maintain the bosonic commutation relations for the output mode $\hat{b}$, it is required that

$$|\mathcal{G}|^2 - |\mathcal{M}|^2 = 1. \tag{2.64}$$

Thus, we can assume $\mathcal{G} = \cosh r,\ \mathcal{M} = -\mathrm{e}^{i2\theta_s} \sinh r$ [5] By using the quadrature operators Eqs. (2.4)–(2.5), the squeezer transformation can be expressed in terms of quadrature operators as

$$\begin{pmatrix} \hat{X}_b \\ \hat{Y}_b \end{pmatrix} = \begin{pmatrix} \cosh r - \cos 2\theta_s \sinh r & -\sin 2\theta_s \sinh r \\ -\sin 2\theta_s \sinh r & \cosh r + \cos 2\theta_s \sinh r \end{pmatrix} \begin{pmatrix} \hat{X}_a \\ \hat{Y}_a \end{pmatrix}. \tag{2.65}$$

For $\theta_s = 0$, the output quadratures are

$$\hat{X}_b = \mathrm{e}^{-r} \hat{X}_a, \tag{2.66}$$

$$\hat{Y}_b = \mathrm{e}^{r} \hat{Y}_a. \tag{2.67}$$

[5] These expressions are the squeezing operations described in Eq. (2.23).

As expected, the quadrature X_b is squeezed by a factor e^r, while the orthogonal quadrature Y_b is amplified with the same factor. Generally, the squeezer transforms the rotated quadrature operators $\hat{X}_{b,\theta}$ and $\hat{Y}_{b,\theta}$ as

$$\hat{X}_{b,\theta} = \hat{X}_{a,\theta}\cosh r - \hat{X}_{a,-\theta}\cos 2\theta_s \sinh r - \hat{Y}_{a,-\theta}\sin 2\theta_s \sinh r, \tag{2.68}$$

$$\hat{Y}_{b,\theta} = \hat{Y}_{a,\theta}\cosh r + \hat{Y}_{a,-\theta}\cos 2\theta_s \sinh r - \hat{X}_{a,-\theta}\sin 2\theta_s \sinh r. \tag{2.69}$$

To summarize this section, I have discussed two important components for entanglement generation: a beam splitter and a single-mode squeezer. In next section, I will explain how I use these tools to generate a two-mode entangled state.

2.3 Continuous-variable entanglement

The concept of entanglement first appeared in literature in the famous paper by Einstein, Podolsky, and Rosen (EPR), published in 1935, which described entanglement in a continuous-variable setting [1]. The entangled state treated in the EPR paper describes a composite system having perfectly correlated positions ($q_1 - q_2 = q_0$) and perfectly anti-correlated momenta ($p_1 + p_2 = 0$) between the two subsystems. The EPR entangled state is a simultaneous eigenstate of the relative position and the total momentum of the two subsystems. As a result, the two subsystems are in a maximally entangled state.[6] However, in principle, the EPR entangled state is unnormalizable, thus unphysical.

In 1988, Reid and Drummond proposed that the EPR paradox can be demonstrated via the quadrature amplitudes of a single-mode electromagnetic field [24], because the quadrature amplitudes are mathematically equivalent to the canonically conjugate position and momentum. Essentially, the EPR entangled state is a limiting case of a two-mode squeezed vacuum with the squeezing parameter $r \to \infty$. With finite squeezing, the two-mode squeezed vacuum is a properly normalized version of the EPR state, but with some finite extent of correlation between positions

[6] Similar to the discrete-variable entangled state [Eq. (2.60)], which exhibits correlations in two mutually conjugate bases $\{|0\rangle,|1\rangle\}$ and $\{|-\rangle,|+\rangle\}$, the continuous-variable entangled states are correlated in both the positions and the conjugate momenta.

and momenta. In this section, I explain how to generate such EPR-like entangled states with the two quantum optical devices I discussed in the previous section.

2.3.1 Two-mode squeezed vacuum

A two-mode squeezed state has quantum correlations between its two modes. Mathematically, it is generated by applying a two-mode squeezed operator $\hat{S}_2(\zeta)$ on a vacuum. The two-mode operator $\hat{S}_2(\zeta)$ is defined as, in analogy with the single-mode squeezed operator Eq. (2.23),

$$\hat{S}_2(\zeta) = \mathrm{e}^{(\zeta^* \hat{a}_1 \hat{a}_2 - \zeta \hat{a}_1^\dagger \hat{a}_2^\dagger)}, \tag{2.70}$$

where $\zeta = r\mathrm{e}^{i2\theta_s}$, and $\hat{a}_1$ and $\hat{a}_2$ are the annihilation operators of the two modes. Physically, this operation can be implemented via a nondegenerate optical parametric amplifier using a nonlinear optical $\chi^{(2)}$ process [105]. Alternatively, the same type of two-mode state can be generated by combining two single-mode squeezed states on a 50:50 beam splitter. Consider that we feed a vacuum state squeezed in the y quadrature

$$\hat{X}_{a_1} = \mathrm{e}^{r} \hat{X}_{\mathrm{vac}_1}, \quad \hat{Y}_{a_1} = \mathrm{e}^{-r} \hat{Y}_{\mathrm{vac}_1}, \tag{2.71}$$

and another vacuum state squeezed in the x quadrature

$$\hat{X}_{a_2} = \mathrm{e}^{-r} \hat{X}_{\mathrm{vac}_2}, \quad \hat{Y}_{a_2} = \mathrm{e}^{r} \hat{Y}_{\mathrm{vac}_2}, \tag{2.72}$$

to the two inputs of a phase-free 50:50 beam splitter ($t_1 = t_2 = r_1 = -r_2 = 1/\sqrt{2}$), respectively. The two output modes are described by the quadrature operators of the two output modes b_1 and b_2 as

$$\hat{X}_{b_1} = \frac{1}{\sqrt{2}}(\mathrm{e}^{r} \hat{X}_{\mathrm{vac}_1} + \mathrm{e}^{-r} \hat{X}_{\mathrm{vac}_2}), \tag{2.73}$$

$$\hat{Y}_{b_1} = \frac{1}{\sqrt{2}}(\mathrm{e}^{-r} \hat{Y}_{\mathrm{vac}_1} + \mathrm{e}^{r} \hat{Y}_{\mathrm{vac}_2}), \tag{2.74}$$

$$\hat{X}_{b_2} = \frac{1}{\sqrt{2}}(\mathrm{e}^{r} \hat{X}_{\mathrm{vac}_1} - \mathrm{e}^{-r} \hat{X}_{\mathrm{vac}_2}), \tag{2.75}$$

$$\hat{Y}_{b_2} = \frac{1}{\sqrt{2}}(\mathrm{e}^{-r} \hat{Y}_{\mathrm{vac}_1} - \mathrm{e}^{r} \hat{Y}_{\mathrm{vac}_2}), \tag{2.76}$$

obtained by using the beam splitter transformation [Eq. (2.50)]. The output quadrature operators show that although the individual quadrature of each output mode becomes noisy because of the e^r term, $\hat{X}_{b_1} - \hat{X}_{b_2}$ and $\hat{Y}_{b_1} + \hat{Y}_{b_2}$ become quieter than a vacuum state:

$$\hat{X}_{b_1} - \hat{X}_{b_2} = \sqrt{2}e^{-r}\hat{X}_{\mathrm{vac}_2}, \tag{2.77}$$

$$\hat{Y}_{b_1} + \hat{Y}_{b_2} = \sqrt{2}e^{-r}\hat{Y}_{\mathrm{vac}_1}. \tag{2.78}$$

Furthermore, as $r \to \infty$, the quadrature variances of $\hat{X}_{b_1} - \hat{X}_{b_2}$ and $\hat{Y}_{b_1} + \hat{Y}_{b_2}$ vanish, and the two-mode state becomes the maximally entangled EPR state.

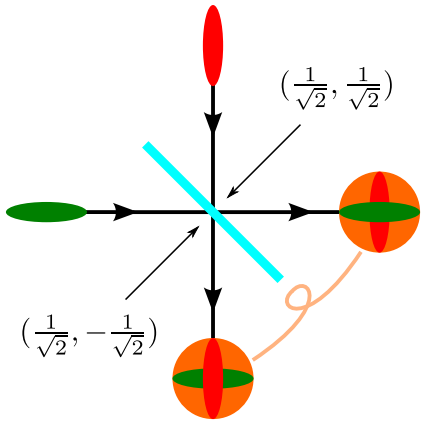

Figure 2.5: Schematic of two-mode entanglement from a 50:50 beam splitter. A two-mode entangled state emerges at the outputs of a 50:50 beam splitter with two quadrature squeezed states as inputs.

The statistical properties of the two-mode squeezed vacuum can be described by its Wigner function

$$W(x_1, y_1, x_2, y_2) = \frac{1}{\pi^2} e^{-\frac{1}{2}e^{-2r}[(x_1+x_2)^2+(y_1-y_2)^2]-\frac{1}{2}e^{2r}[(x_1-x_2)^2+(y_1+y_2)^2]}, \tag{2.79}$$

where r is the squeezing parameter, and (x_1, y_1) and (x_2, y_2) are the quadrature variables of mode 1 and mode 2, respectively. For example, we can calculate the marginal distributions for the two x quadratures and the two y quadratures by integrating over the two orthogonal quadratures

$$\int\int W(x_1, y_1, x_2, y_2)\, dy_1 dy_2 = \frac{1}{\pi} e^{-\frac{1}{2}e^{-2r}(x_1+x_2)^2-\frac{1}{2}e^{2r}(x_1-x_2)^2}, \tag{2.80}$$

$$\int\int W(x_1, y_1, x_2, y_2)\, dx_1 dx_2 = \frac{1}{\pi} e^{-\frac{1}{2}e^{-2r}(y_1-y_2)^2-\frac{1}{2}e^{2r}(y_1+y_2)^2}. \tag{2.81}$$

Again, these results show that, although the width of the distribution for each mode of its individual x and y quadratures increases as the squeezing grows, the $x_1 - x_2$ and $y_1 + y_2$ are well defined with large squeezing ($r \to \infty$). Furthermore, it also illustrates the fact that, similar to the discrete-variable entanglement, to fully characterize the two-mode state, we need to measure both modes in a joint measurement. Specifically, if I measure only mode 2, the associated two-dimensional Wigner function would be found by integrating the four-dimensional Wigner function over the two quadratures of mode 1. The result is a mixed state with a thermal distribution

$$\int\int W(x_1, y_1, x_2, y_2)\,\mathrm{d}x_1\mathrm{d}y_1 = \frac{1}{\pi(1+2\bar{n})}\mathrm{e}^{-\frac{x_2^2+y_2^2}{1+2\bar{n}}}, \tag{2.82}$$

with mean photon number $\bar{n} = \sinh r^2$.

2.3.2 Entanglement witness and measure

In previous discussions, I have shown a continuous-variable–two-mode entangled state can be generated from a 50:50 beam splitter with squeezed states as inputs. To rigorously demonstrate this EPR-type entanglement, a definition of entanglement feasible for continuous-variable systems is needed. Here, I present the criteria for bipartite entanglement, which is entanglement shared by only two parties.

For any pure two-party state, entanglement is defined by the nonfactorizability of the total state vector, as shown in the example of Eq. 2.60. For mixed states, which are states usually generated from practical experiments, the nonfactorizable concept is generalized to the inseparability of the total density operator. A general quantum state of a two-party system is separable if, and only if, its density operator can be expressed in the following form [106]:

$$\hat{\rho}_{12} = \sum_i p_i \hat{\rho}_{i,1} \otimes \hat{\rho}_{i,2}, \tag{2.83}$$

where $\hat{\rho}_{i,1}$ and $\hat{\rho}_{i,2}$ are density operators of mode 1 and mode 2, respectively, and the weights satisfy $p_i \geq 0$, $\sum_i p_i = 1$. Thus, entanglement can be verified by testing the separability of a state.

A separability criterion for two-party continuous-variable states has been derived by Duan

[86]. In this criterion, a pair of EPR-like operators are defined as

$$\hat{\mu} = |a|\,\hat{X}_1 - \frac{1}{a}\hat{X}_2, \tag{2.84}$$

$$\hat{\nu} = |a|\,\hat{Y}_1 + \frac{1}{a}\hat{Y}_2, \tag{2.85}$$

where a is an arbitrary nonzero real number. Based on the Heisenberg uncertainty principle, Duan derived that, for any separable state $\hat{\rho}$, the sum of the variances of the two EPR-like operators, which is called the total variance, has a lower bound

$$\langle(\Delta\hat{\mu})^2\rangle_\rho + \langle(\Delta\hat{\nu})^2\rangle_\rho \geq a^2 + \frac{1}{a^2}. \tag{2.86}$$

In other words, the violation of the inequality is a sufficient condition for a state to be inseparable. Furthermore, for all Gaussian states, it provides a necessary and sufficient condition for inseparability. Therefore, an entanglement witness can be defined as

$$E_{\rm w} = \langle(\Delta\hat{\mu})^2\rangle_\rho + \langle(\Delta\hat{\nu})^2\rangle_\rho - (a^2 + \frac{1}{a^2}) < 0. \tag{2.87}$$

This entanglement witness links the definition of entanglement to measurable quadrature variances of continuous two-mode states. Intuitively, we can understand the entanglement witness $E_{\rm w}$ by noticing that, when $a = 1$, the $\hat{\mu}$ and $\hat{\nu}$ operators are the correlated pair of two-mode squeezed states [Eq. (2.77 and 2.78)], and the quantity on the right hand side of the inequality corresponds to the total variance for the two modes in vacuum states. Essentially, the entanglement witness states that the total variance of an entangled state is smaller than that of a vacuum state. In other words, when given the outcomes of measuring the quadratures (X_1, Y_1) in mode 1, we can predict the outcomes of measuring the quadrature s(X_2, Y_2) in mode 2, with uncertainties below vacuum fluctuations.

The entanglement witness $E_{\rm w}$ is a useful criterion for us to verify the existence of entanglement. To further quantify the bipartite mixed states entanglement, I use a quantity named negativity $\mathcal{N}$ [107]. The concept of this measure of entanglement originates from Peres' partial transpose criterion for the separability of a density operator [108, 87]. This criterion said that a

legitimate density operator should have non-negative eigenvalues because of its hermiticity. For a separable state represented by a density operator as in Eq. (2.83), the transposition of the density operator in either mode yields another legitimate non-negative density operator. Specifically, if $\hat{\rho}_{i,1}$ is transposed in Eq. (2.83), it yields

$$\hat{\rho}'_{12} = \sum_i p_i \hat{\rho}_{i,1}^T \otimes \hat{\rho}_{i,2}. \tag{2.88}$$

The condition that $\hat{\rho}'_{12}$ has non-negative eigenvalues is a necessary condition that $\hat{\rho}_{12}$ is separable. Therefore, the existence of a negative eigenvalue for $\hat{\rho}'_{12}$ is a sufficient condition for the inseparability of $\hat{\rho}_{12}$. The negativity $\mathcal{N}$ measures the degree to which $\hat{\rho}'_{12}$ fails to be positive and is defined as

$$\mathcal{N} = \left| \sum \text{negative eigenvalues of } \hat{\rho}^{T_1} \right| = \frac{\left|\left|\hat{\rho}^{T_1}\right|\right|_1 - 1}{2}, \tag{2.89}$$

where $\left|\left|\hat{\rho}^{T_1}\right|\right|_1$ is the trace norm of the partial transpose of $\hat{\rho}$ with respect to mode 1. If $\mathcal{N} > 0$, the state $\hat{\rho}$ is entangled, and $\mathcal{N} \to \infty$ for a maximally entangled state. The negativity $\mathcal{N}$ has the advantage that it can be evaluated completely straightforwardly using standard linear algebra packages. Furthermore, the negativity provides a bound on the capacity of a quantum communication protocol called quantum teleportation that exploits entanglement [107]. Both of the criteria, E_{w} and $\mathcal{N}$, can be evaluated from the covariance matrix, which can be calculated from simultaneous quadrature measurements.

Chapter 3

Theory of Josephson parametric amplifiers

A Josephson parametric amplifier (JPA) is capable of performing a squeezing operation on its input states. Experimentally, a JPA serves us two purposes. It not only creates the required squeezed states for entanglement generation, but also enables us to perform efficient quadrature measurements on the amplified quadratures of its output states. Because quantum mechanics places no lower bound on the added noise of a phase-sensitive amplifier, a single-quadrature measurement with detection efficiency better than 50% is possible by using a JPA as the first amplifier in an amplifier chain.

In this chapter, I present the theory of JPAs. I start with reviewing the basic theory of Josephson junctions that provide the necessary nonlinearity for the parametric process in electrical circuits. Following that I present the quantum models of the electrical oscillation circuits. Then, by using the input-output formalism, I derive the expressions for the field within the nonlinear resonator of the JPA, the reflected coefficient of the nonlinear resonator, the parametric gains, and the noise squeezing.

3.1 Basic Josephson junctions theory

Josephson junctions are the critical elements for microwave superconducting circuits. In our experiments, we embed our Josephson junctions within LC circuits to make nonlinear resonant circuits. Josephson junctions are used as dissipationless nonlinear inductors that provide the necessary nonlinearity for the parametric amplification process. Here, I review the basic theory of the

Josephson junctions that are relevant for designing a JPA.

3.1.1 Simple junction theory

A Josephson junction consists of two superconducting electrodes separated by a thin insulating layer [Fig. 3.1(a)]. Below the critical temperature, electrons in each superconductor can bind together forming a bosonic condensate of Cooper pairs that can be described by a macroscopic wave function $\Psi(r) = \sqrt{n}e^{i\theta}$, where n is the density of the Cooper pairs. In 1962, Brian Josephson predicted that this macroscopic wave function could tunnel through the insulating barrier from one superconductor to the other in this junction structure [109]. In other words, a tunneling current of Cooper pairs can flow through the junction. The tunneling Cooper pairs require no voltage to flow and are driven by the phase difference $\theta_1 - \theta_2$ of the two macroscopic wave functions in each electrode.

We operate our JPAs in the regime where the current flowing through the junctions is smaller than the maximum current that the junction can support in its superconducting state. This maximum current is called the critical current I_c. In this regime, the tunneling current I that flows through the junction is governed by the Josephson current-phase relation

$$I = I_c \sin \delta, \tag{3.1}$$

where the phase δ is the gauge-invariant phase difference given by

$$\delta = \theta_1 - \theta_2 - \frac{2\pi}{\Phi_0} \int_1^2 \mathbf{A} \cdot \mathrm{d}\mathbf{l}, \tag{3.2}$$

where $\Phi_0 = h/2e$ is the flux quantum, and $\mathbf{A}$ is the vector potential of the magnetic field that the junction is subject to. The line integral path is taken from one superconducting electrode to the other [Fig. 3.1(a)]. At zero magnetic field, the critical current I_c of a single junction is given by the Ambegaokar-Baratoff formula [110]

$$I_c = \frac{\pi \Delta(T)}{2eR_n} \tanh\left(\frac{\Delta(T)}{2k_\mathrm{B}T}\right), \tag{3.3}$$

where R_n is the normal state resistance of the junction, and $\Delta(T)$ is the superconducting gap of the material at temperature T.

The dynamics of the Josephson junction are governed by the Josephson voltage-phase relation

$$\frac{\mathrm{d}\delta}{\mathrm{d}t} = \frac{2\pi}{\Phi_0} V, \tag{3.4}$$

where V is the voltage across the junction. The effective inductance of the Josephson junction can then be calculated by taking the time derivative of Eq. (3.1). Relating the voltage and the current with Eq. (3.4), we obtain

$$V = \frac{L_{J0}}{\cos\delta} \frac{\mathrm{d}I}{\mathrm{d}t}, \tag{3.5}$$

where $L_{J0} = \Phi_0/(2\pi I_c)$. Thus, a Josephson junction can be viewed as a lumped inductor with a Josephson small signal inductance L_J, where

$$L_J = \frac{L_{J0}}{\cos\delta}. \tag{3.6}$$

We can also calculate the energy associated with a Josephson junction. Consider that the junction is driven by a current source increasing from zero to some value. During the time that the current is changing, a voltage is generated across the junction according to Eq. (3.4). Therefore, the energy expended by the current source during this process is

$$E_J = \int_0^t I(\tau)V(\tau)\,\mathrm{d}\tau = \int_0^t (I_c \sin\delta)(\frac{\Phi_0}{2\pi}\frac{\mathrm{d}\delta}{\mathrm{d}\tau})\,\mathrm{d}\tau = -E_{J0}\cos\delta + \text{constant}, \tag{3.7}$$

where $E_{J0} = \Phi_0 I_c/(2\pi)$.

3.1.2 DC SQUID

By combining two Josephson junctions in parallel, we form a superconducting quantum interference device (SQUID) [Fig. 3.2(a)]. In superconducting circuits, a SQUID behaves as a dissipationless nonlinear inductor, which provides the required nonlinearity in our parametric amplification circuits.

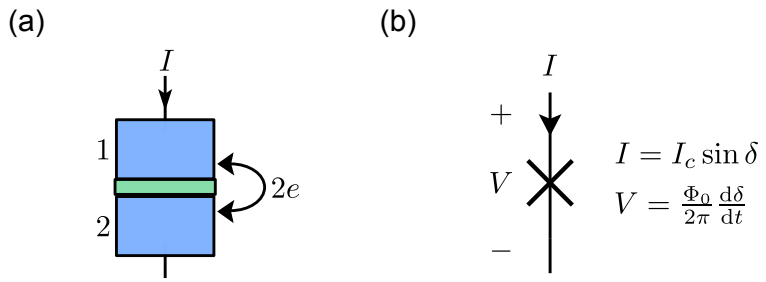

Figure 3.1: Josephson Junction. (a) A Josephson junction consists of two superconductors separated by a thin layer of insulator through which Cooper pairs can tunnel. (b) The Josephson junction is treated as a lumped circuit element and represented by a cross symbol. Its behavior is governed by the two Josephson equations shown here.

We can analyze the properties of a SQUID with the Josephson relations discussed above. The total current that flows through the SQUID is the sum of the current flowing through each junction, as described by Eq. (3.1):

$$I = I_1 + I_2 = I_{c1}\sin\delta_1 + I_{c2}\sin\delta_2. \tag{3.8}$$

Because the phase θ of the macroscopic wave function is allowed to change by $2\pi n$ when integrated in the SQUID loop, the difference in the gauge invariant phases is related to the total flux Φ threading the SQUID loop by

$$\delta_2 - \delta_1 = 2\pi n + \frac{2\pi\Phi}{\Phi_0}. \tag{3.9}$$

We assume the two junctions are identical ($I_{c1} = I_{c2} = I_c$). By using Eq. (3.9), the total current I becomes

$$I = 2I_c\cos\left(\frac{\pi\Phi}{\Phi_0}\right)\sin\left(\delta_1 + \frac{\pi\Phi}{\Phi_0}\right) = I_s\sin\delta_s. \tag{3.10}$$

We first consider the case where the inductance of the SQUID loop is negligible, $\Phi \approx \Phi_{\mathrm{ext}}$. Then the SQUID can be viewed as a device having the critical current I_s, where

$$I_s = 2I_c\left|\cos\left(\frac{\pi\Phi_{\mathrm{ext}}}{\Phi_0}\right)\right|. \tag{3.11}$$

Similar to a single junction, the effective inductance of the SQUID can be calculated by taking the

time derivative of the current I and using Eq. (3.4). The current-voltage relation of the SQUID is

$$V = \frac{L_{S0}}{\cos\delta_s}\frac{\mathrm{d}I}{\mathrm{d}t}, \tag{3.12}$$

where $L_{S0} = \Phi_0/(2\pi I_s)$. Therefore, the SQUID inductance is given by

$$L_S = \frac{\Phi_0}{4\pi I_c \left|\cos\left(\frac{\pi\Phi_{\mathrm{ext}}}{\Phi_0}\right)\right| \cos\delta_s}. \tag{3.13}$$

Apparently, the SQUID inductance depends on the external magnetic flux applied to the SQUID loop. We will use this property of the SQUID to build tunable nonlinear resonant circuits by embedding SQUIDs in electrical oscillation circuits.

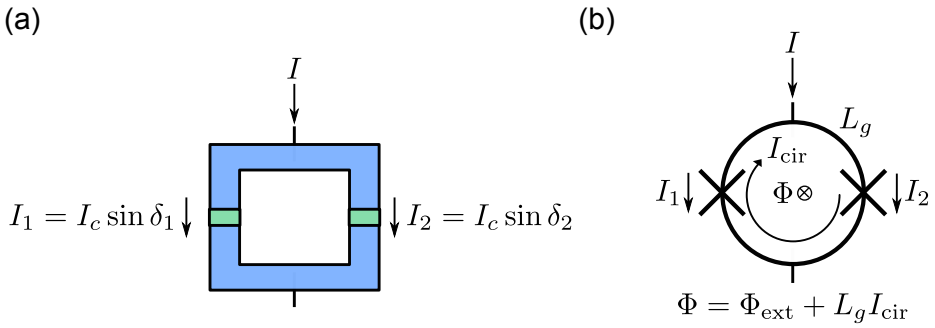

Figure 3.2: DC SQUID. (a) Two Josephson junctions connected in parallel by superconducting wires forms a DC SQUID. The current flowing through each junction is characterized by its gauge-invariant phase difference. (b) The DC SQUID is represented by a circular loop interrupted with two crosses. The loop area is A, and the geometrical inductance of the loop is L_g. With an externally applied magnetic field B perpendicular to the SQUID loop, the total flux threading the SQUID loop is the sum of the external flux $\Phi_{\mathrm{ext}} = BA$ and the self-induced flux $L_g I_{\mathrm{cir}}$.

Generally, when taking into account the loop inductance L_g of the SQUID, the total flux Φ that threads the SQUID loop is the sum of the externally applied flux and the self-induced flux [Fig. 3.2(b)], i.e.,

$$\Phi = \Phi_{\mathrm{ext}} + L_g I_{\mathrm{cir}}, \tag{3.14}$$

where $I_{\mathrm{cir}} = (I_2 - I_1)/2$ is the current circulating through the SQUID loop. By using Eq. (3.9), the total flux can be written as

$$\Phi = \Phi_{\mathrm{ext}} - L_g I_c \sin\left(\frac{\pi\Phi}{\Phi_0}\right)\cos\left(\delta_1 + \frac{\pi\Phi}{\Phi_0}\right). \tag{3.15}$$

The critical current of the SQUID with a given Φ_{ext} is obtained by maximizing Eq. (3.10) with respect to δ_1, subject to the constraint of Eq. (3.15). The flux dependence of the critical current I_s is solved numerically and shown in Fig. 3.3. As a consequence of the finite loop inductance, the modulation depth of the critical current is reduced [Fig. 3.3(a)]. Moreover, for a small loop inductance, the minimum value of the critical current can be approximated by $I_s^{\min}/I_c \approx \pi L_g I_c/\Phi_0$, as shown in Fig. 3.3(b).

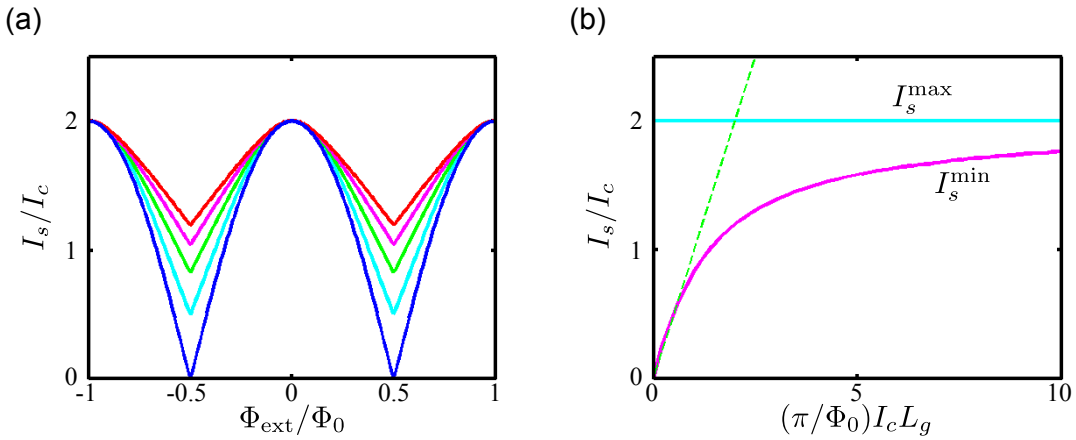

Figure 3.3: DC SQUID critical current. (a) Flux dependence of the critical currents of DC SQUIDs for $(\pi/\Phi_0)I_cL_g = 0$ (blue), 0.5 (cyan), 1 (green), 1.5 (magenta), and 2 (red). The modulation depth is reduced as the loop inductance is increased. (b) The minimum (magenta) and the maximum (cyan) of the flux-modulated critical current versus the loop inductance. For small loop inductance, the critical current is approximated by a linear function $I_s^{\min}/I_c = (\pi/\Phi_0)I_cL_g$ (dashed green).

Finite loop inductance also results in the possibility of flux trapping in the SQUID loop. By using Eq. (3.15), we can examine the total flux threading a SQUID loop for a given external flux when no current flows through it ($\cos(\delta_1 + \frac{\pi\Phi}{\Phi_0}) = 1$). As the loop inductance increases, the total flux becomes a multivalued function of the external flux. In other words, for a specific external flux, the SQUID can be in various states having extra trapped flux quanta in the SQUID loop (Fig. 3.4). Such trapped flux is extremely undesirable for building an amplifier that is tuned with flux. Thus, while fabricating SQUIDs with higher critical currents, we also need to minimize the loop inductance to avoid trapped flux.

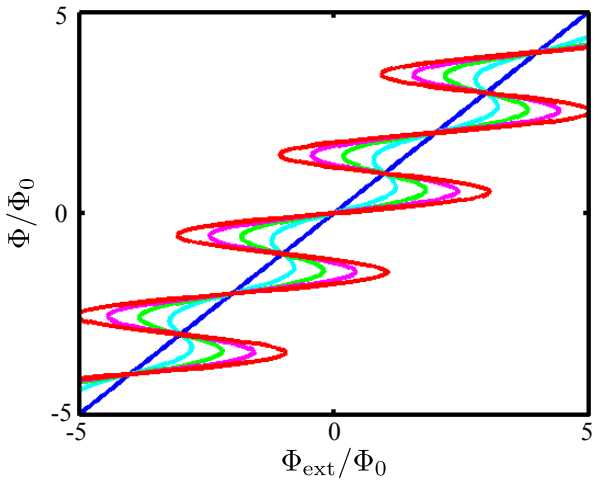

Figure 3.4: DC SQUID flux trapping. Total flux Φ of the DC SQUID is plotted against the externally applied flux $\Phi_{\rm ext}$ for $(\pi/\Phi_0)I_cL_g = 0$ (blue), 2 (cyan), 4 (green), 6 (magenta), and 8 (red). The total flux becomes a multivalued function of the external flux, and thus allows flux-trapping states.

3.2 Quantization of electrical harmonic oscillators

The theory of parametric amplifiers involves the analysis of coupled oscillation electrical circuits. Normally, electrical circuits can be analyzed with classical circuit theory such as Kirchhoff's voltage and current laws. However, when the circuits are at low temperatures and have low dissipations, the quantum mechanical behaviors of the electrical circuits start to play important roles. Specifically, to be able to observe the quantum properties of electrical circuits, the circuits need to be cooled down to temperatures such that $k_{\mathrm{B}}T \ll \hbar\omega_0$, where ω_0 is the resonance frequency of the circuits. Additionally, the separation of energy levels must be larger than their linewidth γ, which leads to the condition that $\mathcal{Q} = \omega_0/\gamma \gg 1$. When analyzing the electrical circuits in this regime, the quantum properties of the circuits are important to the dynamics of the systems.

In this section, I describe the procedures to quantize the electrical circuits. First, I quantize a linear LC oscillation circuit. Then, I discuss a nonlinear Josephson oscillator, which is formed by embedding a Josephson junction in the LC circuit. This nonlinear oscillator is quantized with the same procedure. Finally, I obtain an effective Hamiltonian of the nonlinear oscillation circuits.

3.2.1 LC circuit

The LC circuit shown in Fig. 3.5(a) can be quantized by the usual canonical quantization procedure [111, 112, 113]. The circuit consists of one inductor L and one capacitor C connected together. The energy stored in the capacitor and the inductor are

$$E_C = \frac{1}{2}CV^2, \tag{3.16}$$

$$E_L = \frac{1}{2}LI^2, \tag{3.17}$$

where I is the current flowing through the inductor, and V is the voltage across the capacitor. In analogy to a mechanical harmonic oscillator, the inductive energy plays the role of the potential energy, while the capacitive energy plays the role of the kinetic energy. I introduce a variable Φ_n

called the branch flux as a generalized coordinate of the circuit system:

$$\Phi_n = \int_{-\infty}^{t} V_n(\tau)\,\mathrm{d}\tau, \tag{3.18}$$

where n is the branch index that indicates the path through a specific element between two nodes in the circuits. Because the capacitor and the inductor are in parallel, their branch fluxes are the same ($\Phi_C = \Phi_L = \Phi$). Thus, the Lagrangian of the LC circuit can be written as

$$\mathcal{L} = \frac{1}{2}C\dot{\Phi}^2 - \frac{1}{2}\frac{\Phi^2}{L}. \tag{3.19}$$

The conjugate momentum of Φ can then be derived

$$\frac{\partial \mathcal{L}}{\partial \dot{\Phi}} = CV_C = Q. \tag{3.20}$$

To obtain the classical Hamiltonian $\mathcal{H}$ of the LC circuit, I perform the Legendre transformation $\mathcal{H} = \dot{\Phi}Q - \mathcal{L}$ and obtain

$$\mathcal{H} = \frac{1}{2}\frac{\Phi^2}{L} + \frac{1}{2}\frac{Q^2}{C}. \tag{3.21}$$

Finally, I can quantize the LC circuit by promoting the conjugate variables Φ and Q to be Hermitian operators $\hat{\Phi}$ and $\hat{Q}$, which satisfy the canonical commutation relation

$$[\hat{\Phi}, \hat{Q}] = i\hbar. \tag{3.22}$$

Then we obtain the quantum Hamiltonian of the LC circuit

$$\hat{H} = \frac{1}{2}\frac{\hat{\Phi}^2}{L} + \frac{1}{2}\frac{\hat{Q}^2}{C}, \tag{3.23}$$

which has the same form as for a quantum harmonic oscillator. In analogy to the mechanical oscillator, we can define the annihilation and the creation operators $\hat{A}$ and $\hat{A}^\dagger$ as

$$\hat{A} = \sqrt{\frac{1}{2\hbar Z}}(\hat{\Phi} + iZ\hat{Q}), \tag{3.24}$$

$$\hat{A}^\dagger = \sqrt{\frac{1}{2\hbar Z}}(\hat{\Phi} - iZ\hat{Q}), \tag{3.25}$$

where $Z = \sqrt{L/C}$. By using Eq. (3.22), $\hat{A}$ and $\hat{A}^\dagger$ satisfy the bosonic commutation relation

$$[\hat{A}, \hat{A}^\dagger] = 1. \tag{3.26}$$

Reversing Eq. (3.24), we can express $\hat{\Phi}$ and $\hat{Q}$ in terms of $\hat{A}$ and $\hat{A}^\dagger$

$$\hat{\Phi} = \sqrt{\frac{\hbar Z}{2}}(\hat{A} + \hat{A}^\dagger), \tag{3.27}$$

$$\hat{Q} = i\sqrt{\frac{\hbar}{2Z}}(\hat{A}^\dagger - \hat{A}), \tag{3.28}$$

By replacing $\hat{\Phi}$ and $\hat{Q}$ with $\hat{A}$ and $\hat{A}^\dagger$, the standard form of Hamiltonian for a quantum harmonic oscillator is derived

$$\hat{H} = \hbar\omega(\hat{A}^\dagger\hat{A} + \frac{1}{2}), \tag{3.29}$$

where $\omega = 1/\sqrt{LC}$.

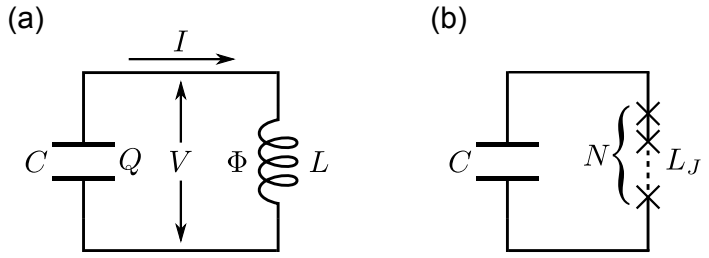

Figure 3.5: LC oscillation circuit. (a) A linear electrical oscillator consists of a capacitor and a inductor. The system coordinates are $\Phi = LI$ and $Q = CV$. (b) A nonlinear electrical oscillator is formed by replacing the linear inductor with an array of N SQUIDs.

3.2.2 Josephson junction oscillator

After quantizing the linear LC circuit, I present the quantization of a nonlinear oscillation circuit. The nonlinear microwave circuit is formed by replacing the linear inductor in the LC circuit with a serial array of N SQUIDs, as illustrated in Fig. 3.5(b). Each SQUID in the array can be described as a single Josephson junction with a tunable effective Josephson energy of E_{J0}. The SQUIDs are assumed to be identical. Thus the branch flux through each SQUID is Φ/N, where Φ is the total branch flux across the SQUID array. By using Eq. (3.7), the Lagrangian of the nonlinear circuit is

$$\mathcal{L} = \frac{1}{2}C\dot{\Phi}^2 + NE_{J0}\cos(\frac{2\pi\Phi}{\Phi_0 N}). \tag{3.30}$$

Again, by performing the Legendre transformation $\mathcal{H} = \dot{\Phi}Q - \mathcal{L}$, I obtain the classical Hamiltonian of the nonlinear Josephson oscillator

$$\mathcal{H} = \frac{1}{2}\frac{Q^2}{C} - NE_{J0}\cos\left(\frac{2\pi\Phi}{\Phi_0 N}\right). \tag{3.31}$$

By assuming that the current flowing through the SQUID array is small compared to the critical current of each SQUID, I then expand the cosine potential and keep up to the first nonquadratic term

$$\mathcal{H} \approx \frac{1}{2}\frac{Q^2}{C} + \frac{1}{2}\frac{\Phi^2}{NL_{J0}} - \frac{1}{24}\frac{1}{N^3 L_{J0}}\left(\frac{2\pi}{\Phi_0}\right)^2\Phi^4, \tag{3.32}$$

where I have used $E_{J0} = (\frac{\Phi_0}{2\pi})^2/L_{J0}$ and dropped the zero-point energy that does not affect the dynamics of the system. This Hamiltonian shows that the circuit has a linear part consisting of a capacitance C and an inductance $L_J = NL_{J0}$ as well as a nonlinear part arising from the quartic potential of Φ. To quantize the nonlinear circuit, the classical variables Φ and Q are again replaced with their corespondent operators $\hat{\Phi}$ and $\hat{Q}$. By using Eq. 3.27, we obtain the Hamiltonian describing the nonlinear Josephson junction oscillator

$$\hat{H} = \hbar\omega\hat{A}^\dagger\hat{A} + \frac{\hbar}{2}K\hat{A}^\dagger\hat{A}^\dagger\hat{A}\hat{A}, \tag{3.33}$$

where

$$\omega = \frac{1}{\sqrt{NL_{J0}C}} + K, \quad K = -\frac{\pi^2\hbar}{2\Phi_0^2}\frac{Z^2}{N^3 L_{J0}}. \tag{3.34}$$

In the above expression, I drop the zero-point energy and make the rotating wave approximation that corresponds to neglecting all terms with an unequal number of $\hat{A}$ and $\hat{A}^\dagger$ operators. The quantity K is referred to as the Kerr constant. This constant quantifies the degree of nonlinearity in the circuit as the change in the resonance frequency per photon. We can analyze the parametric amplification characterized by the nonlinear Hamiltonian Eq. 3.33, where the constants ω and K can be related to the circuit parameters via Eq. 3.34.

3.3 Parametric amplifier theory

After obtaining the quantum Hamiltonian of a nonlinear oscillation circuit, I introduce a generic model of a parametric amplifier. In this section, I derive the expressions that allow us

to understand and design JPAs. The derivation is based on the input-output theory, and the procedures are mainly from references [114].

As shown in Fig. 3.6, a parametric amplifier can be modeled by a nonlinear resonator coupled to two bath modes through its two open ports, where port 1 is the input-output port of the resonator, and port 2 is the additional port to model the loss of itself. Therefore, the total Hamiltonian of this system is a sum of three terms

$$\hat{H} = \hat{H}_{\text{res}} + \hat{H}_{\text{bath}} + \hat{H}_{\text{coup}}, \tag{3.35}$$

where each term represents the Hamiltonian for each component of the system. The resonator Hamiltonian $\hat{H}_{\text{res}}$ is the nonlinear oscillator Hamiltonian Eq. (3.33) and is restated here

$$\hat{H}_{\text{res}} = \hbar\omega_0 \hat{A}^\dagger \hat{A} + \frac{\hbar}{2} K \hat{A}^\dagger \hat{A}^\dagger \hat{A} \hat{A}, \tag{3.36}$$

where $\omega_0/(2\pi)$ is the undriven resonance frequency. Both of the two baths have continuous spectra with Hamiltonian

$$\hat{H}_{\text{bath}} = \sum_{n=1,2} \int \frac{\mathrm{d}\omega}{2\pi} \hbar\omega \hat{a}_n^\dagger(\omega) \hat{a}_n(\omega), \tag{3.37}$$

where $\hat{a}_1(\omega)$ models the modes that couple to the resonator through its input-output port, and $\hat{a}_2(\omega)$ represents the modes that absorb energy from the resonator. These bath-mode operators obey the bosonic commutation relations

$$[\hat{a}_i(\omega), \hat{a}_j^\dagger(\omega')] = 2\pi\delta_{i,j}\delta(\omega - \omega'), \quad [\hat{a}_i(\omega), \hat{a}_j(\omega')] = [\hat{a}_i^\dagger(\omega), \hat{a}_j^\dagger(\omega')] = 0. \tag{3.38}$$

The resonator is assumed to be coupled to the bath modes by the linear coupling relation and the coupling Hamiltonian, $\hat{H}_{\text{coup}}$, is

$$\hat{H}_{\text{int}} = \hbar \sum_{n=1,2} \int \frac{\mathrm{d}\omega}{2\pi} [\kappa_n \hat{A}^\dagger \hat{a}_n(\omega) + \kappa_n^* \hat{a}_n^\dagger(\omega) \hat{A}], \tag{3.39}$$

where the coupling coefficient κ_n quantifies the degree of coupling between the resonator mode $\hat{A}$ and the bath modes $\hat{a}_n$. The coefficient κ_n is assumed to be constant over the frequency range relevant to the system by the Markov approximation.

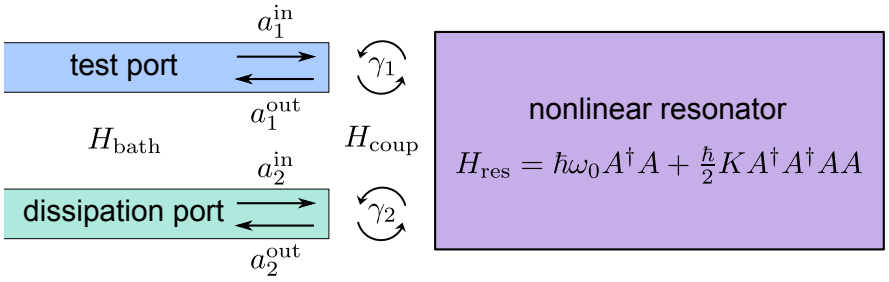

Figure 3.6: Input-Output theory model of a parametric amplifier. (a) A parametric amplifier is modeled by a nonlinear resonator coupled to a test port with coupling rate γ_1. The loss of the resonator is modeled by the coupling to another open port with coupling rate γ_2.

Using the standard input-output formalism [115], we derive the equation of motion for the resonator mode $\hat{A}$ of the system

$$\frac{\mathrm{d}\hat{A}}{\mathrm{d}t} = -i\omega_0\hat{A} - i(\gamma_1+\gamma_2)\hat{A} - iK\hat{A}^\dagger\hat{A}\hat{A} + \sqrt{2\gamma_1}\hat{a}_1^{\text{in}} + \sqrt{2\gamma_2}\hat{a}_2^{\text{in}}, \tag{3.40}$$

where the coupling constant κ_n is expressed in terms of the real constant γ_n with $\kappa_n = i\sqrt{\gamma_n/\pi}$. To obtain this equation, the bath mode $\hat{a}_n$ is separated into the incoming mode $\hat{a}_n^{\text{in}}$ and the outgoing mode $\hat{a}_n^{\text{out}}$. Because of the Markov approximation, the incoming and outgoing mode operators obey the commutation relations

$$[\hat{a}_i^\alpha(t), \hat{a}_j^{\alpha\dagger}(t')] = \delta_{i,j}\delta(t-t'), \quad [\hat{a}_i^\alpha(t), \hat{a}_j^\alpha(t')] = [\hat{a}_i^{\alpha\dagger}(t), \hat{a}_j^{\alpha\dagger}(t')] = 0, \tag{3.41}$$

for $\alpha \to \text{in}, \text{out}$. Additionally, the boundary conditions that relate the incoming, outgoing, and resonator modes are obtained as well from the input-output theory, i.e.,

$$\hat{a}_1^{\text{out}} = \hat{a}_1^{\text{in}} - \sqrt{2\gamma_1}\hat{A}(t), \tag{3.42}$$

$$\hat{a}_2^{\text{out}} = \hat{a}_2^{\text{in}} - \sqrt{2\gamma_2}\hat{A}(t). \tag{3.43}$$

When operating the system as an amplifier, an intense sinusoidal field called the pump is delivered to the resonator, and the signals detuned from the pump within the bandwidth of the resonator will be amplified. Thus the strategy to deal with this nonlinear problem is first solving the response of the resonator to the classical pump field in the absence of signals and then linearizing

about the classical steady-state response to find the equation of motion for the small quantum signal fields. In the following discussion, I describe the classical response of the parametric amplifier to a strong sinusoidal pump with a qualitative description of the saturation power of the amplifier. Then I perform the linearization procedure that leads to a scattering relation between the input and output signal fields. Finally, I discuss the performance of the parametric amplifier, including parametric gain, amplifier bandwidth, and noise squeezing.

3.3.1 Classical response

When operating a parametric amplifier, a strong coherent field is used to pump the amplifier. To obtain the classical response of the parametric amplifier to the intense pump field in the absence of any signal and noise, the inputs are set to be

$$a_1^{\text{in}} = b_1^{\text{in}} \mathrm{e}^{-i(\omega_p t+\phi_p)}, \tag{3.44}$$

$$a_2^{\text{in}} = 0. \tag{3.45}$$

where b_1^{in} is a real constant that quantifies the strength of the pump, ω_p is the pump frequency, and ϕ_p is the pump phase. The field within the resonator is assumed to have the same frequency ω_p,

$$A = B\mathrm{e}^{-i(\omega_p t+\phi_B)}, \tag{3.46}$$

where B is a real constant, and ϕ_B is the phase of the resonator field. Substituting Eqs. (3.44)–(3.46) into the equation of motion Eq. (3.40) yields

$$[i\Delta\omega+\gamma]B + iKB^3 = \sqrt{2\gamma_1} b_1^{\text{in}} \mathrm{e}^{i(\phi_B-\phi_p)}, \tag{3.47}$$

where $\Delta\omega = \omega_p - \omega_0$ is the pump detuning frequency, and $\gamma = \gamma_1 + \gamma_2$ is the total coupling rate. Multiplying Eq. (3.47) by its complex conjugate yields the following equation

$$N^3 - \frac{2\Delta\omega}{K}N^2 + \frac{\Delta\omega^2+\gamma^2}{K^2}N - \frac{2\gamma_1}{K^2}(b_1^{\text{in}})^2 = 0, \tag{3.48}$$

where $N = A^*A = B^2$ represents the energy of the field within the resonator in unit of quanta. The cavity photon number N versus the pump detuning frequency $\Delta\omega_p$ is plotted in Fig. 3.7 for

various pump amplitudes. For a small pump drive, Eq. 3.48 has only one real solution that results in the usual Lorentzian resonance curve of a linear harmonic oscillator. As the pump amplitude increases, the response of the resonator starts to depend on the amplitude of the internal field. As a result, the resonance curves bend to the lower frequency. At points where the slopes are steep, the system is sensitive to small changes in the pump. Consequently, high parametric gains are achieved at these operation points. I will illustrate this idea more in a later discussion of the reflected pump field.

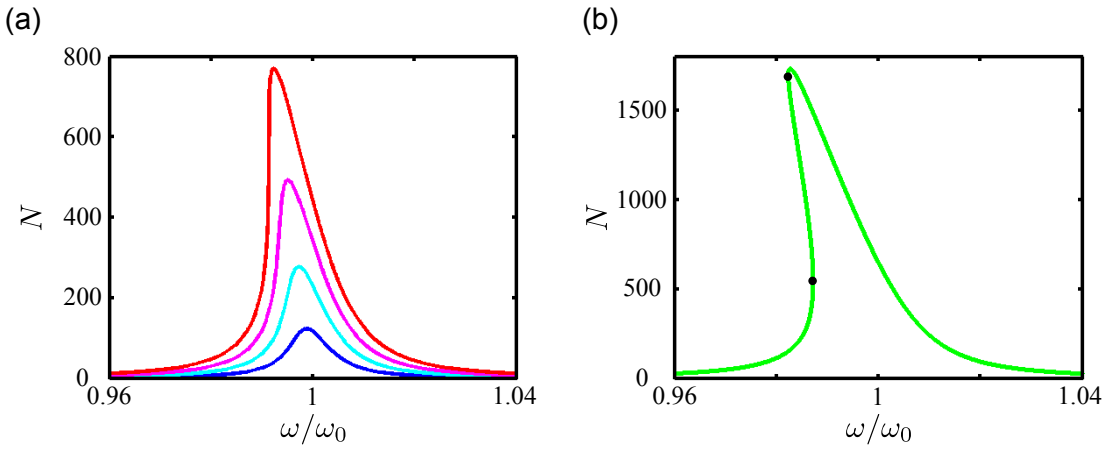

Figure 3.7: Internal field of the driven nonlinear resonator. (a) The number of photons within the driven Josephson nonlinear resonator versus the pump frequency for $b_1^{\text{in}} = 0.4b_{1c}^{\text{in}}$ (blue), $0.6b_{1c}^{\text{in}}$ (cyan), $0.8b_{1c}^{\text{in}}$ (magenta), and b_{1c}^{in} (red). (b) For $b_1^{\text{in}} = 1.5b_{1c}^{\text{in}}$ (green), the resonance curve is multi-valued at certain pump frequencies. The two black dots indicate points with infinite slopes. The solutions between them are unstable. For all cases, $\gamma_1 = 0.005\omega_0$, $\gamma_2 = 0$, $K = -10^{-5}\omega_0$, and the same parameters will be used for all following figures.

When the pump amplitude is larger than the critical pump amplitude b_{1c}^{in}, Eq. 3.48 will have three solutions. In this situation, the resonator is driven to a bistable region where two stable states exist [Fig. 3.7(b)]. To keep the amplifier in a stable configuration, we operate the parametric amplifier below the critical point to avoid any bifurcation. The critical parameters can be found by applying the condition $\frac{\partial \omega_p}{\partial N} = 0$, which yields the two points with infinite slopes shown in Fig. 3.7(b). In addition, the two points merge into one when $\frac{\partial^2 \omega_p}{\partial N^2} = 0$. By satisfying the two conditions ($\frac{\partial \omega_p}{\partial N} = 0$, $\frac{\partial^2 \omega_p}{\partial N^2} = 0$), I derive the critical pump amplitude b_{1c}^{in}, the critical pump

frequency ω_{pc}, and the critical resonator field N_c:

$$(b_{1c}^{\text{in}})^2 = \frac{4}{3\sqrt{3}} \frac{\gamma^3}{\gamma_1 |K|}, \tag{3.49}$$

$$\omega_{pc} = \omega_0 + \sqrt{3}\gamma \frac{K}{|K|}, \tag{3.50}$$

$$N_c = \frac{2\sqrt{3}\gamma}{3|K|}. \tag{3.51}$$

To derive the reflected pump field, I assume that it has the same frequency ω_p and is written in the form

$$a_1^{\text{out}} = b_1^{\text{out}} \mathrm{e}^{-i(\omega_p t + \phi_p)}, \tag{3.52}$$

where b_1^{out} may be a complex number. By using Eq. (3.47) and the boundary condition Eq. (3.42), the reflected coefficient $\Gamma \equiv b_1^{\text{out}}/b_1^{\text{in}}$ is derived

$$\Gamma = 1 + \frac{2\gamma_1}{i(\Delta\omega - KN) - \gamma}. \tag{3.53}$$

If the resonator is lossless, $|\Gamma| = 1$, and all the information is encoded in the reflected phase. The reflected phase versus pump detuning for various pump strengths is plotted in Fig. 3.8, demonstrating similar resonance pulling effect. The resonance curve becomes sharper as the pump approaches its critical value.

The mechanism leading to the phase-dependent amplification of the parametric amplifier can be intuitively understood from its classical response to a coherent input field. The input field can be decomposed into the vector sum of a large pump and a small signal. The output signal field can then be calculated as the difference between the reflection of the input field and that of the pump field only. Because the nonlinear resonator is driven to a state such that the phase of the reflected field is sensitive to a small change in the input field, the output signal depends on the phase of the input signal, as illustrated in Fig. 3.9.

In addition, I have a qualitative analysis of the saturation power for signals having frequencies near the pump frequency. To illustrate the analysis, a series of inputs are plotted as circles around the pump field in Fig. 3.10. The corresponding outputs are also plotted around the reflected pump. For a signal having a small amplitude relative to the pump, the output traces out an

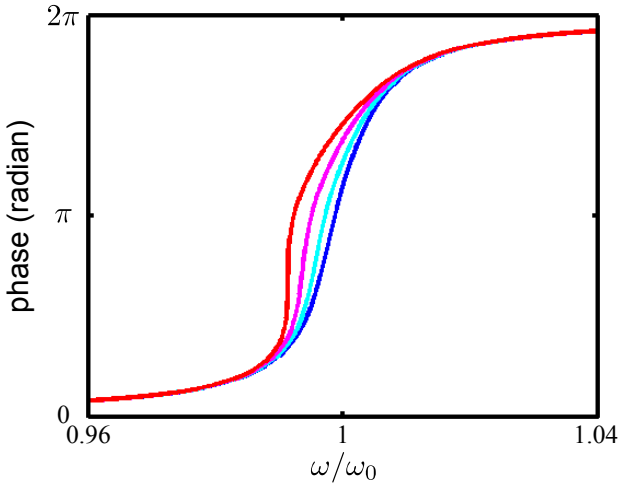

Figure 3.8: Phase of the reflection coefficient for the nonlinear resonator. The reflected phases are plotted versus the normalized pump frequency for $b_1^{\rm in} = 0.4b_{1c}^{\rm in}$ (blue), $0.6b_{1c}^{\rm in}$ (cyan), $0.8b_{1c}^{\rm in}$ (magenta), and $b_{1c}^{\rm in}$ (red). The resonance frequency shifts towards lower frequencies, and the phase response becomes sharper as the pump amplitude approaches its critical value.

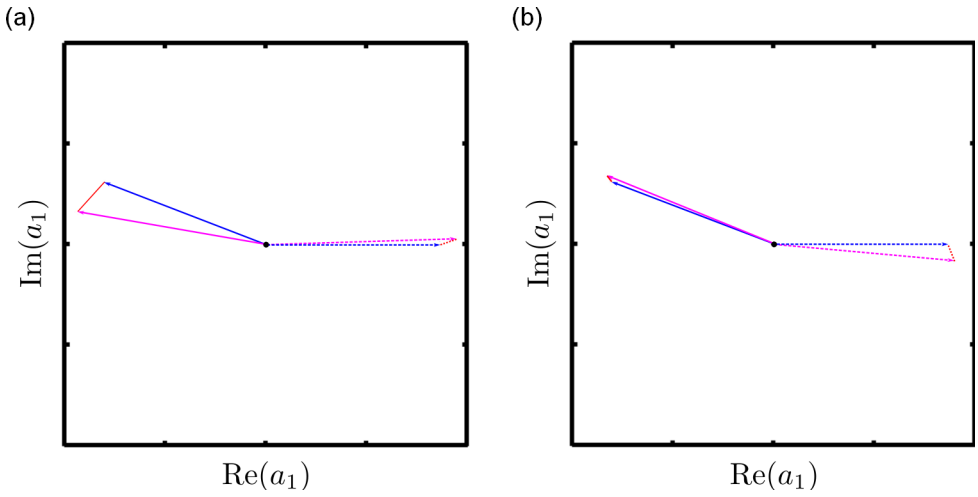

Figure 3.9: Illustration of the phase-sensitive parametric gain. (a) Amplification. The input (dashed magenta) consisting of a strong pump (dashed blue) and a weak signal (dashed red) is plotted in the quadrature plane of the input. The amplified output signal (solid red) is the difference between the reflected input (solid magenta) and the reflected pump (solid blue). (b) Deamplification. The input field has the same pump field and signal amplitude as in (a), but the phase of the input signal is chosen such that the output signal is deamplified.

ellipse, demonstrating that the signal is either amplified or squeezed depending on the signal phase. When operating in the linear regime, the size of the output ellipse increases proportionally to the input signal amplitude. For a large signal amplitude, the output ellipse becomes a banana shape, indicating that the degree of both amplification and squeezing is decreasing.

To quantify this saturation effect, I first find the projections of the output contours onto an axis, where the angle of the axis relative to the $\mathrm{Re}(b_1^{\mathrm{in}})$ axis is varied from 0 to π, as illustrated in Fig. 3.11. Then the degree of amplification and squeezing is defined as the largest-and-smallest projection lengths divided by the diameter of the input circle, respectively. Finally, I plot the amplification and squeezing versus the output signal power with various pump strengths (Fig. 3.12). From these figures, I conclude that, as a rule of thumb, the output signal power should be about 20 dB lower than the pump power to operate the parametric amplifier in its linear regime.

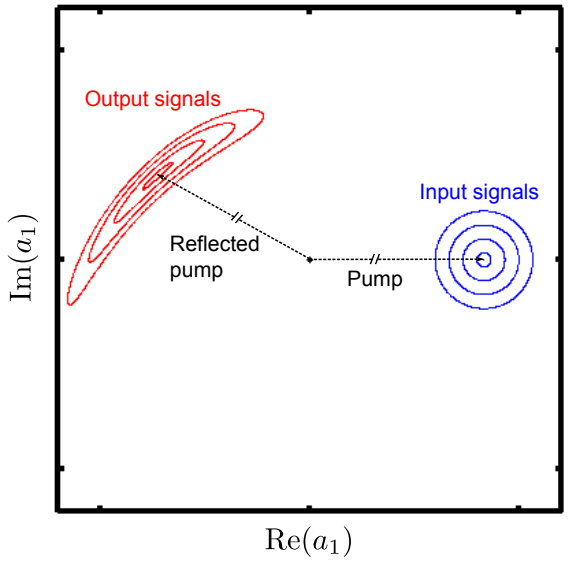

Figure 3.10: Classical responses of the parametric amplifiers. A series of input signals represented by the blue circles around the pump tone (black dashed line) with increasing radius. The corresponding outputs are represented with red contours around the reflected pump.

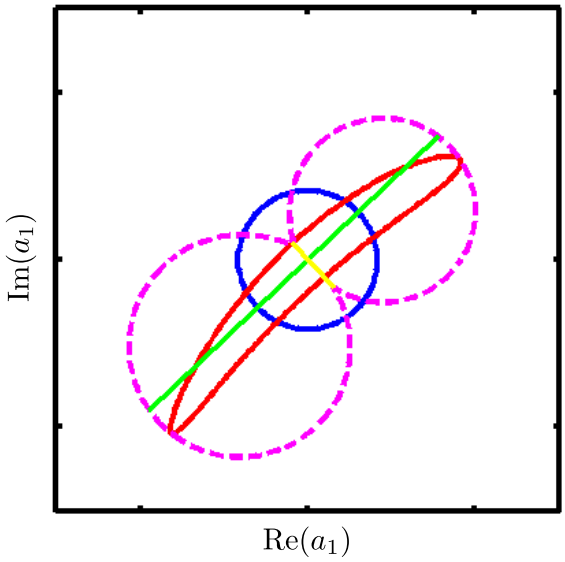

Figure 3.11: Qualitative definitions of amplification and squeezing. The input signals are represented by the blue circle with radius $b_{1,s}^{\text{in}}$. The corresponding output is the red contour. The dashed-magenta contour is the projection of the output onto the axis that has angles relative to the Re(a_1) axis varying from 0 to π. The amplification and the squeezing are then defined as $20\log(\text{maxPL}/2b_{1,s}^{\text{in}})$ and $-20\log(\text{minPL}/2b_{1,s}^{\text{in}})$, respectively, where maxPL and maxPL are the lengths of the longest (green) and the shortest (yellow) axes of the projection contour, respectively. In this figure, the input and output contours are displaced back to origin for comparison.

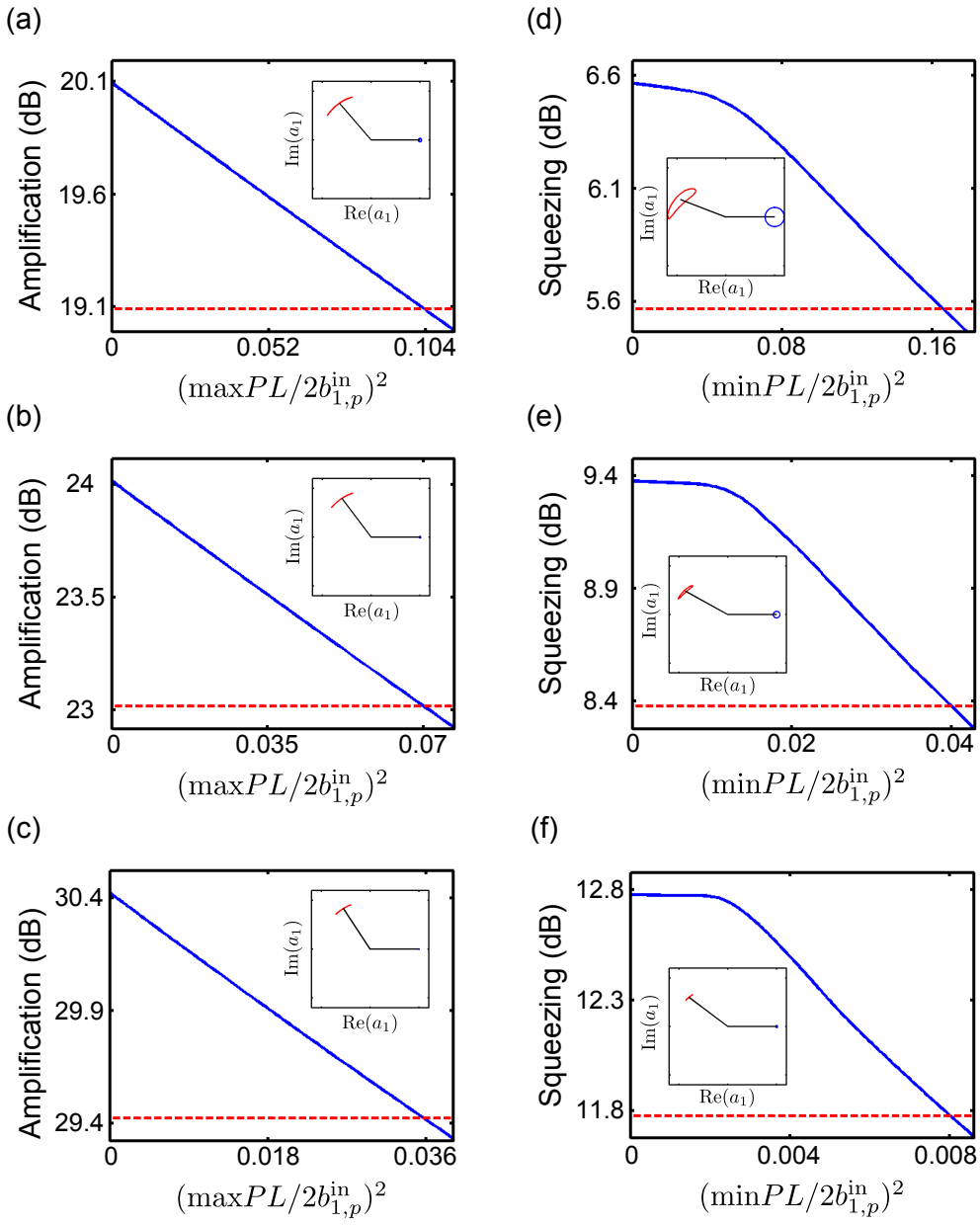

Figure 3.12: JPA saturation analysis. (a) (b) (c) Amplification versus the output signal power represented with $(\max PL/2)^2$ normalized by the pump power $(b_{1,p}^{\text{in}})^2$ for $b_{1,p}^{\text{in}} = 0.85b_{1c}^{\text{in}}$, $0.9b_{1c}^{\text{in}}$, $0.95b_{1c}^{\text{in}}$, respectively. (d) (e) (f) Squeezing versus the output signal power normalized by the pump power for $b_{1,p}^{\text{in}} = 0.5b_{1c}^{\text{in}}$, $0.6b_{1c}^{\text{in}}$, $0.7b_{1c}^{\text{in}}$, respectively. The 1 dB compression levels are indicated by the red-dashed lines. These figures are qualitative analyses of the saturation points that assume no depletion of the pump power. Insets: The input and output signal contours at the 1 dB compression points.

3.3.2 Linearized response

I have solved the nonlinear equation of motion with a classical input field. To obtain the dynamics of the parametric amplifier to small signals, I linearize the system around the classical response point. The linearization procedure is performed by assuming the input signals and noises are small compared to the pump field. The inputs are set to be

$$a_1^{\rm in} = b_1^{\rm in} {\rm e}^{-i(\omega_p t+\phi_p)} + c_1^{\rm in}(t){\rm e}^{-i\omega_p t}, \tag{3.54}$$

$$a_2^{\rm in} = c_2^{\rm in}(t){\rm e}^{-i\omega_p t}. \tag{3.55}$$

The internal field and the output fields are

$$A = B{\rm e}^{-i(\omega_p t+\phi_B)} + a(t){\rm e}^{-i\omega_p t}, \tag{3.56}$$

$$a_1^{\rm out} = b_1^{\rm out}{\rm e}^{-i(\omega_p t+\phi_p)} + c_1^{\rm out}(t){\rm e}^{-i\omega_p t}, \tag{3.57}$$

$$a_2^{\rm out} = b_2^{\rm out}{\rm e}^{-i\omega_p t} + c_2^{\rm out}(t){\rm e}^{-i\omega_p t}. \tag{3.58}$$

In the above expressions, B, $b_1^{\rm out}$, and $b_2^{\rm out}$ are the solutions for the response to the pump $b_1^{\rm in}$ and have been exactly solved. The quantities $c_1^{\rm in}(t)$, $c_2^{\rm in}(t)$, $a(t)$, $c_1^{\rm out}(t)$, and $c_2^{\rm out}(t)$ represent the small input modes in the pump-rotating frame and generally are not constant. Substituting these expressions into the equation of motion Eq. (3.40) and the boundary conditions Eq. (3.42) and keeping only the linear terms in c's and a, we obtain the linearized equations of the parametric amplifier. I express these linear equations in a compact form by creating a state space model

$$\frac{{\rm d}x}{{\rm d}t} = Ax + Bu, \tag{3.59}$$

$$y = Cx + Du, \tag{3.60}$$

where the state vector x, the control vector u, and the measurement vector y are defined as

$$x = \begin{pmatrix} a \\ a^\dagger \end{pmatrix}, \quad u = \begin{pmatrix} c_1^{\rm in} \\ c_1^{\rm in\dagger} \\ c_2^{\rm in} \\ c_2^{\rm in\dagger} \end{pmatrix}, \quad y = \begin{pmatrix} c_1^{\rm out} \\ c_1^{\rm out\dagger} \\ c_2^{\rm out} \\ c_2^{\rm out\dagger} \end{pmatrix}. \tag{3.61}$$

This linear system of the parametric amplifier can be expressed in terms of the dynamic matrix A,

$$A = \begin{pmatrix} W & V \\ V^* & W^* \end{pmatrix} = \begin{pmatrix} i(\Delta\omega - 2KN) - \gamma & -iKN\mathrm{e}^{-2i\phi_B} \\ iKN\mathrm{e}^{2i\phi_B} & -i(\Delta\omega - 2KN) - \gamma \end{pmatrix}, \tag{3.62}$$

the control matrix B,

$$B = \begin{pmatrix} \sqrt{2\gamma_1} & 0 & \sqrt{2\gamma_2} & 0 \\ 0 & \sqrt{2\gamma_1} & 0 & \sqrt{2\gamma_2} \end{pmatrix}, \tag{3.63}$$

the sensor matrix C,

$$C = \begin{pmatrix} -\sqrt{2\gamma_1} & 0 \\ 0 & -\sqrt{2\gamma_1} \\ -\sqrt{2\gamma_2} & 0 \\ 0 & -\sqrt{2\gamma_2} \end{pmatrix}, \tag{3.64}$$

and the direct term D,

$$D = \begin{pmatrix} 1 & 0 & 0 & 0 \\ 0 & 1 & 0 & 0 \\ 0 & 0 & 1 & 0 \\ 0 & 0 & 0 & 1 \end{pmatrix}. \tag{3.65}$$

The response of the linear system can be solved by finding the transfer function of the state space model. For a later discussion of an ideal parametric amplifier, I present the solutions for a lossless resonator. In this case, the transfer function is a 2×2 matrix which relates the inputs and outputs as

$$\begin{pmatrix} c_1^{\mathrm{out}}(\omega) \\ c_1^{\mathrm{out}\dagger}(-\omega) \end{pmatrix} = \begin{pmatrix} g_s(\omega) & g_i(\omega) \\ g_i^*(-\omega) & g_s^*(-\omega) \end{pmatrix} \begin{pmatrix} c_1^{\mathrm{in}}(\omega) \\ c_1^{\mathrm{in}\dagger}(-\omega) \end{pmatrix}, \tag{3.66}$$

where

$$g_s(\omega) = 1 - \frac{2\gamma_1(-i\omega - W^*)}{(-i\omega - \lambda_+)(-i\omega - \lambda_-)}, \tag{3.67}$$

$$g_i(\omega) = \frac{-2\gamma_1 V}{(-i\omega - \lambda_+)(-i\omega - \lambda_-)}, \tag{3.68}$$

with

$$\lambda_\pm = \mathrm{Re}(W) \pm \sqrt{\mathrm{Re}(W)^2 - |W|^2 + |V|^2}, \tag{3.69}$$

or

$$\lambda_{\pm} = -\gamma \pm \sqrt{K^2N^2 - (\Delta\omega - 2KN)^2}. \tag{3.70}$$

The transfer function Eq. (3.66) relates the inputs and outputs in the frequency domain, where $c_1^{\alpha}(\omega)$ is the fourier component of $c_1^{\alpha}(t)$ defined by

$$c_1^{\alpha}(t) = \int_{-\infty}^{\infty} \frac{\mathrm{d}\omega}{2\pi} c_1^{\alpha}(\omega) \mathrm{e}^{-i\omega t}, \tag{3.71}$$

for $\alpha \to \mathrm{in}, \mathrm{out}$. With the input-output relation Eq. (3.66), we are able to discuss the performance of the parametric amplifier, which includes its parametric gain, bandwidth and the noise squeezing.

3.3.3 Performance of a parametric amplifier

Parametric gain

The input-output relation Eq. (3.66) states that both inputs $c_1^{\mathrm{in}}(\omega)$ and $c_1^{\mathrm{in}\dagger}(-\omega)$, which represent signals with frequencies ω and $-\omega$ detuned from the pump frequency ω_p, respectively, contribute to the output signal at frequency ω detuned from ω_p. In other words, a signal at frequency $\omega_p + \omega$ sent to the parametric amplifier results in not only a direct output signal at frequency $\omega_p + \omega$, but also an image output at frequency $\omega_p - \omega$. Now I define the direct power gain of the amplifier as

$$G_{\mathrm{D}}(\omega) = \left|g_s(\omega)\right|^2, \tag{3.72}$$

and the intermodulation gain as

$$G_{\mathrm{I}}(\omega) = \left|g_i(\omega)\right|^2. \tag{3.73}$$

The parametric gains depend on both the pump power and the pump detuning, as illustrated in Fig. 3.13, with a signal frequency $\omega = 0$. The pump detuning for maximum gains with a specific pump power shifts approximately linearly with increasing pump power.

Because of the intermodulation gain, the parametric amplifier is noiseless for a signal that is a linear combination of Fourier frequencies symmetric around the pump. In other words, to be amplified noiselessly, a signal needs to be all contained in a single quadrature. On the other hand,

if an input signal is a single frequency tone at frequency ω, the amplifier has to add noise, where the added noise originates from the input noise at frequency $-\omega$.

Bandwidth

To discuss the bandwidth of the parametric amplifier, we first note that the direct gain and the intermodulation gain are symmetric around the pump frequency. Thus,

$$G_{\mathrm{D}}(\omega) = G_{\mathrm{D}}(-\omega), \tag{3.74}$$

$$G_{\mathrm{I}}(\omega) = G_{\mathrm{I}}(-\omega), \tag{3.75}$$

which is illustrated in Fig. 3.14. Furthermore, from the expressions Eqs. (3.67)–(3.68), we see the bandwidth of the parametric gains is set by λ_+. Quantitatively, for the high-gain limit

$$G_{\mathrm{D}}(\omega) \approx G_{\mathrm{I}}(\omega) = G(\omega) = \frac{4\gamma_1^2 |V|^2}{(\omega^2+\lambda_+^2)(\omega^2+\lambda_-^2)} \approx \frac{G(0)}{1+(\frac{\omega}{B_\omega/2})^2}, \tag{3.76}$$

where $B_\omega = 2\lambda_+$ is the full width at half maximum (FWHM) of the amplification frequency response. Furthermore, by using the critical parameters in Eq. (3.49), we show that the gain-bandwidth product is constant:

$$\sqrt{G(0)}B_\omega = \frac{4}{\sqrt{3}}\gamma, \tag{3.77}$$

which is a common property of many amplifiers.

Noise squeezing

Because of the creation of an image output, the parametric amplifier establishes correlations between the $\omega_p + \omega$ and $\omega_p - \omega$ components of the output field. These correlations in the outputs lead to the reduction of the input quadrature fluctuations with properly chosen quadrature phases. This noise squeezing effect can be proved by the fact that the input-output relation Eq. (3.66) satisfies the single-mode squeezing transformation Eq. (2.64):

$$|g_s(\omega)|^2 - |g_i(\omega)|^2 = 1, \tag{3.78}$$

$$g_s(\omega)g_i(-\omega) = g_s(-\omega)g_i(\omega). \tag{3.79}$$

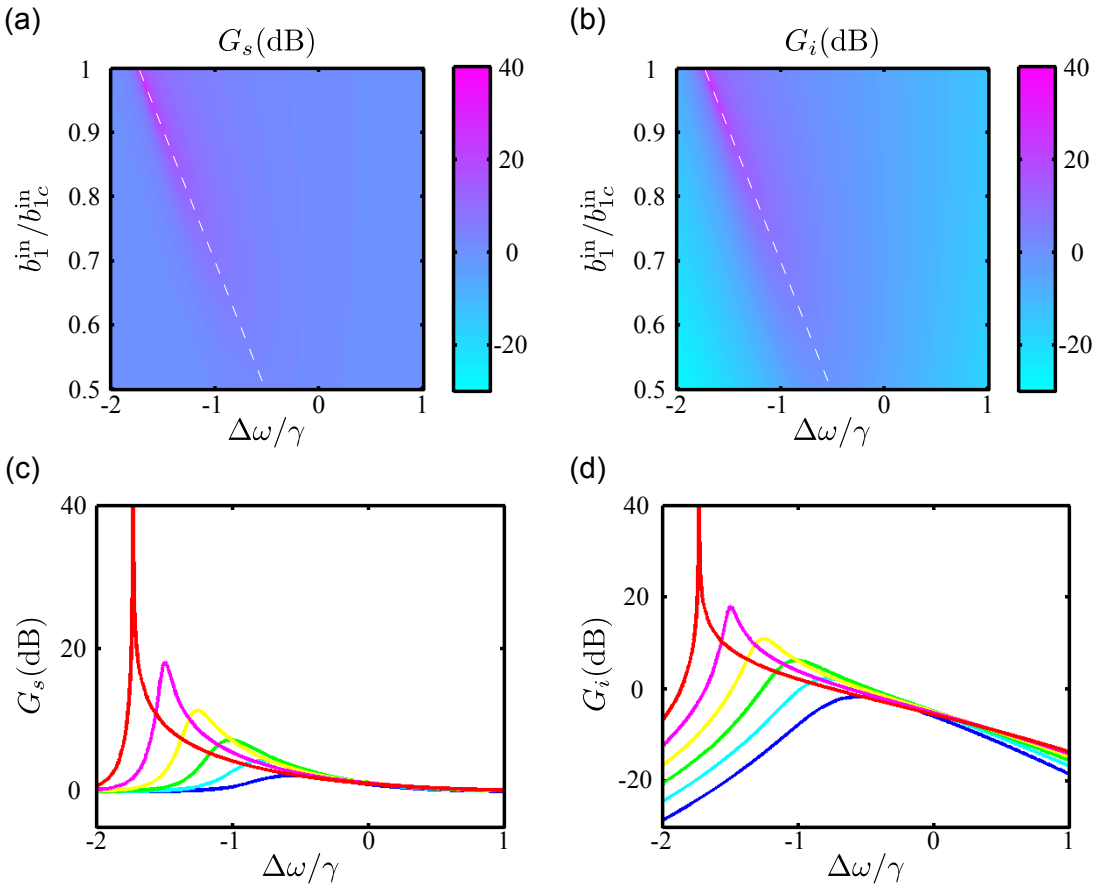

Figure 3.13: Direct gain and intermodulation gain. (a) The direct gain G_s and (b) the intermodulation gain G_i versus the pump detuning frequency $\Delta\omega$ and the normalized pump amplitude $b_1^{\rm in}/b_{1c}^{\rm in}$. For a specific pump amplitude, the pump detuning for maximum gain is approximately indicated by the white dashed lines. Line cuts of (c) G_s and (d) G_i with $b_1^{\rm in} = 0.5b_{1c}^{\rm in}$ (blue), $0.6b_{1c}^{\rm in}$ (cyan), $0.7b_{1c}^{\rm in}$ (green), $0.8b_{1c}^{\rm in}$ (yellow), $0.9b_{1c}^{\rm in}$ (magenta), and $b_{1c}^{\rm in}$ (red).

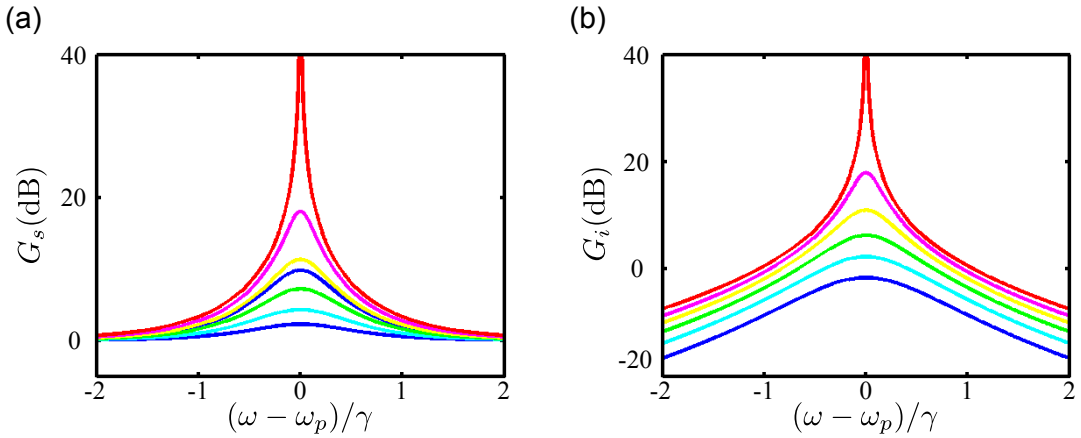

Figure 3.14: Bandwidth of direct gain and intermodulation gain. (a) The direct gain G_s and (b) the intermodulation gain G_i versus the signal detuning $\omega-\omega_p$ for $b_1^{\rm in}=0.5b_{1c}^{\rm in}$ (blue), $0.6b_{1c}^{\rm in}$ (cyan), $0.7b_{1c}^{\rm in}$ (green), $0.8b_{1c}^{\rm in}$ (yellow), $0.9b_{1c}^{\rm in}$ (magenta), and $b_{1c}^{\rm in}$ (red) with the pump detunings chosen as the maximum-gain detuning.

To analyze the noise squeezing, I treat the input $\hat{c}_1^{\rm in}(t)$ and output $\hat{c}_1^{\rm out}(t)$ as quantum operators that satisfy the bosonic commutation relations

$$[\hat{c}_1^{\alpha}(t), \hat{c}_1^{\alpha}(t')] = [\hat{c}_1^{\alpha\dagger}(t), \hat{c}_1^{\alpha\dagger}(t')] = 0, \quad [\hat{c}_1^{\alpha}(t), \hat{c}_1^{\alpha\dagger}(t')] = \delta(t-t'), \tag{3.80}$$

for $\alpha \to {\rm in}, {\rm out}$. The corresponding Fourier component operators defined by Eq. (3.71) satisfy the commutation relations

$$[\hat{c}_1^{\alpha}(\omega), \hat{c}_1^{\alpha}(\omega')] = [\hat{c}_1^{\alpha\dagger}(\omega), \hat{c}_1^{\alpha\dagger}(\omega')] = 0, \quad [\hat{c}_1^{\alpha}(\omega), \hat{c}_1^{\alpha\dagger}(\omega')] = 2\pi\delta(\omega-\omega'), \tag{3.81}$$

for $\alpha \to {\rm in}, {\rm out}$. The inputs are considered to be either thermal or quantum noise, and the expectation values of the input operators are characterized by

$$\langle \hat{c}_1^{\rm in}(\omega)\rangle = 0, \tag{3.82}$$

$$\langle \hat{c}_1^{\rm in}(\omega)\hat{c}_1^{\rm in}(\omega')\rangle = \langle \hat{c}_1^{\rm in\dagger}(\omega)\hat{c}_1^{\rm in\dagger}(\omega')\rangle = 0, \tag{3.83}$$

$$\langle \hat{c}_1^{\rm in\dagger}(\omega)\hat{c}_1^{\rm in}(\omega')\rangle = \frac{1}{{\rm e}^{\frac{\hbar\omega}{k_{\rm B}T}}-1} 2\pi\delta(\omega-\omega'), \tag{3.84}$$

where T is the temperature of the input mode $\hat{c}_1^{\rm in}$.

To analyze the noise fluctuation of the input and output fields, the rotated quadrature operator Eq. (2.9) is generalized for multimode fields. In the pump rotating frame, the rotated quadrature operator is defined as [45]

$$\hat{X}_\theta(t) = \frac{1}{\sqrt{2}}(\hat{c}(t){\rm e}^{-i\theta} + \hat{c}^\dagger(t){\rm e}^{i\theta}), \tag{3.85}$$

where θ is the quadrature phase. Transforming $\hat{X}_\theta(t)$ into the frequency domain, we have

$$\hat{X}_\theta(\omega) = \frac{1}{\sqrt{2}}(\hat{c}(\omega){\rm e}^{-i\theta} + \hat{c}^\dagger(-\omega){\rm e}^{i\theta}). \tag{3.86}$$

I can then express the expectation value $\langle \hat{X}_\theta(t)^2\rangle$ in terms of its spectral density $S_{X_\theta,X_\theta}(\omega)$ as

$$\langle \hat{X}_\theta(t)^2\rangle = \int_0^\infty \frac{{\rm d}\omega}{2\pi} S_{X_\theta,X_\theta}(\omega), \tag{3.87}$$

where $S_{X_\theta,X_\theta}(\omega)$ can be calculated by the anticommutator

$$S_{X_\theta,X_\theta}(\omega)2\pi\delta(\omega-\omega') = \frac{1}{2}\left\langle \{\hat{X}_\theta(\omega), \hat{X}_\theta^\dagger(\omega')\}\right\rangle. \tag{3.88}$$

With input conditions Eqs. (3.82)–(3.84), the input field has zero mean value

$$\langle \hat{X}_{\mathrm{in},\theta}(t) \rangle = 0, \tag{3.89}$$

and the input noise spectral density becomes

$$S_{X_{\mathrm{in},\theta},X_{\mathrm{in},\theta}}(\omega) = \frac{1}{2}\coth\left(\frac{\hbar\omega}{2k_{\mathrm{B}}T}\right). \tag{3.90}$$

For the output field, by using Eq. (3.66), the mean value is apparently zero

$$\langle \hat{X}_{\mathrm{out},\theta}(t) \rangle = 0, \tag{3.91}$$

and the output spectral density is

$$\begin{aligned} S_{X_{\mathrm{out},\theta},X_{\mathrm{out},\theta}}(\omega) &= S_{X_{\mathrm{in},\theta},X_{\mathrm{in},\theta}}(\omega)\frac{1}{2}\begin{pmatrix} |g_s(\omega)|^2 + |g_s(-\omega)|^2 + |g_i(\omega)|^2 + |g_i(-\omega)|^2 \\ +2\mathrm{Re}\left[\mathrm{e}^{-2i\theta}\left(g_s(\omega)g_i(-\omega) + g_s(-\omega)g_i(\omega)\right)\right] \end{pmatrix} \qquad (3.92) \\ &= S_{X_{\mathrm{in},\theta},X_{\mathrm{in},\theta}}(\omega)G_\theta(\omega), \qquad (3.93) \end{aligned}$$

where $G_\theta(\omega)$ is obtained by using Eq. (3.78)

$$G_\theta(\omega) = 2G_s(\omega) - 1 + 2\sqrt{G_s(\omega)}\sqrt{G_s(\omega)-1}\cos\left(2\phi - 2\theta\right), \tag{3.94}$$

with $g_s(\omega)g_i(-\omega) = \sqrt{G_s(\omega)}\sqrt{G_s(\omega)-1}\mathrm{e}^{2i\phi}$. The quadrature phase θ_{amp} at which the maximum of $G_\theta(\omega)$ occurs defines the amplified quadrature X_{amp} with quadrature gain G_{amp}, i.e.,

$$G_{\mathrm{amp}}(\omega) = 2G_s(\omega) - 1 + 2\sqrt{G_s(\omega)}\sqrt{G_s(\omega)-1}. \tag{3.95}$$

The minimum of $G_\theta(\omega)$ defines the squeezed quadrature X_{squ} with quadrature phase $\theta_{\mathrm{squ}} = \theta_{\mathrm{amp}} + \pi/2$ and quadrature squeezing G_{squ}, i.e.,

$$G_{\mathrm{squ}}(\omega) = 2G_s(\omega) - 1 - 2\sqrt{G_s(\omega)}\sqrt{G_s(\omega)-1}. \tag{3.96}$$

The amplification and squeezing satisfy

$$G_{\mathrm{amp}}(\omega)G_{\mathrm{squ}}(\omega) = 1, \tag{3.97}$$

which demonstrates that the parametric amplification process conserves the quadrature uncertainty [Fig. 3.15(a)].

The degree of squeezing for signal frequency $\omega = 0$ versus the pump power is shown in Fig. 3.15(a), and the bandwidth of the squeezing near the critical point is illustrated in Fig. 3.15(b). Both figures show that the quadrature noise can be arbitrarily squeezed for low-frequency signal $\omega \approx 0$. However, practically, issues such as the pump power depletion, pump stabilities, and the loss of the amplifier resonator, limit the maximum degree of squeezing. Moreover, the amplifier saturation effects also prevent us from achieving arbitrarily high squeezing.

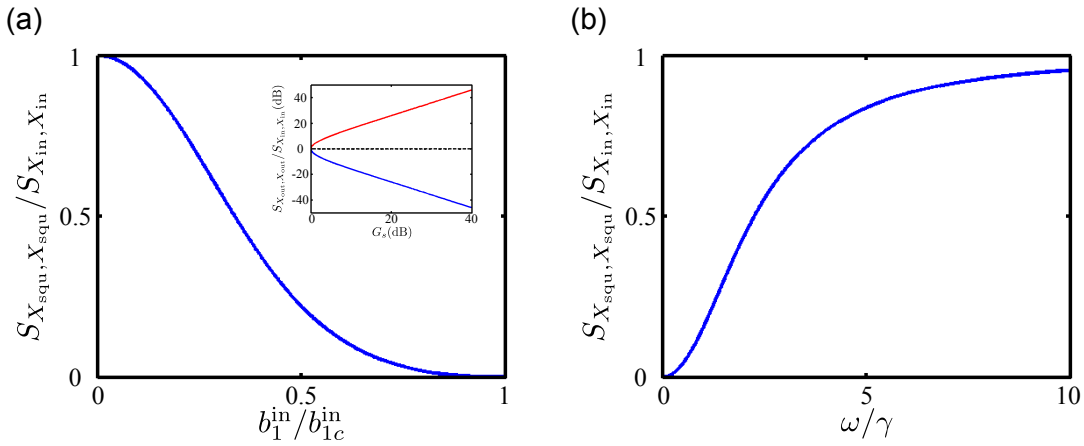

Figure 3.15: Noise Squeezing. (a) The noise spectral density of the output squeezed quadrature $S_{X_{\rm squ},X_{\rm squ}}$ for signal $\omega = 0$ versus pump amplitude $b_1^{\rm in}$. The pump detunings are chosen as the maximum gain detunings for each pump amplitude. Inset: the noise spectral densities of the squeezed quadrature (blue) and the amplified quadrature (red) versus the direct power gain. The products of the two noise spectral densities (dashed black) are constant, illustrating that the noise is conserved. (b) The noise spectral density of the output squeezed quadrature with critical gain versus signal frequencies.

Chapter 4

Design and testing of passive components

To fully exploit the power of microwave circuits, it is important to be able to combine and split itinerant microwave fields. These tasks are accomplished using passive microwave components, particularly directional couplers and hybrids, which act as beam splitters for microwave photons. These components are microwave implementations of the linear optics elements discussed in Sec. 2.2. They provide the ability to manipulate quantum states of itinerant microwave fields. For example, a directional coupler can be used as a tool to shift a quantum state in its phase space, and a two-mode squeezed vacuum state can be generated at the outputs of a hybrid with two single-mode squeezed states as inputs. Although passive microwave components are routinely combined into monolithic microwave integrated circuits [116, 117], they are only now beginning to appear in recent microwave integrated quantum information processing circuits [82]. In order to be integrated with our JPAs and used in quantum information applications, we design, fabricate, and test quadrature hybrids and 20 dB directional couplers.

In the first part of this chapter, I introduce the designs of these two passive components, starting with the basic operation principles. Next, I present the descriptions of the design principles and the detailed design features that improve the performances. I also describe how we optimize the designs by simulating their performances. In the second part of this chapter, I discuss how we measure the fabricated components and calibrate the measurements to extract the intrinsic performances of the devices. Finally, I present the calibrated measured performances of the two passive components.

4.1 Design and simulation of passive components

In this section, I introduce the designs of two passive microwave components, a quadrature hybrid and a 20 dB directional coupler. These passive components are designed to be suitable for integration with JPAs developed in our group and are built to meet the requirements for the application of generating two-mode entanglement. As such, we design them using a coplanar waveguide (CPW) architecture [118, 119] from superconducting niobium metals. They also must have low loss and high isolation, but only need to be working in a 10% band around a specific frequency between 6 and 7 GHz. In the following, I describe the design we use to achieve the required performances, the simulations to optimize the designs, and the layer structures of the devices.

4.1.1 Design of a quadrature hybrid

Essentially, a quadrature hybrid is a microwave equivalent of a 50:50 beam splitter. It can be used as a tool to combine the two input itinerant microwave states and create correlation between the two output states. With nonclassical input states, such as squeezed states, the two outputs will be in a two-mode entangled state. Its operation is illustrated by Fig. 4.1(a), which is also the symbol we use for a quadrature hybrid. Power injected to port 1 (the input port) is evenly transmitted to port 2 (the through port) and port 3 (the coupled port) with a 90° phase difference between the two output ports (It is this phase difference that makes a hybrid a *quadrature* hybrid.). Ideally, no power is transmitted to port 4 (the isolation port). Thus an ideal quadrature hybrid is a 4-port network with a S-matrix [120]:

$$[S] = \frac{-1}{\sqrt{2}} \begin{bmatrix} 0 & j & 1 & 0 \\ j & 0 & 0 & 1 \\ 1 & 0 & 0 & j \\ 0 & 1 & j & 0 \end{bmatrix}.$$

A specific element of an S-matrix is defined as

$$S_{ij} = \left.\frac{V_i^-}{V_j^+}\right|_{V_k^+=0 \text{ for } k\neq j}, \tag{4.1}$$

where V_j^+ is the amplitude of the voltage wave incident on port j, and V_i^- is the amplitude of the voltage wave coming out of port i.

The quadrature hybrid is implemented with a structure known as a branch-line coupler [120, 118]. It consists of two through lines with characteristic impedance $\frac{Z_0}{\sqrt{2}}$ connected by two branch lines with characteristic impedance Z_0, where $Z_0 = 50\ \Omega$ is the characteristic impedance of the transmission lines used in our microwave system. Thus, the initial dimensions of the hybrids are chosen such that the impedances of the through lines and the branch lines are 35 Ω and 50 Ω, respectively. This configuration achieves 3 dB coupling and can be matched a 50 Ω transmission line [Fig. 4.1(c)]. Moreover, both the branch and through lines are a quarter wavelength long at 7 GHz, making the center frequency of the hybrid approximately 7 GHz.

Although CPW transmission lines are commonly used in making superconducting qubits or JPAs, they are not ideal geometries for passive components. In particular, when using CPW lines to create a branch line coupler, one creates a floating metal square, which should be grounded. In order to ground the center square, we short the two ground planes, using bridges made in a second metal layer, at 4 T-junctions of the designed hybrid. These bridges also suppress the slotline modes of CPW lines [Fig. 4.1(e)].

4.1.2 Design of a 20 dB directional coupler

A directional coupler is an asymmetric beam splitter. We use it to add a coherent amplitude to a quantum state. This process displaces the state in its phase space. In our experiments, we often use a directional coupler to remove the displacement of the displaced squeezed state generated by a JPA. It is also the device through which we introduce the intense pump to a JPA. With reference to Fig. 4.1(b), the operation of a directional coupler is as follows: a small amount of input power injected through port 1 (the input port) is coupled to port 3 (the coupled port) with a power

coupling factor β^2, while the remainder of the input power is delivered to port 2 (the through port) with a power transmitting factor $\alpha^2 = 1 - \beta^2$. No power is delivered to port 4 (the isolation port) for an ideal directional coupler. The S-matrix of this 4-port device is [120]:

$$[S] = \begin{bmatrix} 0 & \alpha & j\beta & 0 \\ \alpha & 0 & 0 & j\beta \\ j\beta & 0 & 0 & \alpha \\ 0 & j\beta & \alpha & 0 \end{bmatrix}.$$

The directional coupler is realized by coupling a pair of CPW transmission lines and is referred as a coupled-line directional coupler [120, 118]. The physical layout of a coupled-line directional coupler using CPW architecture is shown in Fig. 4.1(d). Generally, this CPW structure supports two normal modes: the even and the odd mode. The design equations for the required even-mode impedance Z_{0e} and odd-mode impedance Z_{0o} are:

$$Z_{0e} = Z_0 \sqrt{\frac{1+\beta}{1-\beta}}, \tag{4.2}$$

$$Z_{0o} = Z_0 \sqrt{\frac{1-\beta}{1+\beta}}. \tag{4.3}$$

According to these equations, to design a 20 dB directional coupler ($\beta^2 = 0.01$) matched to a $Z_0 = 50\ \Omega$, the initial dimensions of the coupled-line CPW are chosen such that $Z_{0e} = 55\ \Omega$ and $Z_{0o} = 45\ \Omega$. The chosen dimensions also result in a difference between the even-mode and odd-mode phase velocities of less than 1%, which is a requirement to achieve good directivity. Similar to the hybrid, the coupler is a quarter wavelength long at 7 GHz.

To improve the performance of the designed directional coupler using CPW, we add two more design features. Bridges designed to short the two ground planes of the CPWs are placed at CPW 90° bends to suppress the parasitic slot line mode. Furthermore, the narrowed CPW center conductors are used to compensate the parasitic capacitance added by the bridges and the 90° bend reactance [Fig. 4.1(f)] [121].

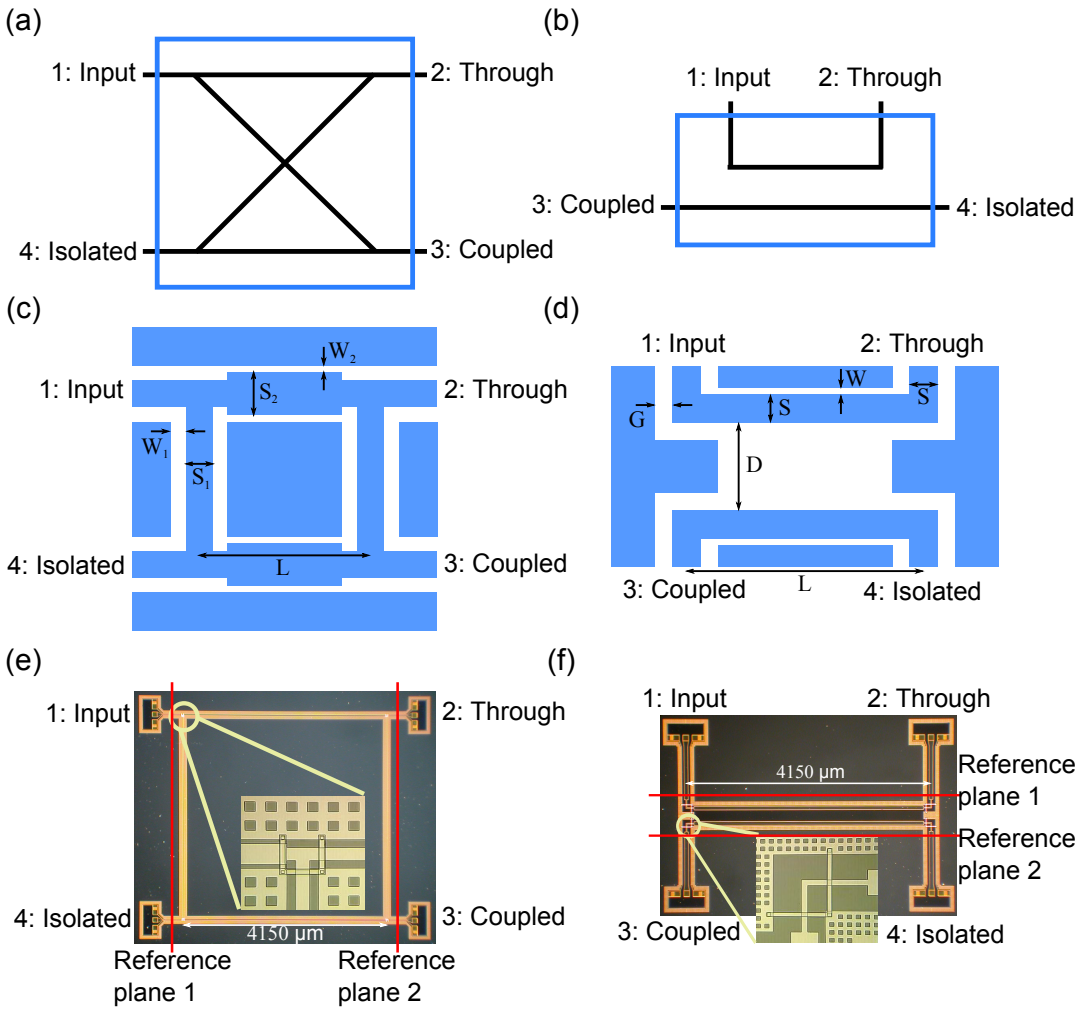

Figure 4.1: Passive components. (a) The symbol we use to represent a quadrature hybrid with port definitions. (b) The symbol we use to represent a 20 dB directional coupler with port definitions. (c) Physical layout of the quadrature hybrid. The blue areas represent superconducting metal, and the white areas indicate the regions where the metal is removed exposing insulating substrate. These diagrams are not to scale; the indicated dimensions are $S_1 = 14\ \mu$m, $W_1 = 8\ \mu$m, $S_2 = 23\ \mu$m, $W_2 = 3.5\ \mu$m, and $L = 4150\ \mu$m. (d) Physical layout of the directional coupler with the following indicated dimensions: $D = 200\ \mu$m, $S = 65\ \mu$m, $W = 15\ \mu$m, $G = 40\ \mu$m, and $L = 4150\ \mu$m. (e) Photograph of the quadrature hybrid. The inset shows bridges and ground plane meshes to suppress the motion of the trapped magnetic flux. In the inset, the lighter material is niobium, and the darker material is the insulating substrate. (f) Photograph of the 20 dB directional coupler. The inset shows similar bridges and ground plane meshes, as well as the narrowed center conductor at the corners. In (e) and (f) the red lines indicate the reference planes for the two devices of the calibration procedure.

4.1.3 Simulation and fabrication

We optimize the designs of the hybrid and coupler by simulating their performances using AWRs Microwave Office software. We then make fine adjustments to the layout dimensions to compensate for the effects of the T-junctions in the quadrature hybrid and the 90° bends in the directional coupler. The optimization procedure is repeated until the simulations indicate that the desired performance has been achieved. For the directional coupler, we can simulate and optimize its entire structure. In contrast, the quadrature hybrid is too complex to simulate the entire structure at once because of the small features of the bridges compared to the whole structure. To overcome this problem, the hybrid is divided into eight parts: 4 T-junction elements, 2 through-line elements, and 2 branch-line elements. After simulating each element separately, these elements are combined and simulated as a microwave network.

The simulated performances for the final designs of the two passive components are shown in Fig. 4.3(a,b). To characterize the performance of the two passive components, we define: return loss $= -20\log|S_{11}|$, through transmission $= -20\log|S_{21}|$, coupling $= -20\log|S_{31}|$, isolation $= -20\log|S_{41}|$, and directivity $= 20\log\frac{|S_{31}|}{|S_{41}|}$. For the hybrid, the designed through transmission and coupling are both 3 ± 0.3 dB in a 700 MHz band around 7 GHz. The return loss and isolation both are better than 20 dB in the same band. For the directional coupler, the designed coupling is 20 ± 1 dB with both return loss and isolation better than 40 dB from 6 to 8 GHz.

Because the passive components are intended to be integrated with our JPAs, our test devices are fabricated with the same niobium process [122] as is used to fabricate JPAs. The circuit pattern layer is a 200 nm thick niobium film deposited onto a high-resistivity silicon wafer (resistivity $>$ 17 kΩ·cm) with 20 nm of SiO_2 thermally grown on its surface. A 350 nm thick SiO_2 layer is then deposited and etched to form the insulation layer between the circuit layer and a wiring layer of 300 nm thick niobium. Bridges are patterned into the wiring layer, where niobium vias through the insulation layer connect the circuit layer and wiring layer. For reliable contact between the microwave probes and test devices, a gold layer is deposited on the niobium circuit layer in

the region that forms the probe pads. In addition to the test devices, we also fabricate the TRL calibration standards and a high Q half-wavelength CPW resonator on the same test chip. The high Q resonator is designed for diagnosing the losses of the materials. Including all of these elements, the size of the test chip is 1.5 cm $\times$ 1.9 cm, which still fits the probing range of the probe station we use.

4.2 Testing and calibration of passive components

A general problem for measuring microwave networks is how to extract intrinsic performances of the devices from the effect of the instruments and cables used to test the devices. The procedure for de-embedding the behavior of the measured device from its testing apparatus is called calibration. In this section, I describe the apparatus we use to test the fabricated devices and how we perform the calibration procedure. Finally, I report the calibrated performance of the two passive components.

4.2.1 TRL Calibration

We use a procedure called Thru-Reflect-Line (TRL) calibration [123, 120] to characterize the effects of the measurement apparatus. The common Short-Open-Load-Through (SOLT) calibration method for coaxial transmission lines is difficult to apply in CPW structures because it requires three lumped elements that usually are difficult to fabricate with accurate impedances. Instead, the TRL technique can be used to calibrate devices fabricated in CPW architecture with three simple connections: the $Thru$, the $Reflect$, and the $Line$. The TRL method does not rely on the accuracy of known loads, but uses these three connections to extract the intrinsic performances of the devices under test.

In order to implement the TRL calibration, we co-fabricate sets of TRL calibration standards with the passive components on the same chip. The calibration standards comprise three elements (Fig. 4.4): a section of transmission line providing the $Thru$ element, a short circuit providing the $Reflect$ element, and a longer section of transmission line, which is a quarter wavelength longer

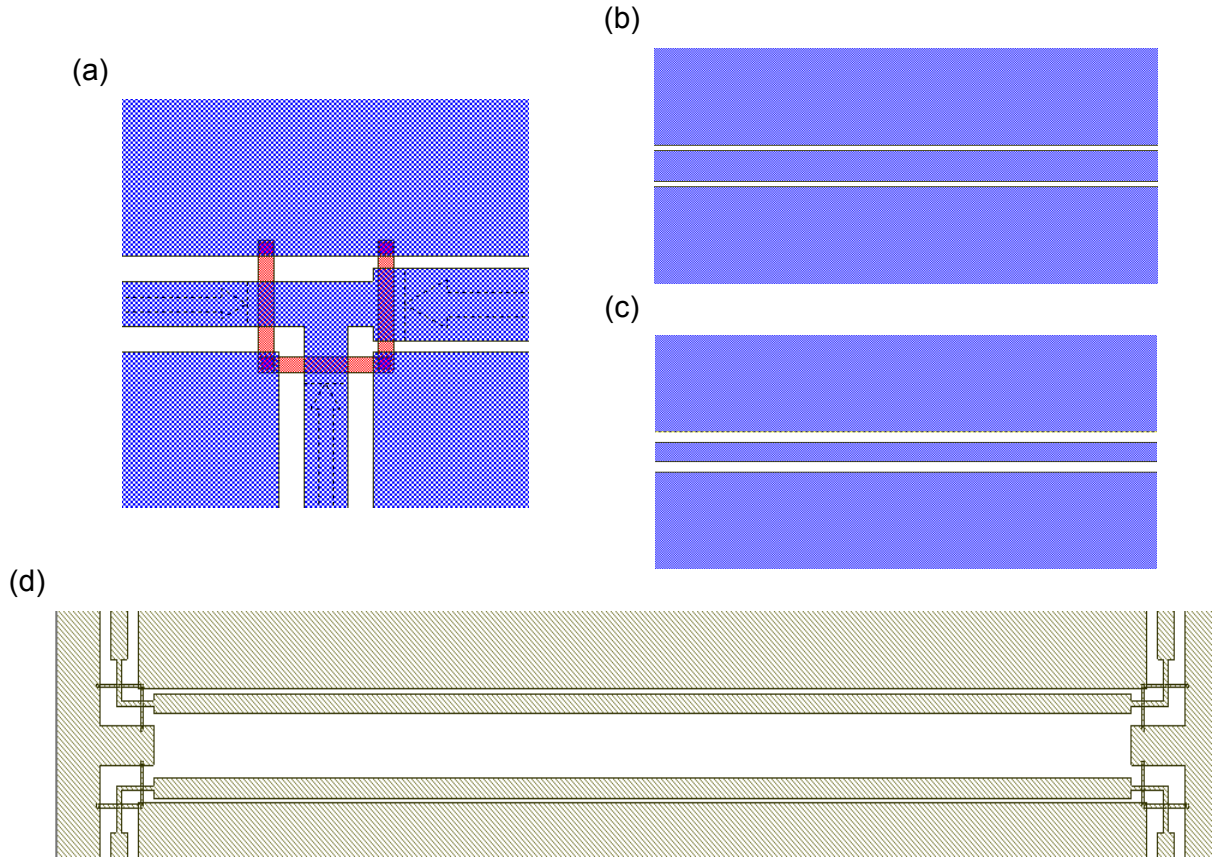

Figure 4.2: Simulation layouts of the passive components. The simulation of the quadrature hybrid is divided into three building blocks: (a) a T-junction, (b) a 35 Ω transmission line, and (c) a 50 Ω transmission line. (d) Simulation layout of a 20 dB direction coupler.

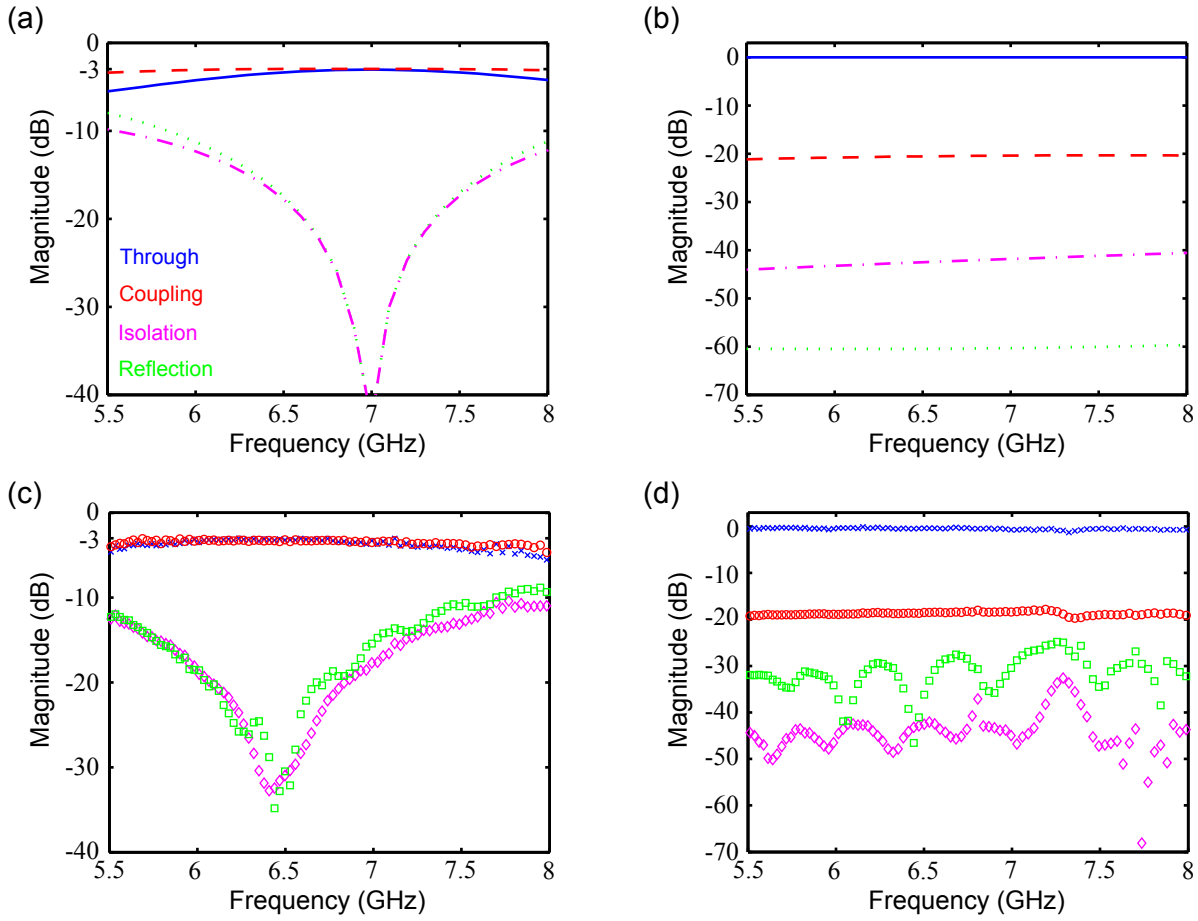

Figure 4.3: Simulated and measured performance of passive components. The magnitude of the simulated S-parameters of (a) the quadrature hybrid and (b) the 20 dB directional coupler showing the fraction of the input power that exits the following: through port (blue solid line), coupled port (red dashed line), isolated port (magenta dash-dot line), and input port (green dotted line). The magnitude of the measured S-parameters of (c) the quadrature hybrid and (d) the 20 dB directional coupler through transmission (blue cross), coupling (red circle), isolation (magenta diamond), and reflection (green square). The measurements shown here are calibrated by measuring the on-chip TRL calibration standards.

than the *Thru*, providing the *Line* element. After measuring the uncalibrated performance of a passive component and the TRL elements, and then applying the calibration algorithm, we can extract the microwave performance of the structure that lies between two so-called reference planes, as shown in Fig. 4.1(e,f). In TRL calibration, the reference plane is defined by the symmetry plane of the *Thru*. In order to improve the quality of calibration, alignment marks are patterned into the probe-pads so that probes can be positioned on the pads reproducibly. Because our custom TRL standards are fabricated with the same probe-pads and tapered CPWs as the passive components, the effects of probe-to-CPW transition can be removed, allowing us to extract the true microwave performance of the passive components between the two reference planes.

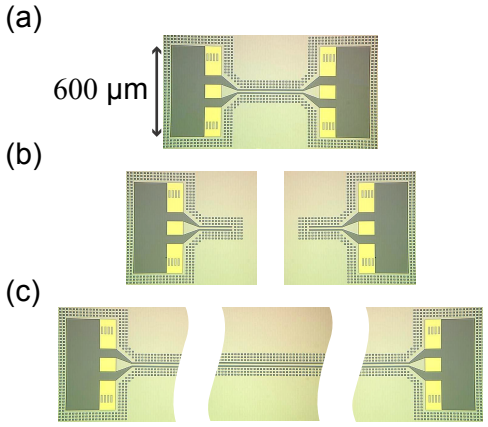

Figure 4.4: The custom TRL calibration standards for the quadrature hybrid. (a) Thru standard. (b) Reflect standard: two identical CPW short circuits. (c) Line standard. The lighter material is niobium, and the darker material is the insulating substrate. The yellow regions at the two ends are gold patterned into probe pads with alignment marks. A similar set of TRL standards but with different CPW dimensions was fabricated for the coupler (not shown).

4.2.2 Measurement apparatus and scheme

I measure the microwave performances of the passive components with a cryogenic microwave probe station system (Desert Cryogenics TT-Prober System), which can reach 4 K temperature allowing the study of niobium passive components in their superconducting state [Fig. 4.5(a,b)]. In order to calibrate the passive components with high accuracy, a cryogenic microwave probe station

is essential. The station has four straight arms connected to four microwave cryogenic probes. These microwave probes [Picoprobe P-10-5325-4 (straight probe) and Picoprobe P-10-5325-B (90°-probe)] are GSG (Ground-Signal-Ground) probes, which naturally launch CPW modes [Fig. 4.5(c)]. Because the four probe arms are 90° apart from one another, two 90° probes and two straight probes are used to match the distribution of ports on the device (two ports on one side and two ports on the opposite side). Microwave probes contacting the probe pads provide a high-quality, reproducible connection between the network analyser cables and the test devices. The quality and reproducibility of this contact is critical because the calibration procedure assumes that the contact made to the TRL standards is identical to the contact made to the passive components. Unfortunately, using 90° probes decreases the calibration accuracy because of the poor planarity adjustment of probe tips that have a 90° bend.

Measurements are made by connecting a two-port vector network analyzer (Agilent N5230A PNA-L) to two of the four ports of a component via a pair of calibrated microwave probes. The remaining two ports are contacted by probes that are terminated in 50 Ω resistors. The network analyser is then used to measure the S-parameters of the two connected ports. This procedure is repeated for all possible pairs of probes. In this manner, the full 4×4 S-matrix is determined. An important limitation of this measurement scheme arises because pairs of probes on the same side of a device can not be calibrated as the TRL standards themselves have probe pads on opposite sides. To calibrate probes on the same side, we calibrate one of the probes by using the calibration of the same type of probe on the opposite side. In addition, this procedure assumes that the unmeasured ports are in fact terminated in exactly 50 Ω.

4.2.3 Calibrated performance

By applying the TRL calibration algorithm, we are able to calculate the S-parameters of the measurement apparatus and use them to calculate the calibrated performances of the passive components. The calibrated measurements of the quadrature hybrid are shown in Fig. 4.3(c), indicating the isolation $>$ 20 dB in a 700 MHz band and the return loss $>$ 20 dB in a 550 MHz

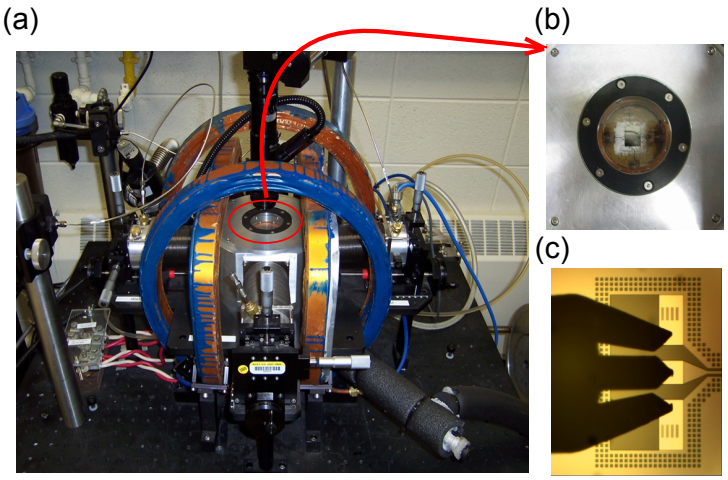

Figure 4.5: (a) Photograph of cryogenic microwave probe station system used to measured the test chip. (b) View from the top window on the vacuum chamber of the probe station. The test chip is indium soldered to the cold plate of the station. (c) A GSG probe is landing on the probe pads of one test device.

band around 6.5 GHz. The through transmission and coupling are 3.1 dB and 3.3 dB at 6.5 GHz, respectively. Strikingly, the observed hybrid center frequency is 500 MHz below the design value. This center frequency shift is likely caused by a poorly modeled reactance at the T-junctions in the CPW structures. This poorly modeled reactance may arise from dividing the entire hybrid structure into smaller parts for simulation.

The calibrated measurements of the directional coupler are shown in Fig. 4.3(d). The coupling is around 19 dB in a 2 GHz band around 6 GHz. The isolation is 40 dB (which means the directivity is 21 dB), and the return loss is 30 dB in the same band except around 7.3 GHz. There is a weak resonant feature around 7.3 GHz, whose origin is unknown. We believe that this is a real resonance in the physical geometry of the coupler, not a flaw in the calibration.

The period of the oscillations in the return loss (400 MHz) is too small to be caused by reflections on the chip. Rather they almost certainly result from a small standing wave component in the measurement cables that is not perfectly calibrated away. The observed return loss of 30 dB for both the hybrid and the coupler is consistent with the specified 30 dB return loss of the microwave probes used to terminate the two unmeasured ports. Measurements from both components show insertion loss [defined as: $-20\log(|S_{21}| + |S_{31}|)$] 0.3 dB. We believe that the 0.2 dB insertion loss that we do observe is not a consequence of power absorbed in the dielectric or conductors because the intrinsic loss of the cofabricated resonator yields a $Q > 10,000$. Losses might arise from coupling of the CPW modes to other modes, (including to free space modes), especially at the elbow structures.

The intrinsic performances of these components are within the design goals for the application of entanglement generation. Both devices are appropriate for being integrated with JPAs whose center frequency can by widely tuned. Furthermore, they may be well suited for use in other experiments that study the quantum optics of microwave circuits.

Chapter 5

Designs of tunable Kerr circuits

A tunable Kerr circuit (TKC) is the critical element of a Josephson parametric amplifier (JPA). It is a nonlinear resonant circuit where the nonlinearity is provided by an embedded array of superconducting quantum interference devices (SQUIDs). The SQUID array behaves as a nonlinear inductor where the inductance is proportional to the intensity rather than the amplitude of the current flowing through it. In analogy with an optical Kerr medium, this nonlinear effect is referred as a Kerr nonlinearity. Furthermore, because the effective inductance of a SQUID is a function of the magnetic flux threading it (Eq. 3.13), we can tune the resonant frequency of the circuit by applying a magnetic field to the SQUID loops, which greatly improves the usefulness of the JPA.

In the experiment of two-mode entanglement, two versions of TKCs are used to form JPAs. The transmission line resonator is integrated with passive components into a entangler chip to generate the entangled states. The lumped-element LC resonator is used in building the measurement apparatus to verify the entangled states. The LC resonator is much smaller in size as compared to the transmission line resonator.

Here, I describe the designs of both TKCs. I begin with a review of transmission line theory and a discussion of microwave resonators. Following that I present the designs of the nonlinear resonators built by incorporating SQUID arrays into the resonators. Finally, I discuss the designs of on-chip DC bias lines through which we can inject bias currents to tune the resonance frequencies of the nonlinear resonators.

5.1 Microwave environment

In the microwave regime, the electromagnetic fields are carried by transmission lines rather than ordinary conducting cables for low-frequency currents. Because the cable length is a significant fraction of the wavelength of the transmitted signal, the wave nature of the electromagnetic signals become important and the transmission line theory is necessary.

A transmission line is a specially designed structure, which usually consists of two conductors, to guide the electromagnetic waves. Moreover, by having two discontinuities separated by a length on a transmission line, we can construct an electrical resonant circuit analogous to a Fabry-Pérot cavity built with two mirrors in optics.

In this section, I review the basic theory of transmission lines and introduce the figures for characterizing a transmission line. I then discuss the useful expressions for the design of transmission line resonators.

5.1.1 Transmission line theory

At microwave frequencies, the physical size of the electronic components is comparable to the electrical wavelength. DC circuit theory is no longer valid for analyzing a microwave network. Both the magnitude and the phase of the voltage and current waves can vary over the length of a transmission line. Generally, the voltage and current waves traveling on a transmission line can be expressed as

$$V(x) = \quad V_o^+ \mathrm{e}^{-\gamma x} + V_o^- \mathrm{e}^{\gamma x}, \tag{5.1}$$

$$I(x) = \quad I_o^+ \mathrm{e}^{-\gamma x} + I_o^- \mathrm{e}^{\gamma x}, \tag{5.2}$$

where V_o^+ (I_o^+) and V_o^- (I_o^-) are the amplitudes of the voltage (current) waves propagating in the $+x$ and $-x$ directions, respectively, and γ is the complex propagation constant [Fig. 5.1(a)]. A transmission line is modeled as a distributed-parameter network [120], as shown in [Fig. 5.1(b)]. The analysis of this transmission line model for time-harmonic signals gives us the wave equations

thatsupport the voltage [Eq. (5.1)] and the current waves [Eq. (5.2)], i.e.,

$$\frac{\partial^2 V(x)}{\partial x^2} - \gamma^2 V(x) = 0, \tag{5.3}$$

$$\frac{\partial^2 I(x)}{\partial x^2} - \gamma^2 I(x) = 0. \tag{5.4}$$

The complex propagation constant γ can then be expressed in terms of the circuit parameters as

$$\gamma = \alpha + j\beta = \sqrt{(R + j\omega L)(G + j\omega C)}, \tag{5.5}$$

where R, L, G, C are the series resistance, the series inductance, the shunt conductance, and the shunt capacitance per unit length of the transmission line. The voltage and the current are related by the characteristic impedance Z_0 of the transmission line as

$$Z_0 = \frac{V_o^+}{I_o^+} = \frac{-V_o^-}{I_o^-}, \tag{5.6}$$

where the impedance Z_0 is calculated by

$$Z_0 = \sqrt{\frac{R + j\omega L}{G + j\omega C}}. \tag{5.7}$$

We can also calculate the wavelength λ and the phase velocity v_p of the waves traveling on the transmission line

$$\lambda = \frac{2\pi}{\beta}, \tag{5.8}$$

$$v_p = \frac{\omega}{\beta}. \tag{5.9}$$

Usually, a transmission is used to transmit electric waves to a load. Considering that we terminate a transmission line with an arbitrary load impedance Z_L at $x = 0$, as shown in Fig. 5.1(c), the amplitudes of the transmitted V_o^+ and reflected V_o^- waves can then be related via the voltage reflection coefficient Γ at the load end:

$$\Gamma = \frac{V_o^-}{V_o^+} = \frac{Z_L - Z_0}{Z_L + Z_0}. \tag{5.10}$$

The input impedance of this terminated transmission line is calculated as

$$Z_{\text{in}}(l) = Z_0 \frac{1 + \Gamma e^{-2\gamma l}}{1 - \Gamma e^{-2\gamma l}}, \tag{5.11}$$

or expressed in terms of the load impedance

$$Z_{\text{in}}(l) = Z_0 \frac{Z_L + Z_0 \tanh \gamma l}{Z_0 + Z_L \tanh \gamma l}. \tag{5.12}$$

If the transmission line is lossless, the input impedance can be rewritten as

$$Z_{\text{in}}(l) = Z_0 \frac{Z_L + jZ_0 \tan \beta l}{Z_0 + jZ_L \tan \beta l}. \tag{5.13}$$

With these expressions , I can explain how we build microwave resonant circuits with terminated transmission lines.

5.1.2 Microwave resonant circuits

A electromagnetic resonator is a device can store energy when it is on resonance. The stored energy oscillates between the electric and the magnetic energy with the resonance frequency. To make a JPA, I design the resonant circuits to enhance the nonlinear parametric process. I start my discussion of our microwave resonator with its lumped-element model, as shown in Fig. 5.2(a). It is a parallel RLC resonant circuit. The total impedance of the parallel RLC circuit is

$$Z_{\text{in}} = (\frac{1}{j\omega L_0} + j\omega C_0)^{-1}, \tag{5.14}$$

and the resonant frequency ω_0 is

$$\omega_0 = \frac{1}{\sqrt{L_0 C_0}}. \tag{5.15}$$

When $\omega \approx \omega_0$, the impedance is approximated as

$$Z_{\text{in}} \approx \frac{1}{j2C_0(\omega - \omega_0)}. \tag{5.16}$$

This near-resonance impedance expression is useful for mapping a distributed-element resonator to a lumped-element one.

We couple the resonant circuit to a voltage generator via the coupling capacitor, C_c, shown in Fig. 5.2(a). To analyze the whole circuit model, I consider the input impedance of the coupled parallel RLC circuit

$$Z_{\text{in}} = R_g + \frac{1}{j\omega C_c} + (\frac{1}{R_0} + \frac{1}{j\omega L_0} + j\omega C_0)^{-1}. \tag{5.17}$$

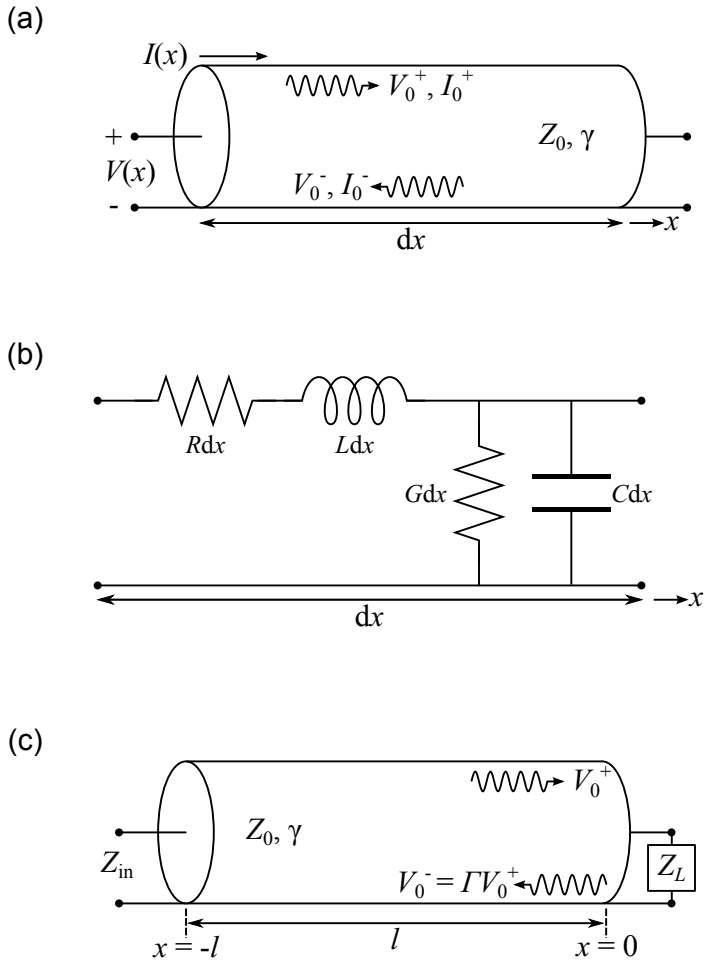

Figure 5.1: Transmission line model. (a) Definitions of voltage and current on a transmission line, which is characterized by its characteristic impedance Z_0 and complex propagation constant γ. (b) The distributed model of a unit-length transmission line consisting of the series resistance R, the series inductance L, the shunt conductance G, and the shunt capacitance C per unit length. (c) The transmission line of length l is terminated with a load impedance Z_L, which determines the voltage reflection coefficient Γ.

The resonance occurs when $\mathrm{Im}(Z_{\mathrm{in}}) = 0$, which results in the resonance frequency of the coupled resonator ω_{res}, i.e.,

$$\omega_{\mathrm{res}} \approx \frac{1}{\sqrt{L_0(C_0 + C_c)}}, \tag{5.18}$$

for a low internal loss resonator ($R_0 \to \infty$). The resonance frequency ω_{res} shows that the coupling capacitor has the effect of lowering the resonance frequency.

When discussing a resonator, we usually define a quality factor Q as

$$Q = \omega_{\mathrm{res}}\tau_{1/\mathrm{e}} = \omega_{\mathrm{res}}\frac{\text{Energy stored}}{\text{energy loss per second}}, \tag{5.19}$$

where $\tau_{1/\mathrm{e}}$ is the time for the stored energy to decay to 1/e of its initial value. Physically, the quality factor represents how many oscillations a cavity field can perform before it dies out. In other words, the Q factor indicates the rate of energy loss relative to the stored energy of the resonator. The mechanisms of the energy dissipation can be categorized into the external and the internal loss. Thus, the total Q of the resonator can be separated into Q_{ext} and Q_{int}, which correspond to energy decay in the resonator due to the energy coupled to the external environment and due to the internal loss of the resonator, i.e.,

$$\frac{1}{Q} = \frac{1}{Q_{\mathrm{ext}}} + \frac{1}{Q_{\mathrm{int}}}, \tag{5.20}$$

respectively. I calculate the Q_{ext} and Q_{int} of the coupled parallel RLC circuit by using circuit theory and obtain

$$Q_{\mathrm{int}} = \frac{R_0}{\omega_{\mathrm{res}}L_0} = \omega_{\mathrm{res}}R_0(C_c + C_0), \tag{5.21}$$

$$Q_{\mathrm{ext}} \approx \frac{C_0+C_c}{\omega_{\mathrm{res}}R_g C_c^2}. \tag{5.22}$$

The resonator is classified into three regimes based on the relations between its Q_{ext} and Q_{int}. If $Q_{\mathrm{ext}} > Q_{\mathrm{int}}$, the resonator is said to be undercoupled. If $Q_{\mathrm{ext}} < Q_{\mathrm{int}}$, the resonator is overcoupled. If $Q_{\mathrm{ext}} = Q_{\mathrm{int}}$, the resonator is critically coupled.

We implement the resonant circuit with a section of transmission line terminated in an inductor L_t, as shown in Fig. 5.2(b). The length l of the transmission line is a quarter wavelength

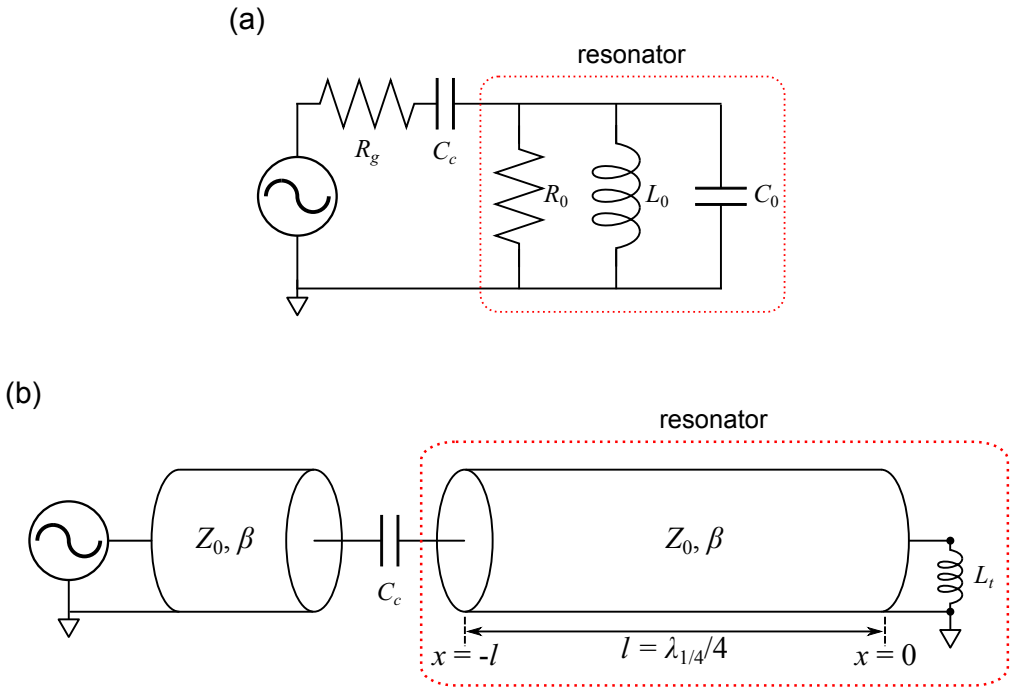

Figure 5.2: Models of the microwave resonators. (a) A lumped-element parallel RLC resonance circuit is coupled to a generator via a coupling capacitor C_c. (b) A distributed-element resonator is formed by a transmission line of length l terminated with a inductor L_t. It is coupled to a feedline via a coupling capacitor C_c.

at frequency $\omega_{1/4}$. Assume that the transmission line is lossless, the input impedance of this terminated transmission line can be calculated by using Eq. (5.13):

$$Z_{\text{in}}(\omega) = Z_0 \frac{j\omega L_t + jZ_0 \tan\beta l}{Z_0 - \omega L_t \tan\beta l} = \frac{Z_0}{j(\frac{b_l - \cot\beta l}{b_l \cot\beta l + 1})}, \tag{5.23}$$

where $b_l = \omega L_t / Z_0$ is the normalized reactance of the terminated inductor. The resonance occurs when $\text{Im}(Z_{\text{in}}) \to \infty$, which yields the following resonance condition

$$\cot\beta l = b_l. \tag{5.24}$$

Generally, this transcendental equation needs to be solved numerically or graphically, as illustrated in Fig. 5.3. However, for the case of small terminated inductance ($b_l \ll 1$), we can approximately solve it by using $\cot\beta l \approx -\Delta\omega\sqrt{LC}l$, where $\Delta\omega = \omega - \omega_{1/4}$. I then derive the approximate resonance frequency

$$\omega_0 \approx \frac{\omega_{1/4}}{1 + \frac{L_t}{Ll}}. \tag{5.25}$$

A useful technique for designing a distributed-element resonator is to map its near resonance behavior to a lumped-element circuit. To do that, I expand the denominator of $Z_{\text{in}}(\omega)$ around the resonance frequency ω_0, i.e.,

$$Z_{\text{in}}(\omega) \approx \frac{Z_0}{j\pi(\omega - \omega_0)/(2\omega_0)}. \tag{5.26}$$

The expression of the impedance is in the same form as Eq. (5.16). Thus I can then map the terminated transmission line to a parallel RLC circuit with the following circuit parameters

$$C_0 = \frac{\pi}{4\omega_0 Z_0}, \tag{5.27}$$

$$L_0 = \frac{1}{\omega_0^2 C_0}. \tag{5.28}$$

I then consider the effect of coupling the terminated transmission line to a feedline via a coupling capacitor C_c. The total input impedance is

$$Z_{\text{in}} = -\frac{j}{\omega C_c} + Z_0 \frac{j\omega L_t + jZ_0 \tan\beta l}{Z_0 - \omega L_t \tan\beta l} = (-\frac{1}{b_c} + \frac{b_l \cot\beta l + 1}{\cot\beta l - b_l}) Z_0 j, \tag{5.29}$$

where $b_c = \omega C_c Z_0$ is the normalized susceptance of the coupling capacitor. Similarly, the resonance occurs on $\mathrm{Im}(Z_{\mathrm{in}}) = 0$, which yields the resonance condition

$$\cot \beta l = \frac{b_l + b_c}{1 - b_l b_c}. \tag{5.30}$$

The graphic solution of this transcendental equation is shown in Fig. 5.3. For the situation with small terminated inductance ($b_l \ll 1$) and small coupling capacitance ($b_c \ll 1$), I derive the approximated resonance frequency by again using $\cot \beta l \approx -\Delta\omega\sqrt{LC}l$. Thus

$$\omega_{\mathrm{res}} \approx \frac{\omega_{1/4}}{1 + \frac{L_t}{Ll} + \frac{C_c}{Cl}}. \tag{5.31}$$

I also use the technique of mapping the transmission line resonator to a lumped-element circuit to estimate its properties. After obtaining the circuit parameters of the lumped-element model via Eqs. (5.27)–(5.28), I calculate the resonance frequency ω_{res} and Q_{ext} of the coupled transmission line resonator with Eq. (5.18) and Eq. (5.22), respectively.

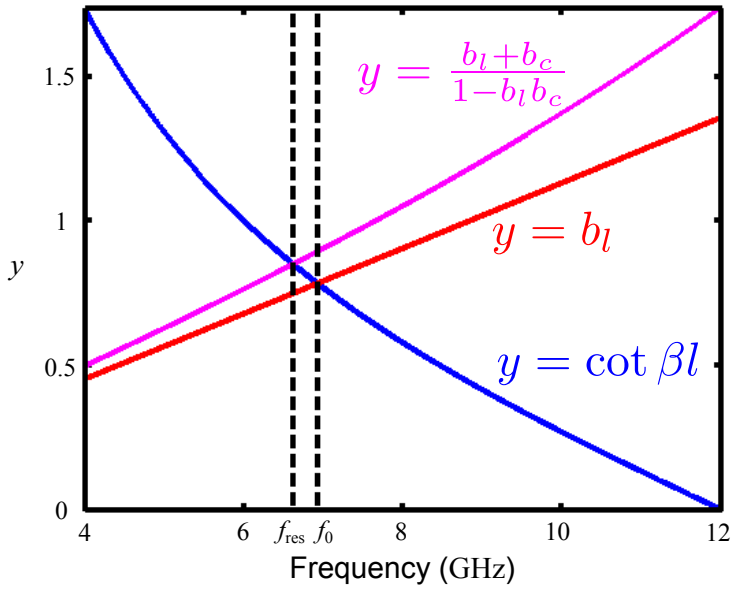

Figure 5.3: Resonance conditions. The resonance solutions $f_0 = 6.93$ GHz for Eq. (5.24) and $f_{\mathrm{res}} = 6.62$ GHz for Eq. (5.24) are graphically solved by the intersections. The circuit parameters used in this example are: $Z_0 = 50$, $v_p = 2 \cdot 10^8$ m/s, $L_t = 0.9$ nH, $C_c = 30$ fF, and the length l is a quarter wavelength at $\omega_{1/4} = 2\pi \cdot 12$ GHz.

The key difference between a lumped-element circuit and a transmission line resonator is

that the field amplitudes inside the transmission line cavity are distributed over the length of the resonator. The voltage and the current profile within the resonator can be calculated by using the transmission line theory [120]:

$$V(x) = V_{\rm in}\frac{S_{21}^C e^{-j\beta l}}{1-S_{22}^C\Gamma_L e^{-2j\beta l}}(e^{-j\beta x}+\Gamma_L e^{j\beta x}), \tag{5.32}$$

$$I(x) = I_{\rm in}\frac{S_{21}^C e^{-j\beta l}}{1-S_{22}^C\Gamma_L e^{-2j\beta l}}(e^{-j\beta x}-\Gamma_L e^{j\beta x}), \tag{5.33}$$

where $V_{\rm in}$ and $I_{\rm in}$ are the amplitudes of the incoming voltage and current wave impinging on the resonator, and Γ_L is the reflection coefficient of the terminated inductor. These field profiles are plotted in Fig. 5.4. I also derive the reflection coefficient of the coupled transmission line resonator $\Gamma_{\rm res}$:

$$\Gamma_{\rm res} = S_{11}^C + \frac{S_{21}^C S_{12}^C \Gamma_L e^{-2j\beta l}}{1-S_{22}^C\Gamma_L e^{-2j\beta l}}. \tag{5.34}$$

In the above expressions, S_{11}^C, S_{21}^C, S_{12}^C, and S_{22}^C are the elements of the S-matrix for the coupling capacitor C_c.

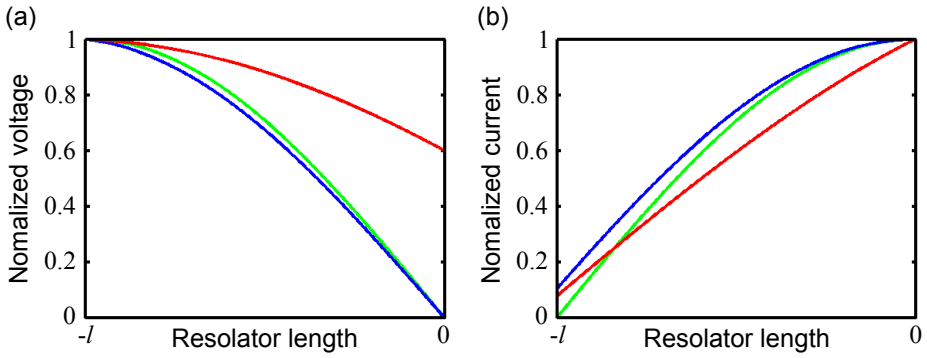

Figure 5.4: Profiles of the resonant field. The (a) voltage and (b) current profile within the transmission line resonator on its resonance. The circuit parameters used for the red curves are the same values as used in Fig. 5.3. The blue curves are profiles with $L_t = 0$, and the green curves are the cosine approximations $[V(x) = \sin(-\frac{\pi}{2}\frac{x}{l})$ and $I(x) = \cos(\frac{\pi}{2}\frac{x}{l})]$. These profiles show that the end voltage is significant rather than a node due to the terminated inductor.

5.2 Design of TKC

A tunable nonlinear resonant circuit is built by embedding a SQUID array into a microwave resonator, as discussed in Sec. 3.2.2. The Kerr nonlinearity of this SQUID resonator can be calculated by using Eq. 3.34. Moreover, because the critical current of each SQUID is a function of the magnetic flux threading through its SQUID loop [Eq. (3.11)], the effective inductance, and hence the resonance frequency, can be tuned by applying an external magnetic flux.

We design the SQUID array to achieve a resonant circuit with high dynamic range. Generally, we would like to increase the critical current of the SQUIDs in order to amplify larger signals, while maintaining the validity of the expansion used in the analysis of the nonlinear circuit. However, as discussed in Sec. 3.1.2, the critical current can not be so large that the SQUIDs enter the region of trapped flux $I_c > \Phi_0/\pi L_g$. Practically, the geometrical inductance L_g is limited by the smallest features that can be fabricated using optical lithography and planar circuits. We can not build a resonant circuit with a single such SQUID. The inductive impedance of the SQUID at our operating frequency would be much less than the smallest capacitive impedance that we could make using an interdigital finger capacitor. Consequently we use a series array of SQUIDs to increase the inductive impedance. By using an array rather than a single SQUID we also decrease the Kerr constant and therefore increase the pump power required to operate the JPA. This increased pump power improves the dynamic range of the JPA because an amplified signal will be a proportionally smaller fraction of the pump power.

A microscope image of the SQUID array is shown in Fig. 5.5(d). It consists of 20 SQUIDs in series. The expected critical current I_c of the Josephson junction in each SQUID is 6 μA. Thus the SQUID array is expected to have an effective inductance of $L_s \approx 0.6$ nH when the external flux is zero. The geometry inductance of the array is $L_g \approx 0.3$ nH from the simulation. The total inductance is then $L_T = L_g + L_s \approx 0.9$ nH.

With these considerations in mind, I describe the two types of TKCs: a transmission line resonator and a lumped-element circuit. I also designed the on-chip flux bias lines that allow us to

inject DC current for applying the magnetic flux to the SQUID loops.

5.2.1 Design of the distributed TKCs

The first TKC design I present is a distributed microwave resonator. A microscope image of the this TKC is shown in Fig. 5.5. It is composed of a CPW transmission line connected to ground through a SQUID array [Fig. 5.5(d)] at one end and coupled to the CPW feedline through an interdigitated capacitor [Fig. 5.5(b)] at the other end. The length of the line is chosen such that the resonance frequency $\omega_1 \approx 6.5$ GHz with zero flux bias. One feature of the design is that the width of the center conductor of the CPW transmission line is not uniform [Fig. 5.5(c)]. It is designed that the impedances are 50 Ω, 65 Ω, and 50 Ω along the transmission line. The impedance mismatch of the middle section makes the next resonance $\omega_2 \neq 3\omega_1$ to avoid energy coupling to a higher resonance mode that causes loss.

The designed resonator is extremely overcoupled; the intrinsic loss is negligible compared to the coupling energy. Generally, the intrinsic loss of the resonator includes radiative loss, resistive loss, and dielectric loss. The radiative loss for this type of cavity has been shown to yield $Q_{\text{int}} \approx 10^6$ in Ref. [124]. The resistive loss should be negligible because the resonator is made of superconducting niobium metal. To reduce the dielectric loss, we use a high-resistivity silicon wafer (resistivity > 17 kΩ·cm) as a substrate material. However, the major source of dielectric loss is the silicon dioxide isolation layer used in the Josephson junction structure. For the current design, because the number of SQUIDs are greatly reduced by only placing them at the grounded end of the resonator, we expect the dielectric loss should be much less than the previous metamaterial version of the TKC [125].

Although the number of SQUIDs is much less in this design, we can still have high parametric gain. The maximum of the current density is at the grounded end of the resonator, as shown in Fig. 5.4(b). In contrast to the design having SQUIDs distributed all over the center conductor, we only remove the SQUIDs that contribute little to the parametric gain.

For designing the amount of nonlinearity within the TKC, a useful figure is the participation

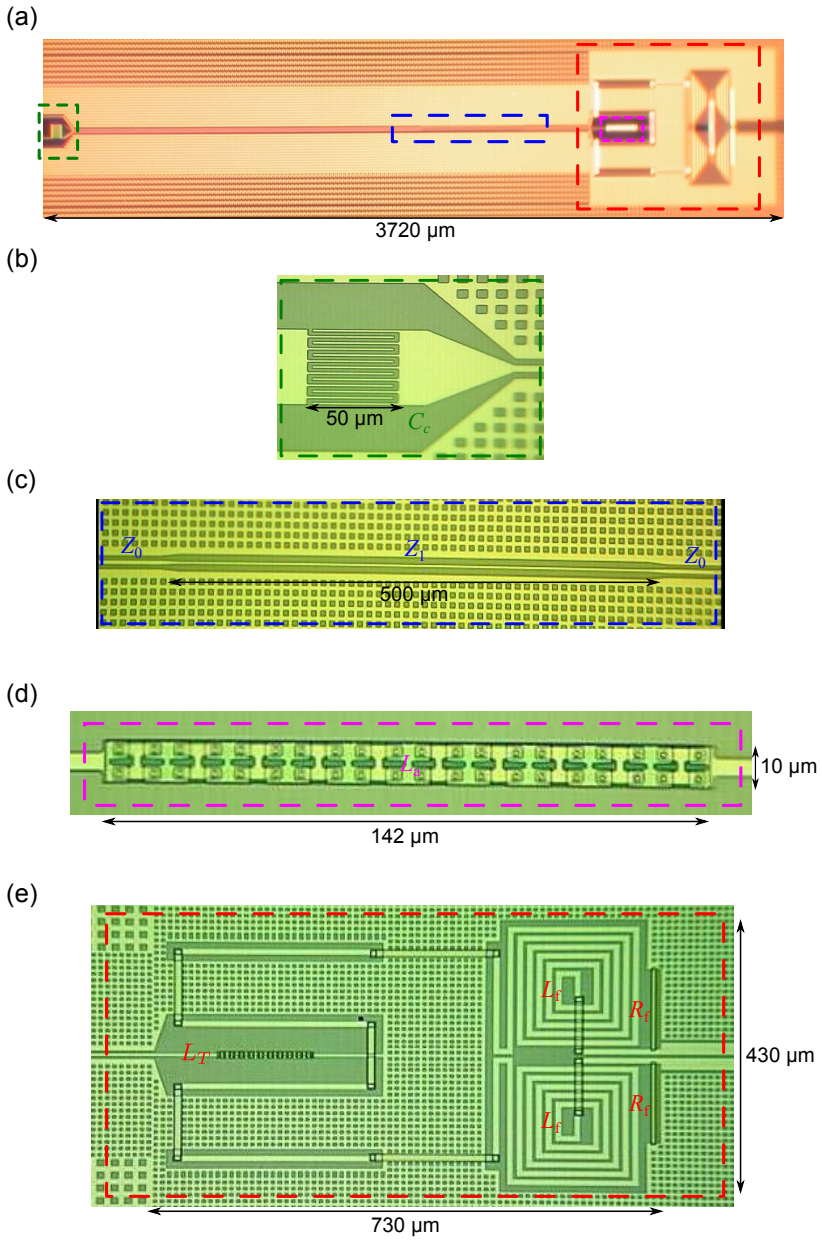

Figure 5.5: Images of the distributed TKC. (a) A microscope image of the distributed TKC. Various features are zoomed-in in (b)–(e). (b) The interdigitated capacitor serves as the coupling capacitor of the resonator with designed value $C_c = 30$ fF. (c) A section of CPW transmission line with impedance $Z_1 = 65\ \omega$ is inserted in the resonator to avoid coupling to the next higher resonance mode. (d) The SQUID array embedded in the resonator provides the tunability of resonance frequency and the nonlinearity for parametric gain. (e) The DC flux bias line. It is symmetric around the SQUID array. The inline filter is composed of two spiral inductors with $L_f = 3.8$ nH and two shunt resistors with $R_f = 100\ \Omega$. The mutual inductance between the flux line and each SQUID loop is $M = 4$ pH, and the effective capacitance between the flux line and the SQUID array is $C_{\text{eff}} = 9$ fF. The ground planes are meshed with square holes for immobilizing the potential trapped flux near the SQUID array to suppress the flux noise.

ratio p [126] defined as

$$p = \frac{E_s}{E_s + E_g}, \tag{5.35}$$

where E_s is the inductive energy stored in the effective inductance of the SQUID array, and E_g is the stored energy in the geometrical inductance. For our transmission line TKCs, the participation ratio can be calculated as

$$p = \frac{E_s}{E_s + E_g} = \frac{\frac{1}{2}L_s I(0)^2}{\frac{1}{2}L_s I(0)^2 + (\frac{1}{2}\int_{-l}^{0} LI(x)^2\,\mathrm{d}x + \frac{1}{2}L_g I(0)^2)}, \tag{5.36}$$

where I use Eq. (5.33) for the integration term. The participation ratio of the distributed TKC is designed to be $p \approx 30\%$. With the coupling quality factor $Q \approx 200$, we fulfill the requirement $pQ \gg 1$ [125], which makes I/I_c a small parameter and validates the expansion of the nonlinear inductance Eq. (3.32).

5.2.2 Design of the lumped TKCs

The second TKC we made is a lumped-element resonant circuit. The physical sizes of basic circuit elements, such as capacitors and inductors, can be fabricated as a small fraction of the wavlength. Typically, the dimensions of these passive elements can be only as few tens of micrometers, which is approximately a few thousandths of the wavelength.

For future applications requiring JPAs with wider operating bandwidth, in addition to the usual coupling $Q \approx 200$ TKC, we also design another TKC with $Q \approx 50$. The microscope images of these two lumped TKCs are shown in Fig. 5.6. They are simply parallel LC circuits, where a significant amount of the inductance is provided by the SQUID array. The participation ratio for the lumped TKC can be straightforwardly calculated by the ratio of the SQUID array inductance L_s to the total inductance $L_T = L_s + L_g$ as

$$p = \frac{E_s}{E_s + E_g} = \frac{L_s}{L_s + L_g}. \tag{5.37}$$

For the $Q \approx 200$ TKC, we keep the pQ product the same as the distributed TKC. Thus, its participation ratio is $p \approx 30\%$. For the $Q \approx 200$, the participation ratio is increased to $p \approx 60\%$.

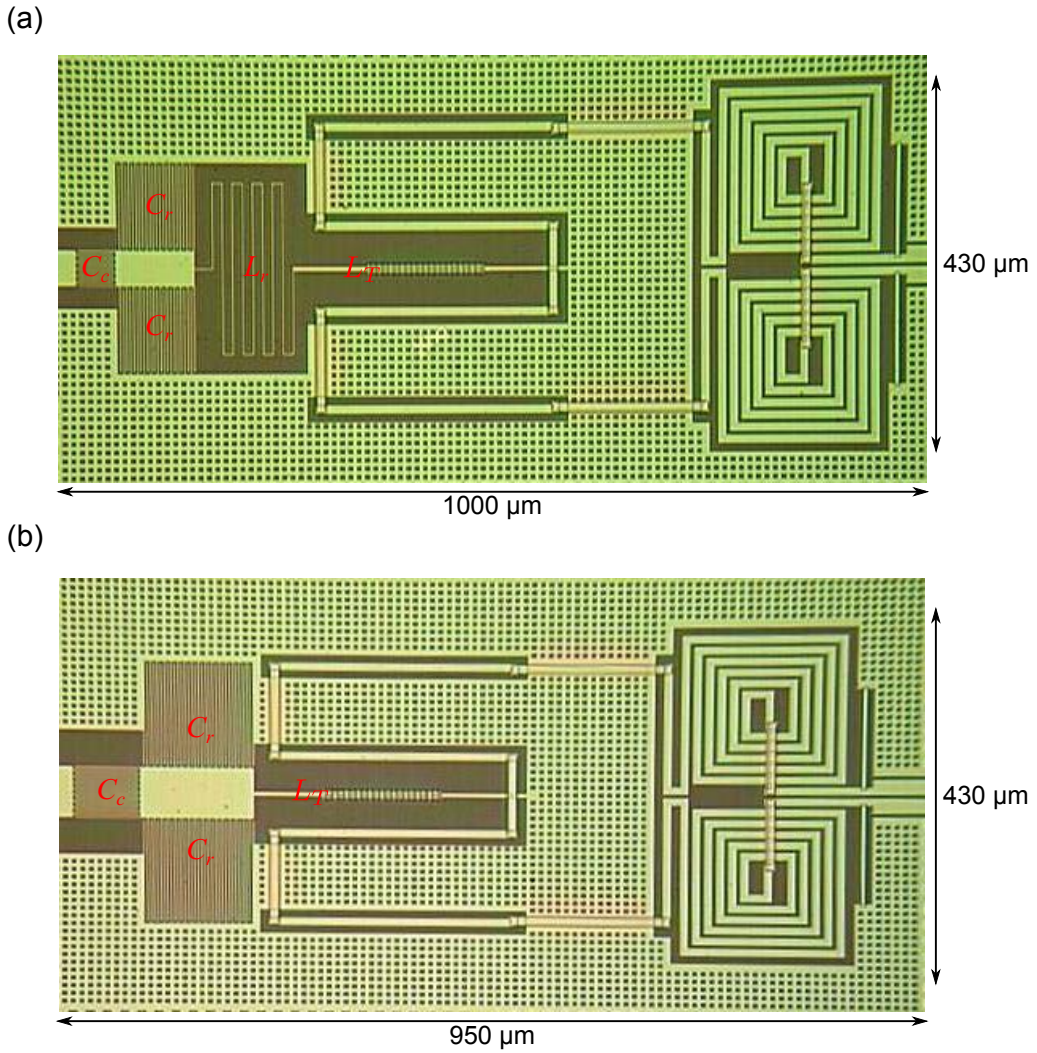

Figure 5.6: Images of the lumped TKCs. (a) The high Q ($Q \approx 200$) version of TKCs. The circuit parameters are: $C_c = 24$ fF, $C_r = 0.24$ pF, $L_r = 1$ nH, and $L_T = L_s + L_g = 0.6 + 0.4 = 1$ nH, where L_s and L_g are the effective inductance and the geometrical inductance of the SQUID array, respectively. The participation ratio is then $p = 30\%$. (b) The low Q ($Q \approx 50$) version of TKCs. The circuit parameters are: $C_c = 75$ fF, $C_r = 0.47$ fF, and $p \approx 60\%$. Both the SQUID arrays and the flux bias lines are the same design as in the distributed TKC.

Both the distributed and lumped TKC devices are fabricated at NIST Boulder using a standard Nb/AlOx/Nb trilayer process [122] modified by eliminating the shunt resistor layer and minimizing deposited oxides [127].

5.2.3 Design of the on-chip flux bias line

Because the TKCs utilize a resonant cavity to enhance the nonlinearity process for parametric gain, our JPAs operate only in a relatively narrow band around the resonance frequency of the TKC. To improve the usefulness of JPAs, we exploit the magnetic-flux-dependent inductance of the SQUID array. By applying magnetic flux to the SQUID array, we can tune the value of the SQUID inductance and therefore the resonance frequency of the TKC. In our previous demonstrations of operating JPAs, we use a superconducting magnetic coil to supply the magnetic flux. One advantage of using a coil is that its large self inductance suppresses the high-frequency current noise, thus enabling a stable resonance of the TKC. However, because of the physical size of the coil, it is difficult to independently tune two TKCs close to each other. For the two-mode entanglement experiment, we want to operate two JPAs integrated onto a single chip, which motivated us to develop the technique of on-chip flux biasing to locally tune each TKC.

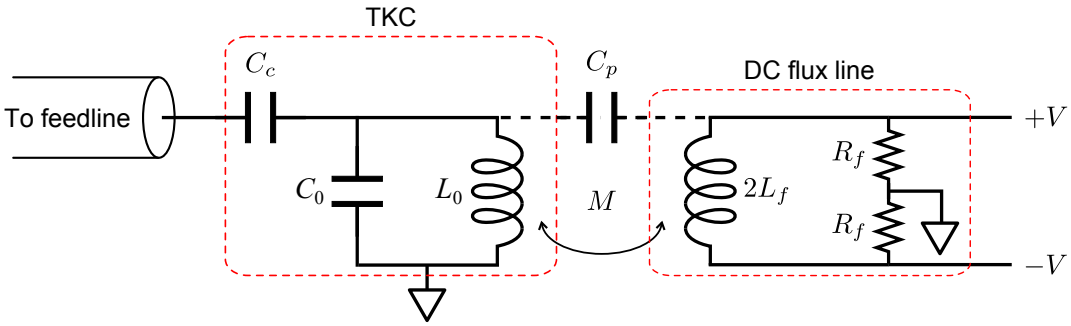

Figure 5.7: Circuit model of the on-chip flux bias line. The DC flux bias line is designed to have a mutual inductance $M = 4$ pH to the SQUID array. The inline LR filter, which has $L_f = 4$ nH and $R_f = 100\ \Omega$, is to filter the high frequency noise. The parasitic capacitance is $C_p \approx 8$ fH from the simulation.

The on-chip DC flux-bias line is essentially a thin metal trace winding around the SQUID

array [Fig 5.5(e) and Fig. 5.6]. The mutual inductance between the flux bias line and the SQUID loop is designed to be $M \approx 4$ pH in simulations. Hence, it needs a 0.5 mA DC current to apply one flux quanta. In addition, the flux line has an inline LR filter consisting of two spiral inductors ($L_f = 4$ nH) and two shunt resistors ($R_f = 100\ \Omega$) to filter out the high-frequency noise of the incoming current with a cutoff frequency 2 GHz (Fig. 5.7).

Although the purpose of the flux line is to couple magnetic flux into the SQUID loops, it also becomes a lossy port of the resonator. There are two possible mechanisms for the resonator energy leaking out to the flux line: the inductive and capacitive coupling. For the inductive loss, the microwave current flowing through the SQUID array can induce current on the flux line, thereby causing energy loss. To suppress this energy loss effect, the physical layout of the flux line is designed to be symmetric around the SQUID array such that the induced current on either side of the SQUID array flows in opposite directions on the flux line. Hence, they cancel out each other [Fig 5.5(e) and Fig. 5.6].

The microwave voltage at the SQUID array can drive a current through the parasitic capacitance between the metal trace of the SQUID array and the flux line (Fig. 5.7). As shown in Fig. 5.4(b), the voltage at the SQUID array is significant and thus can cause energy to leak into the flux line. Thus, I design the flux line via microwave simulations to ensure that, while having enough mutual inductance, the coupling rate through the parasitic capacitor is much smaller than the input/output coupling of the TKC. Moreover, the current driven by the end voltage is dissipated by the shunt resistors of the inline filter. Thus we prefer to have a small shunt resistor to reduce dissipation. However, a smaller resistor generates a larger thermal-noise current spectral density on the flux line, which causes the resonance frequency of the TKC to fluctuate. The designed shunt resistance is a compromise between these two considerations.

In an oversight, the design of the DC flux bias line for the lumped TKCs was naively copied from a design for distributed TKCs. Without carefully considering that the voltage at the SQUID array is actually much larger than that of the distributed TKCs, the energy dissipation on the flux line due to the capacitive loss could be larger for lumped TKCs.

Chapter 6

Quantum state tomography of an itinerant squeezed microwave field

A Josephson parametric amplifier (JPA) is capable of performing a single-mode squeezing operation. We operate a JPA to squeeze one quadrature variance of its input state at the expense of amplifying the orthogonal quadrature. This squeezing operation is a deterministic and reversible transformation. Thus, the JPA adds no noise during this process. Consequently, we can not only prepare squeezed states from the JPA, but also perform efficient quadrature measurements with the JPA as a noiseless preamplifier.

I present a quantum tomography experiment of microwave squeezed states in this chapter. In this experiment, the JPA plays two roles for us. We first use a JPA called squeezer (SQ) to generate a squeezed state. The squeezed state is then measured by a chain of microwave amplifiers in which a second JPA called a verifier (VER) is used as the preamplifier of the quadrature measurement. The measured quadrature is chosen by controlling the relative pump phases between the SQ and VER. With a complete set of quadrature measurements, we are able to reconstruct the Wigner function of the squeezed state using mathematical tools.

I begin the discussion by presenting our experimental implementation of quantum tomography using two JPAs in series. Next, I explain how we calibrate the input variances and the losses of various stages of the amplifier chain. Finally, I present the results of measured quadrature variances and the reconstructed Wigner function of the squeezed states. Most of the text here is from our published paper and its supplement [89].

6.1 Methods of the experiments

In this section, I explain the method of squeezed state tomography. I start with the experimental model that involves using two JPAs in series. Following that I describe the operations of the experiment in detail. Finally, I explain how the measured quadrature variances are related to the Wigner function of the measured state.

6.1.1 Principle of the experiment

To perform a reconstruction of the Wigner function of a microwave squeezed state, we operate two JPAs in series, as shown in Fig. 6.1. The first JPA, operated as the SQ, prepares a squeezed state. The quadrature distribution $W(\theta)$ of the squeezed state is then measured with an efficient quadrature measurement (QM) apparatus. The QM employs a second JPA (VER) to noiselessly amplify one quadrature of the squeezed state, where the amplified quadrature is determined by the phase difference θ between the pumps of the SQ and the VER.

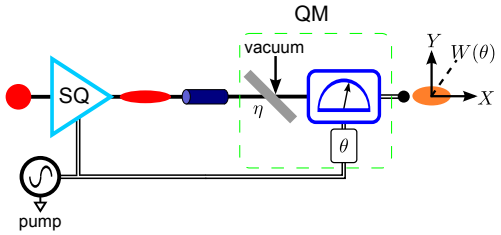

Figure 6.1: Model of the squeezed state tomography experiment. The squeezer (SQ, in blue) prepares a squeezed state whose quadrature distribution $W(\theta)$ is measured with a quadrature measurement (QM) apparatus for quadrature phase θ, where θ is chosen by its pump phase. We model the loss and added noise of the QM with an overall quantum efficiency η.

The QM efficiency is modeled with the insertion of a fictitious beam splitter of power transmissivity η. This efficiency can be related to the added noise of the QM via the relation [128]

$$\eta = \frac{1}{1+2A_n}, \tag{6.1}$$

where A_n is the added noise in units of quanta. Theoretically, the QM efficiency η when using phase-insensitive amplifiers is limited to 50% because of the unavoidable half-quanta of added noise. In

practice, state of the art microwave amplifiers, e.g., high-electron-mobility transistors (HEMTs), have A_n ≈10–20, resulting in $\eta \approx 2\%$. However, as demonstrated in [64], inserting a JPA used as a single-quadrature preamplifier before the HEMT increases the experimentally achieved η by a factor of approximately 20.

Our implementation of a JPA, as shown in Fig. 6.2, requires three elements: (i) a tunable Kerr circuit (TKC),[1] (ii) a directional coupler, and (iii) a circulator. As described in Ch. 5, the TKC is a nonlinear resonator whose nonlinearity originates from a SQUID array. When the TKC is pumped, it provides the parametric gains for its input modes whose frequencies lie within the bandwidth of the TKC centered on the pump frequency. Such microwave modes incident on the TKC are reflected and exit the resonator with one quadrature amplified and the orthogonal quadrature squeezed, depending on their phase relative to the pump's phase. The directional coupler is used to add the pump tone to the incident signal and remove the pump tone from the reflected signal. Finally, the circulator is used to separate the incident and reflected modes into different transmission lines.

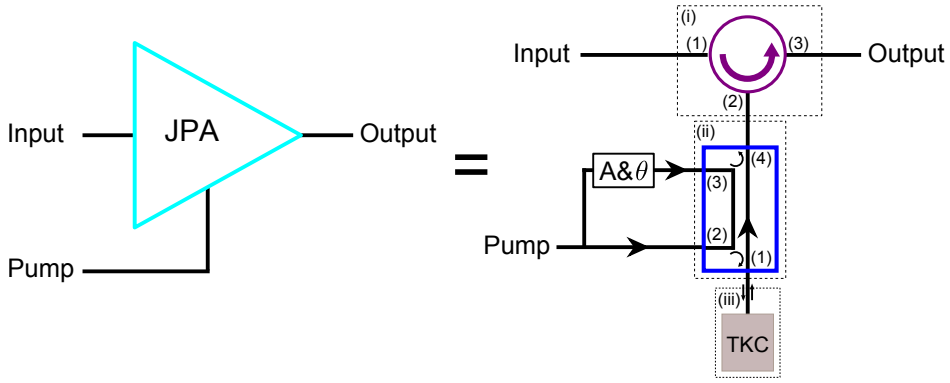

Figure 6.2: Components of a JPA. (a): To implement a JPA, three microwave components are required: (i) a TKC, (ii) a directional coupler and (iii) a circulator. For describing the coupler, I take port (1) of the directional coupler as reference, (2) is the weakly coupled port, (3) the isolated port, and (4) the direct port. Port (2) is used to pump the TKC. Port (3) is used to apply a cancelation tone (adjusted with a room temperature attenuator and phase shifter) that nulls the pump and displaces the output of the JPA back to the origin of the phase space.

[1] The JPA used in the tomography experiment employs the metamaterial version of the TKC previously developed in our group [129, 53, 130].

6.1.2 Implementation and operation of the experiment

The schematic of the experiment is shown in Fig 6.3. The input thermal states for the SQ originate from either of the two 50 Ω terminations thermally anchored to the base stage ($T = 15$ mK) or the 4 K stage of the cryostat. This hot-cold load setup is connected to the SQ via a microwave switch located at the 4 K stage. Although the tomography of the squeezed state is only performed with the cold load, both loads are required to calibrate the efficiencies of the measurement chain.

To squeeze the input states, the SQ is pumped by a microwave signal generator at 7.45 GHz through the weakly coupled port of the directional coupler. The SQ pump frequency is determined by finding the applied magnetic flux from an external superconducting coil that brings both the SQ and the VER into the same resonance frequency.

The output of the SQ is a quadrature squeezed state displaced by its pump. To prevent the saturation of the VER with the SQ pump, we null it by sending a copy of the SQ pump through the isolation port of the SQ's directional coupler to cancel the SQ pump. Then the resultant squeezed state is passing to the VER, which is pumped by the second microwave generator at 100 kHz higher than the SQ pump frequency. With this 100 kHz detuning, the measured quadrature phase θ sweeps from 0 to 2π every 10 μs.

Because of the finite isolation of the circulator (approximately 20–30 dB), there is some leakage of the VER pump into the SQ, modifying the degree of squeezing. To minimize this unwanted effect, we inject a copy of the VER pump through the isolation port of the directional coupler to cancel the VER pump.

Following the VER are the high-electron-mobility transistor (HEMT) amplifier at 4 K and the commercial microwave amplifiers at room temperature that complete the whole amplification chain. Finally, the amplified voltages are mixed down by an I/Q mixer where the LO of the mixer is from the same generator that pumps the VER. Both of the in-phase (I) and quadrature (Q) voltage data are digitized with a 10 MHz sampling rate. With these quadrature measurements, we calculate the variances at all measured quadrature phases and reconstruct the Wigner function of

the squeezed state.

6.1.3 Wigner function reconstruction

By making quadrature measurements with quadrature phases from 0 to 2π, we are able to infer the quantum state of a single mode of a microwave field. Our microwave measurement apparatus measures the value of the quadrature X_θ, where θ is varied by sweeping the phase of the VER pump. The probability density function $\mathrm{pr}(X_\theta)$ for measuring a particular value of X_θ is the marginal density function of the Wigner function, i.e., $\mathrm{pr}(X_\theta) = \int dX_{\theta+\pi/2} W(X_\theta, X_{\theta+\pi/2})$, as shown in Fig. 6.4. Thus, by performing measurements of X_θ on many identical copies of the system and varying θ, the "hidden" quantum object can be seen from different angles, and we can infer its state. Because of the measurement inefficiency, the measured $\mathrm{pr}(X_\theta)$ is no longer the projection of the true Wigner function, but rather a smoother quasi-probability distribution created by convolving the true Wigner function with a Gaussian Wigner function [131]. To deconvolve the effect of inefficiency, we use the maximum-likelihood quantum state tomography [29] with the knowledge of the inefficiencies of the various stages in the measurement chain. In the next section, I explain how we perform the experiment to separately measure the losses and the added noise of the various stages.

6.2 Efficiency calibration

The inefficiency of the measurement chain prevents us from measuring the true projection of the Wigner function. To infer the squeezed state corrected for the inefficiency, we need to isolate the effect of a specific loss or added-noise contribution to the overall efficiency of the measurement chain. In the limit of large HEMT power gain G_H, the overall quantum efficiency η can be cast as

$$\eta = \frac{\alpha}{2 - \alpha + 2A_V + [2A_H - (1-\beta)]/G_V\beta}, \tag{6.2}$$

where A_V (A_H) is the VER (HEMT) added noise, α (β) is the fraction of power transmitted by the microwave circuitry between the SQ and the VER (the VER and the HEMT), and G_V is the

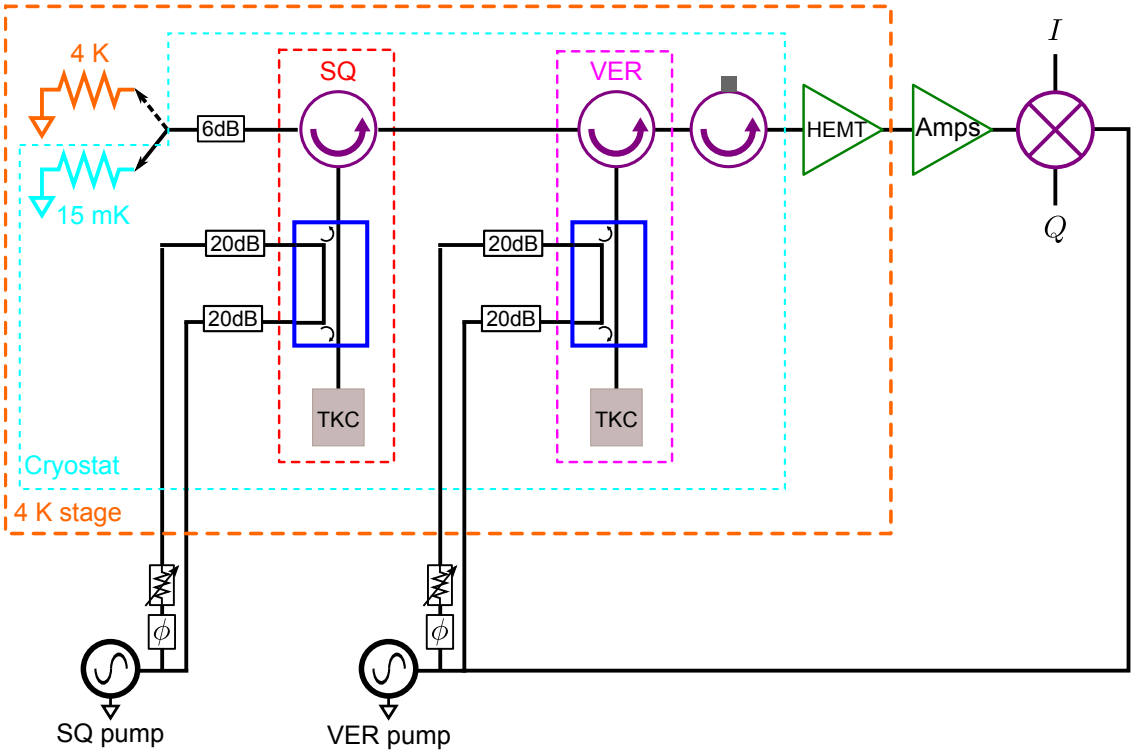

Figure 6.3: Circuit diagram of the squeezed state tomography experiment. The operational details are described in the text.

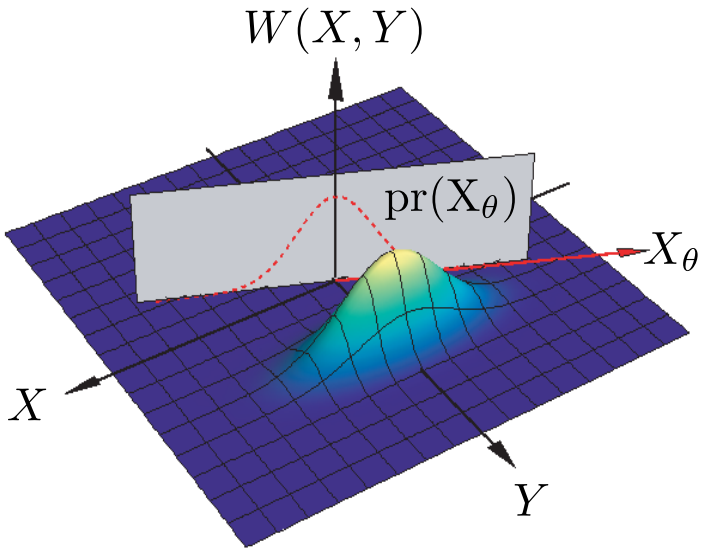

Figure 6.4: Graphical interpretation of the Wigner function reconstruction. The probability distribution $\mathrm{pr}(X_\theta)$ is simply the projection of the Wigner function: $\mathrm{pr}(X_\theta) = \int dX_{\theta+\pi/2} W(X_\theta, X_{\theta+\pi/2})$.

power gain of the VER (Fig. 6.5).

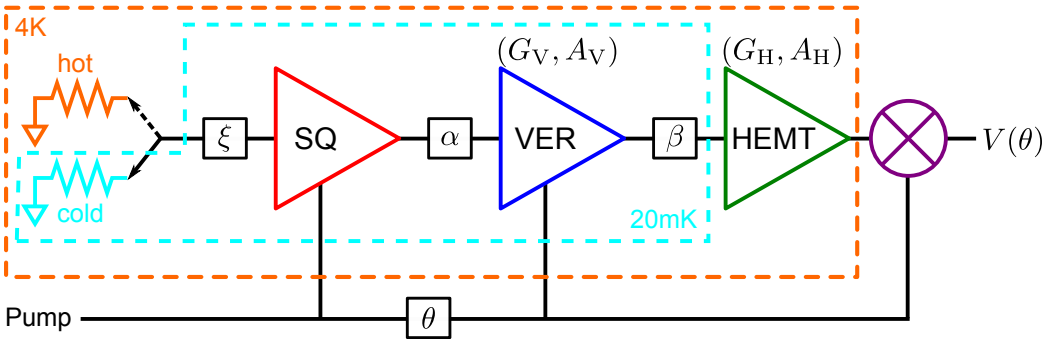

Figure 6.5: Measurement efficiency model of the tomography experiment. In this model, the overall detection efficiency η is decomposed into the power transmissivities before the SQ (ξ), between the SQ and the VER (α), and between the VER and the HEMT (β) and the added noises of the VER (A_V) and the HEMT (A_H). All the microwave components and cables are considered lossless; their imperfections are absorbed into ξ, α, and β.

The crucial aspect that makes our calibration scheme possible is that the TKCs have widely tunable resonance frequencies, adjusted by imposing a magnetic flux [129, 53, 130]. When far from resonance, the TKCs behave as open circuits. They are simply mirrors that reflect the microwave field without otherwise transforming it; therefore, either the SQ or VER or both stages can effectively be bypassed. Briefly, we inject different amounts of thermal noise into the amplifier chain while operating each JPA either as an amplifier (ON) or as a noiseless element with unit gain (OFF). We then infer the added noise and loss of the elements by observing the variation in the noise at the output of the measurement chain.

We begin with both the SQ and VER bypassed (SQ OFF, VER OFF), so that the gain of the SQ is $G_S = 1$, and the gain of the VER is $G_V = 1$. If the switch is lossless, when it is connected to the cold load, the noise power exiting the HEMT amplifier would be $S = G_H(A_H + S_f)$, where $S_f = (1/2) + n_f = (1/2) + [\exp(\hbar\omega/k_B T_f) - 1]^{-1}$, and T_f is the temperature of the cryostat. Notice that the result doesn't depend on the transmissivities α, β, or ξ because these are at the same temperature as the cold load. Consequently each loss component emits as much power as it absorbs. However, with the switch connected to the hot load, the expression for the total power at the output

becomes $S = G_H(A_H+(\xi\alpha\beta)S_h+(1-\xi\alpha\beta)S_f)$, with $S_h = (1/2)+n_h = (1/2)+[\exp(\hbar\omega/k_BT_h)-1]^{-1}$, and $T_h = 4.1$ K. In both cases, we expect and observe that S depends linearly on S_f with an offset. By fitting these linear dependencies, we can extract G_H, A_H, and the product $\xi\alpha\beta$.

However, we cannot assume that the switch is lossless. Because its loss sits at 4.1 K, it always emits noise power $S_h(1-\lambda)+S_{in}\lambda$, where S_{in} is the incident noise from either the cold or hot load, and λ is the switch transmissivity. So, even when $n_f \ll 1/2$, the state presented at the SQ stage will have average thermal occupancy of $\bar{n} = (1-\lambda)\xi n_h$. We write the noise power at the output as a function of S_f for switches in both positions as

$$S_{1c} = G_HA_H + S_hG_H(1-\lambda)\xi\alpha\beta + S_f[G_H\lambda\xi\alpha\beta + G_H(1-\xi\alpha\beta)] = b_{1c} + m_{1c}S_f, \tag{6.3}$$

$$S_{1h} = G_HA_H + S_hG_H(\xi\alpha\beta) + S_f[G_H(1-\xi\alpha\beta)] = b_{1h} + m_{1h}S_f, \tag{6.4}$$

where the subscript $1c$ ($1h$) corresponds to the switch connected to the cold (hot) load. Fitting our noise data to the right hand side of Eq. 6.3 [Fig. 6.6(a)] and 6.4, we can obtain the four parameters b_{1h}, b_{1c}, m_{1h} and m_{1c}. However as these parameters are not independent, i.e., $S_h = (b_{1h} - b_{1c})/(m_{1c} - m_{1h})$, we cannot extract the switch loss independently. We can nevertheless bound this unknown loss by taking a worst case estimate as the manufacturer's minimum-specified transmission (at room temperature) $\lambda = 0.83$ and assuming it is less lossy at 4.1 K. We moreover confirmed that at room temperature, the frequency-dependent loss of the switch is within the manufacturer's specification. Then by using $1 < \lambda < 0.83$, we can bound the desired parameters using Eq. 6.3 and 6.4, with the expressions $(\xi\alpha\beta)^{-1} = 1+m_{1h}S_h\lambda/(b_{1h}-b_{1c})$, $G_H = m_{1h}/(1-\xi\alpha\beta)$, and $A_H = (b1c/G_H) - (1-\lambda)S_h(\xi\alpha\beta)$.

We then perform the same analysis, finding the linear dependence of the output noise on S_f and on the switch position, with the SQ OFF and VER ON. From these fits and knowledge of A_H and G_H, we find $\xi\alpha$, A_V, and$G_V\beta$. Finally, we operate the experiment with SQ ON and VER OFF. A third time we fit the linear dependence of S on S_f with the switch in both positions, determining ξ, α and β separately [Fig. 6.6(b)]. We evaluate the expressions for ξ, α, β, A_V, A_H, and $\bar{n}$ at the bounds on λ, finding $\alpha = 68 \pm 2\%$, $\beta = 74 \pm 5\%$, $A_V = 0.25 \pm 0.06$, $A_H = 17.3 \pm 0.1$,

and $\bar{n} = 0.15 \pm 0.15$. We also find $\xi = -9.9 \pm 1$ dB, of which 6 dB arises from an attenuator that has been placed at the input of the SQ stage. With sufficient VER gain $G_V = 180$, one quadrature of the resulting squeezed state is amplified at the VER stage such that the noise in the amplified quadrature exceeds A_H for any θ. From Eq. 6.2, we obtain an overall quantum efficiency of $\eta = 36 \pm 4\%$, which can be compared to $\eta \approx 2\%$ without the VER stage.

In this experiment, our uncertainty in η and $\bar{n}$ create a systematic source of error. We thus perform our data analysis under three assumptions (1) high efficiency ($\eta = 0.40$) and high mean photon number ($\bar{n} = 0.30$), (2) best estimate for both efficiency ($\eta = 0.36$) and mean photon number ($\bar{n} = 0.15$), and (3) low efficiency ($\eta = 0.33$) and low mean photon number ($\bar{n} = 0$). These three cases give us "pessimistic", "best-guess", and "optimistic" analyses in terms of the purity of the squeezed state estimated by the tomography. Using a lower estimate for η and $\bar{n}$ as inputs to the tomography algorithm causes it to return a more pure, more squeezed, and therefore a more "optimistic" estimate of the squeezed state. Associated with each of these three cases, we also have statistical uncertainty, so the given error bounds cover an interval that includes both uncertainties around the "best-guess" estimate. They are reported in the form X^{+U}_{-L}, where X is the statistical mean using the "best-guess" calibration, and L and U are, respectively, the lower and upper bounds of the one standard deviation uncertainty in the "pessimistic" and "optimistic" cases.

To acquire the above calibration data sets, we regulate the cryostat's temperature at 10 values between base temperature ($T < 50$ mK) and 800 mK, which requires about 7 hours to complete. For each temperature point, we measure the noise at the output under all six conditions, 2 switch positions, and 3 amplifier configurations (SQ OFF VER OFF, SQ OFF VER ON, and SQ ON VER OFF). We inject a tone detuned from the VER pump by 20 kHz. By dividing the noise power at the output of the chain by the power in this tone, we become insensitive to any variation in G_H over the time needed to acquire the data. At the end of the calibration, we immediately operate the experiment with SQ ON and VER ON, to acquire the data in the paper. In addition, we use the tone to ensure that we do not saturate the amplifier chain.

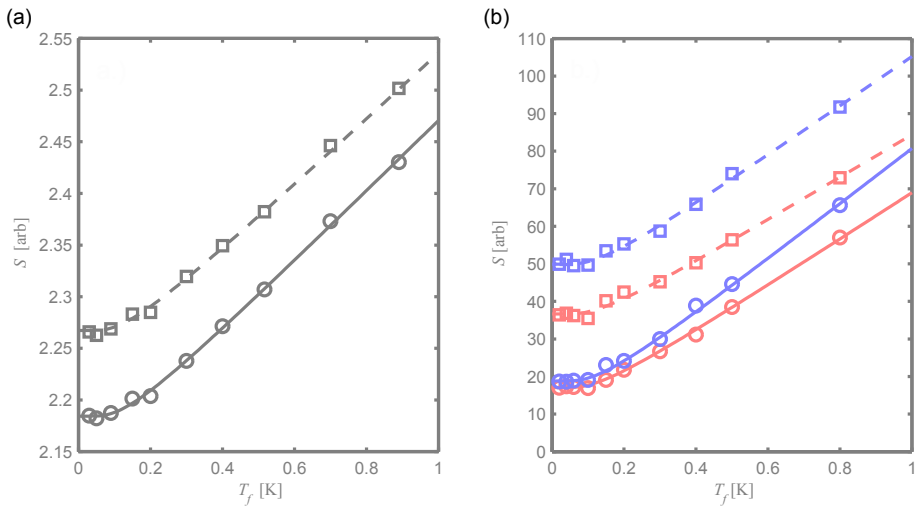

Figure 6.6: Measurement efficiency calibration. The noise density S in arbitrary units at the output of the measurement is plotted versus refrigerator temperature T_f. (a) Data acquired with the VER and SQ OFF and the switch connected to the cold load (circles) and hot load (squares). The lines are *linear* fits to S versus S_f for the case of the switch connected to the cold load (solid) and hot load (dashed). (b) Data acquired with the VER ON and SQ OFF (blue) and VER OFF and SQ ON (red), with the switch connected to the cold load (circles) with a linear fit (solid) and hot load (squares) with a linear fit (dashed). The arbitrary y-scale is consistent between the six plots. The linear fits do not appear as lines because we plot S versus T_f rather than S_f.

6.3 Results

In this section, I present the measured quadrature variances of the generated squeezed states and the Wigner function reconstructed from the variances data by using the maximum likelihood method.

6.3.1 Quadrature variance

At the output of our microwave quadrature measurement chain, the noise voltages are digitized. We can then calculate the variances of the noise voltages at all measured phases. We first insert the weak thermal state with mean photons $\bar{n}$ (by simply bypassing the SQ) and measure voltages proportional to quadrature values at many θ [Fig. 6.7(a)] to calibrate the QM, converting the measured voltage noise into units of noise quanta. As expected, this voltage noise is θ independent, with a variance of $\Delta V^2_{\mathrm{SQ,OFF}} = 3.2 \times 10^{-5}$ mV^2. Under the convention that vacuum has quadrature variance 1/2 in units of "quanta", we calibrate this voltage variance to be $\Delta X^2_{\mathrm{SQ,OFF}} = (1-\eta)/2 + \eta(1/2+\bar{n}) = 0.55^{+0.07}_{-0.05}$ quanta. Therefore, the desired conversion factor $\Delta X^2_{\mathrm{SQ,OFF}}/\Delta V^2_{\mathrm{SQ,OFF}} = 1.71^{+0.20}_{-0.17} \times 10^4$ quanta/mV^{-2} is used to rescale the variances in Fig. 6.7 (c).

For the case in which the SQ is pumped, we observe the characteristic phase-dependent noise for a squeezed state. Compared to the measurements when the SQ is bypassed, we observe the noise level is below that of the unsqueezed input state. At the phase for which the noise is minimum, the histogram of quadrature measurements is shown in Fig. 6.7(b). The SQ-bypassed histogram is clearly wider than the squeezed state histogram, demonstrating our ability to observe squeezing directly at the output of our measurement chain without correcting for the measurement inefficiency. Moreover, I plot the variances of the quadrature measurements expressed in units of quanta, clearly showing squeezing below the vacuum level. Without correcting for the measurement efficiency η, we observe a minimum quadrature variance that is $\Delta X^2_{\mathrm{SQ,MIN}} = 68^{+9}_{-7}\%$ of the variance of the vacuum.

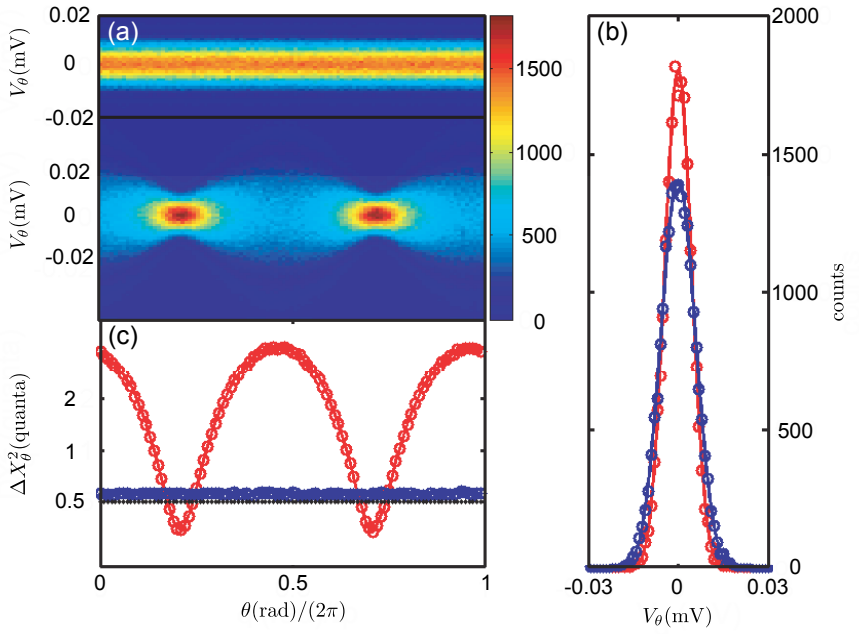

Figure 6.7: Measured quadrature variances. (a) Density plot of the number of occurrences in a 1 μV bin size of the amplified quadrature voltage V_θ versus $\theta/2\pi$, with the SQ pump OFF (top) and ON (bottom). (b) Histograms of V_θ at the maximum of squeezing: data ($\circ$) and Gaussian fit (continuous lines) for the SQ pump OFF (blue) and ON (red). (c) Noise variance ΔX^2_θ in quanta units on a log scale versus $\theta/2\pi$ for the SQ pump ON (red) and OFF (blue). The (black) line indicates our estimate of the vacuum noise level under the "best-guess" calibration.

6.3.2 Reconstructed Wigner function

To infer the quantum state created by the squeezer, thus correcting for the inefficiency of the measurement apparatus, we use maximum-likelihood quantum state tomography [132]. For each of the three calibration cases mentioned in the previous section, we perform 35 reconstructions using independent subsets each containing 10,000 quadrature measurements of the total measured data. We estimate statistical uncertainty from the spread of properties (such as fidelity or minimum variance) of the set of 35 reconstructions. The statistical uncertainty is significantly lower than the systematic uncertainty.

I show the Wigner function of the "best-guess" reconstructed state ρ in Fig. 6.8. The *pure* squeezed vacuum state $|\psi\rangle$ that has the highest fidelity with ρ has the minimum quadrature variance $6.0^{+1.4}_{-1.1}\%$ [2] of the vacuum variance. The maximum fidelity is $F = \langle\psi|\rho|\psi\rangle = 0.81^{+0.16}_{-0.17}$. Because the minimum variance of ρ is biased by an amount comparable to our systematic uncertainty as discussed below, we infer the minimum variance $\Delta x^2_{\mathrm{SQ,MIN}}$ directly from the observed minimum variance as $\Delta x^2_{\mathrm{SQ,MIN}} = (1/\eta)(\Delta X^2_{\mathrm{SQ,MIN}} - (1-\eta)/2)$. We find $\Delta x^2_{\mathrm{SQ,MIN}} = 12^{+30}_{-12}\%$ of the vacuum variance.

To provide more discussion on the quadrature variances estimated from different quantities, we summarize our estimates of inferred parameters characterizing the squeezed state for the three analysis cases. The estimates are based upon our systematic calibration uncertainties shown in Table 6.1. The first line presents the fidelity $F = \langle\psi|\rho|\psi\rangle$, where ρ is the maximum-likelihood reconstructed density matrix of the field exiting the SQ, and $|\psi\rangle$ is the pure vacuum-squeezed state that maximizes the fidelity. The second line gives the ratio of the minimum variance of $|\psi\rangle$ to the variance of the vacuum. The third line gives the purity $\mathrm{Tr}(\rho^2)$ of ρ. The fourth and fifth lines give the ratios of the squeezed and antisqueezed variances of the reconstructed state to the variance of the vacuum. The last line gives our estimate of the experimental states' minimum variance based

[2] The estimates of the squeezed state's properties are reported in the form X^{+U}_{-L}, where X is the mean of the 35 maximum-likelihood estimates based on the "best-guess" calibration parameters. L and U are the lower and upper bounds of the one standard deviation uncertainty interval associated with our maximum-likelihood estimate based on the "pessimistic" and "optimistic" cases.

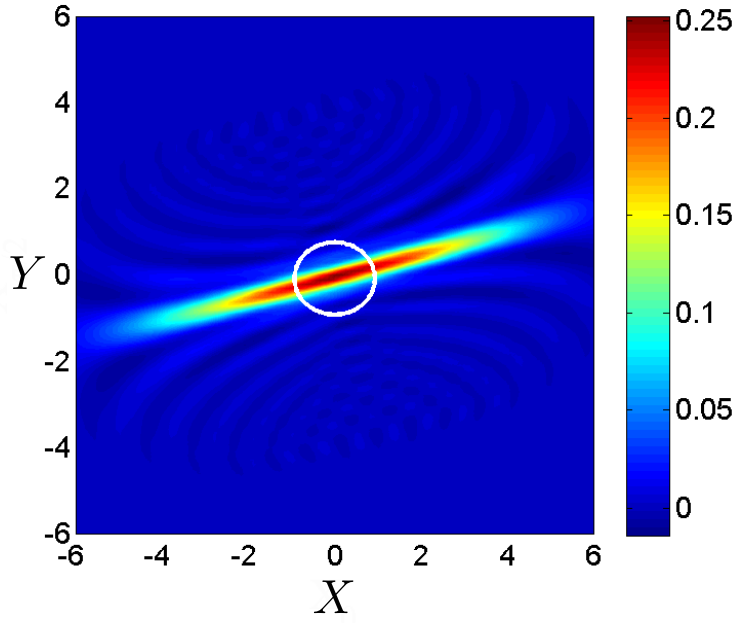

Figure 6.8: The reconstructed Wigner function. Mean of 35 reconstructions of the Wigner function of the state exiting the SQ, inferred by maximum likelihood under the "best-guess" assumption. The faint pattern of ripples extending from the origin is caused by truncation at 30 photons of the density matrix used to represent the state. The white circle at the origin shows the full-width at half-maximum of the vacuum state.

Table 6.1: Inferred properties of the squeezed state, based upon our three analysis assumptions.

	Pessimistic	Best guess	Optimistic
Fidelity	0.66 ± 0.02	0.807 ± 0.016	0.960 ± 0.005
Min. var. of comparison pure state $\|\psi\rangle$:[a]	0.065 ± 0.009	0.060 ± 0.003	0.0493 ± 0.0006
ρ's purity	0.62 ± 0.02	0.74 ± 0.02	0.96 ± 0.01
ρ's sq. var[b].	0.918 ± 0.002	0.484 ± 0.013	0.304 ± 0.008
ρ's anti-sq[b]. var.	25.54 ± 0.07	20.17 ± 0.06	19.18 ± 0.05
Linear sq. var[c].	0.40 ± 0.02	0.12 ± 0.02	-0.18 ± 0.02

[a] Ratio of the variance of the squeezed quadrature of the pure squeezed vacuum state with highest fidelity to the variance of the vacuum.
[b] Ratio of variance of most likely state ρ's squeezed or antisqueezed quadrature to the variance of the vacuum.
[c]Direct linear inference of the squeezed state's minimum variance relative to vacuum variance.

on direct linear inference.

We have three variances that characterize the state created in this experiment: the linear estimate of the experimental state's minimum variance (12%), the most likely state ρ's minimum variance (48%), and the minimum variance of the pure squeezed vacuum state $|\psi\rangle$ that maximizes the fidelity with ρ (6.0%). The discrepancies among them are discussed below.

The quadrature measurements we observe are the linear combination of the quantum state created by the squeezer and vacuum fluctuations:

$$X_\theta = \sqrt{\eta} x_\theta + \sqrt{(1-\eta)} y_\theta,$$

where x_θ is the quadrature of the squeezed state, and y_θ is the quadrature of the vacuum state. Solving for x_θ gives

$$x_\theta = \frac{1}{\sqrt{\eta}} \left(X_\theta - \sqrt{(1-\eta)} y_\theta \right).$$

Therefore the inferred variance of the squeezed state's quadrature Δx_θ^2 is

$$\Delta x_\theta^2 = \frac{1}{\eta} \left[\Delta X_\theta^2 - (1-\eta)\, \Delta y_\theta^2 \right].$$

The vacuum variance $\Delta y_\theta^2 = 1/2$, and we can easily calculate an unbiased estimate of ΔX_θ^2 for every phase θ. This gives us an unbiased estimate of Δx_θ^2 that does not depend on the details (for example, Gaussianity) of the quantum state. We calculate Δx_θ^2 using 20,000 quadrature measurements at

each of 100 evenly spaced θ and calculate the minimum value $\Delta x^2_{\mathrm{SQ,MIN}}$, as shown in Table 6.1. The statistical uncertainties show one standard deviation in the estimate of $\Delta x^2_{\mathrm{SQ,MIN}}$. For the "optimistic case", we calculate a negative variance, which is clearly unphysical. This is a sign of inconsistency in the "optimistic" calibration parameters. Because the "optimistic" estimate for the squeezed state is computed using the lower bounds on η and $\overline{n}$, this negative variance is evidence that the detector's true η and/or effective gain ($\Delta X^2_{\mathrm{SQ,OFF}}/\Delta V^2_{\mathrm{SQ,OFF}}$) must be larger than the lower bounds set by calibration.

The minimum variance of ρ is significantly higher than this linear estimate. This deviation is caused by bias in the maximum-likelihood method. Quantum state estimation by maximum likelihood is biased toward more mixed states, and the amount of bias increases with increasing purity of the state from which the measurements are drawn [133]. Based on numerical experiments, the bias in our estimates of the fidelity should be well below the uncertainty level set by systematic effects. However, the bias in our estimates of the minimum variance of the inferred state could be larger. To attempt to quantify this effect, we simulate measuring and performing maximum likelihood tomography on a Gaussian state. This Gaussian state is chosen to have minimum and maximum variances equal to those calculated by the linear method described above for the "best-guess" case. By computer, we simulate 10,000 quadrature measurements (the same number we use for the maximum-likelihood analysis of the true experiment) from this Gaussian state and perform maximum-likelihood tomography on those measurements. The inferred state has a minimum variance of 40%. Therefore it is possible that the experimental state has a smaller minimum variance than the most likely state inferred from only 10,000 measurements. Because we have some independent evidence for non-Gaussian effects in the experiment, we cannot quantify this size of this bias using this Gaussian simulation. Other numerical simulations have confirmed that this bias decreases as the number of measurements analyzed increases and that this bias is not caused by truncation of the Hilbert space at 30 photons.

The apparent discrepancy between the 6% for the variance of $|\psi\rangle$ and the 48% for the variance of ρ also deserves some comment. Note that one would not expect the minimum variance of a mixed

state to equal the minimum variance of its highest-fidelity pure state. The fidelity between a mixed Gaussian state (centered at the origin of phase space) whose minimum and maximum variances are v_x and v_p and a pure squeezed vacuum state with minimum variance v_s is given by

$$F_{\text{Gauss}} = \frac{2}{\sqrt{\frac{(1+4v_s v_p)(v_s+v_x)}{v_s}}}.$$

The highest-fidelity pure state has a minimum variance of $v_s = \frac{1}{2}\sqrt{\frac{v_x}{v_p}}$, and the fidelity between these two states is

$$F_{\text{Gauss,max}} = \frac{2}{1+2\sqrt{v_x v_p}}.$$

Consider the state σ to be a Gaussian state with a minimum variance of 48% and maximum variance of 2017%. (σ has variances equal to those of our state ρ, but unlike ρ, σ is guaranteed to be Gaussian.) Then let $|\psi\rangle$ be the pure squeezed vacuum state that has maximum fidelity with σ. $F_{\text{Gauss,max}}\langle\psi|\sigma|\psi\rangle = 0.49$, and the minimum variance of $|\psi\rangle$ is 7.7%. The difference between the minimum variances of ρ and $|\psi\rangle$ is to be expected. However, the maximum fidelity of ρ is significantly larger than we would expect if it were perfectly Gaussian. This non-Gaussianity could be caused by bias in the maximum-likelihood inference and/or genuine non-Gaussian effects in the experiment.

Tomographic reconstruction of a quantum state requires that the experimental device always creates the same (potentially mixed) quantum state, that the measurements are well described by inefficient quadrature measurements, and that the calibration of those measurements is consistent. In this experiment, we have observed some evidence that at least one of these assumptions is violated. The likelihood of the maximum-likelihood state is significantly lower than one should expect from simulated measurements on that state. That is, if the tomographic assumptions above were true, we expect to find a significantly higher value for the maximum likelihood. We believe this effect could be caused by an interaction between the state preparation and measurement stages of the experiment, one possibility is a phase-dependent efficiency of the measurement JPA, and/or nonlinear processes in the measurement.

In conclusion, we reconstruct the Wigner function of an itinerant squeezed microwave field generated at the output of a JPA. Using a second JPA as a preamplifier increases the quantum efficiency of quadrature measurement from approximately 2% to 36%. The level of squeezing is primarily limited by noise added to the squeezed state generated by the JPA. We use the maximum likelihood quantum state tomography to deconvolve the QM inefficiency in order to precisely characterize the state generated. This is an important step toward generating distributable microwave entanglement on chip.

Chapter 7

Generating and verifying entangled-itinerant microwave fields

For the past several decades, researchers have been making significant progress on quantum information technology with superconducting circuits, which carry quantized microwave photons. The superconducting circuits are attractive because they can be lithographically patterned and fabricated as small chips. To fully exploit the power of superconducting circuits, generating on-chip, distributable microwave entanglement has been a vital research subject. In addition, a high-quality detection scheme to measure the microwave entangled states is as important as the generation of entanglement. In this chapter, I present my work on generating a two-mode entanglement of the itinerant microwave fields and verifying the entangled states with an efficient joint measurement.

I have already shown in Ch. 2 that, in principle, a state arbitrarily close to a maximally entangled state can be generated by combining two pure, arbitrarily squeezed states on a 50:50 beam splitter. However, to reduce the experimental complexity, we combine only one moderately squeezed state with vacuum on a quadrature hybrid. The two output modes of the hybrid are then measured with a two-channel measurement apparatus consisting of two single-quadrature amplification chains, where each chain employs a Josephson parametric amplifier (JPA) as its preamplifier. This measurement scheme allows us to perform efficient joint quadrature measurements on the two-mode state. Moreover, the measured quadrature phases of the two modes can be independently controlled which enables us to fully characterize the two-mode state.

I begin the discussion in this chapter with presenting the model of the experiment and explaining how we implement the entanglement generation and verification in the microwave regime.

Next, I explain the calibrations of input variances of the experiment and possible amplifier-gain variations to express the measured quadrature variances in units of the vacuum. Finally, I present the results of measured variances and the associated covariance matrix of the two-mode states. By showing that the resultant covariance matrix satisfies the entanglement criterions Eq. 2.87 and 2.89, I demonstrate the achievement of two-mode entanglement.

7.1 Implementing generation and verification of two-mode entangled states with JPAs

In this section, I present the experimental setup for generating and verifying two-mode entanglement. First, I introduce a single-squeezer model (SSM) of the experiment that I use to explain the data of quadrature measurements and discuss how the covariance matrix Eq. (2.44) is calculated from the model parameters. Following that, I present two important superconducting chips we build for the experiment: the entangler chip and the lumped-element tunable Kerr circuit (TKC). The entangler integrates JPAs with passive microwave components to generate two-mode entangled states; the lumped TKC is the circuit we use to build the JPA for verifying the entangled states. Finally, I explain the operational details of the entanglement experiment.

7.1.1 Single-squeezer model of the experiment

The entanglement between two spatially separate itinerant microwave modes is generated by combining a quadrature-squeezed state and a vacuum state on a microwave hybrid. As illustrated in Fig. 7.1, the squeezed state is generated by operating a JPA denoted as a squeezer (SQ), with a squeezing parameter s. The quadrature hybrid (HY) is characterized by its power transmission coefficient t and power-coupling coefficient $c = 1 - t$. I detect the correlations between the two output modes by simultaneously making quadrature measurements on the two output modes. The detection apparatus consisting of two single-quadrature measurement chains (QM1 and QM2), where each chain employs a JPA called a verifier (VER) as its preamplifier. The outcomes of the measurements are denoted as $W_1(\theta_1) = X_1\cos(\theta_1)+Y_1\sin(\theta_1)$ and $W_2(\theta_2) = X_2\cos(\theta_2)+Y_2\sin(\theta_2)$,

where θ_1 and θ_2 are the quadrature phases of the two modes, respectively. I model all losses and the inefficiencies of the two measurement chains by introducing two fictitious beam splitters with power transmission coefficients η_1 and η_2, respectively. One important feature of our measurement scheme is that the two measurement chains can each choose their noiselessly measured quadrature by independently adjusting their reference phase θ_1 and θ_2 over all pairs (θ_1, θ_2). By making repeated measurements on many copies of the same two-mode state and adjusting their phase references over all possible values, I can fully characterize the two-mode state.

As discussed in Ch. 2, a Gaussian two-mode state is fully characterized by its covariance matrix Σ. To compute the covariance matrix predicted by the single-squeezer model I examine the effects of each of the linear optical transformations (including squeezing) shown in Fig. 7.1. Each of the transformations evolves the quadrature vector $Z = \{X_1, Y_1, X_2, Y_2\}^{\mathrm{T}}$ to MZ. The matrix M that describes the transformation is a real 4×4 matrix in the symplectic group $\mathrm{Sp}(4, \mathbb{R})$ [134]. The quadratures of the transformed state will have the covariance matrix $M\Sigma M^{\mathrm{T}}$, where Σ was the covariance matrix of the original state. The squeezing of mode 1 by amount s is described by

$$S(s) = \begin{bmatrix} \frac{1}{\sqrt{s}} & 0 & 0 & 0 \\ 0 & \sqrt{s} & 0 & 0 \\ 0 & 0 & 1 & 0 \\ 0 & 0 & 0 & 1 \end{bmatrix}. \tag{7.1}$$

A beam splitter of transmissivity t is described by

$$B(t) = \begin{bmatrix} \sqrt{t} & 0 & -\sqrt{1-t} & 0 \\ 0 & \sqrt{t} & 0 & -\sqrt{1-t} \\ \sqrt{1-t} & 0 & \sqrt{t} & 0 \\ 0 & \sqrt{1-t} & 0 & \sqrt{t} \end{bmatrix}. \tag{7.2}$$

The phase shifts imparted as the states of the two modes propagates from the input of the SQ to the input of the measurement chains are represented with ϕ_1 and ϕ_2, respectively. The operation

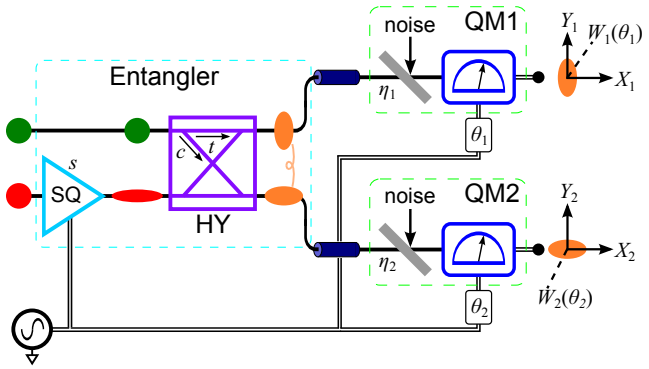

Figure 7.1: Single-squeezer model (SSM) of the experiment. The squeezer (SQ) prepares a squeezed state with squeezing parameter s, where the variance of the squeezed quadrature is $1/(2s)$. The squeezed state (red ellipse) and the unsqueezed input (green circle) are combined on a quadrature hybrid (HY) to generate entangled modes. The hybrid has a power transmission coefficient t and a power coupling coefficient $c = 1 - t$. The two output modes (orange ellipses) of the hybrid propagate onto two physically separate transmission lines and are fed to the two-channel measurement apparatus to measure quadrature amplitudes $W_1(\theta_1)$ and $W_2(\theta_2)$. The measurement apparatus consists of two single-quadrature measurement chains (QM1 and QM2). All sources of loss and measurement inefficiencies are modeled by introducing two fictitious beam splitters with power transmission coefficients η_1 and η_2, respectively. All the microwave components and cables are considered lossless; their imperfections are absorbed into the experimentally determined η_1 and η_2. The two squeezed states arrive at the two VERs with fixed but uncontrolled phase shifts ϕ_1 and ϕ_2, respectively. I mathematically adjust the reference phases to align the squeezed states with X_1 and X_2 as illustrated.

of phase shifting mode 1 by ϕ_1 and mode 2 by ϕ_2 is described by

$$P(\phi_1, \phi_2) = \begin{bmatrix} \cos(\phi_1) & \sin(\phi_1) & 0 & 0 \\ -\sin(\phi_1) & \cos(\phi_1) & 0 & 0 \\ 0 & 0 & \cos(\phi_2) & \sin(\phi_2) \\ 0 & 0 & -\sin(\phi_2) & \cos(\phi_2) \end{bmatrix}. \tag{7.3}$$

Beginning with an initial thermal (nearly vacuum) state, $\Sigma_0 = \sigma\mathbb{I}$, (with $\mathbb{I}$ being the identity matrix and σ being the input variance with $\sigma = 1/2$ for the vacuum), I compute the state just prior to measurement to be

$$\Sigma_p = P(\phi_1, \phi_2)B(t)S(s)\Sigma_0 S(s)^{\mathrm{T}} B(t)^{\mathrm{T}} P(\phi_1, \phi_2)^{\mathrm{T}}. \tag{7.4}$$

To account for photon loss I append two ancilla modes, which are coupled to modes 1 and 2 with beam splitters $B(\eta_1)$ and $B(\eta_2)$ respectively. After this coupling, the ancilla modes are discarded. This procedure transforms Σ_p into

$$\Sigma_{\mathrm{ss}} = \begin{bmatrix} \eta_1 & 0 & 0 & 0 \\ 0 & \eta_1 & 0 & 0 \\ 0 & 0 & \eta_2 & 0 \\ 0 & 0 & 0 & \eta_2 \end{bmatrix} \Sigma_p + \begin{bmatrix} 1-\eta_1 & 0 & 0 & 0 \\ 0 & 1-\eta_1 & 0 & 0 \\ 0 & 0 & 1-\eta_2 & 0 \\ 0 & 0 & 0 & 1-\eta_2 \end{bmatrix} \sigma\mathbb{I}. \tag{7.5}$$

7.1.2 Implementation and operation of the experiment

In the two-mode entanglement experiment, JPAs are the critical devices for both the entanglement generation and verification. One JPA (SQ) is used to prepare the squeezed states required to generate entanglement and two more JPAs (VERs) are employed to perform efficient quadrature measurements. We build two superconducting Niobium circuits, fabricated using optical-lithography with a standard Nb/AlO_x/Nb trilayer process [122, 127], to construct the SQ and the VER, respectively.

For the entanglement generation, we build an integrated circuit called the entangler to minimize loss in the entanglement generation process. The entangler integrates two 20 dB directional

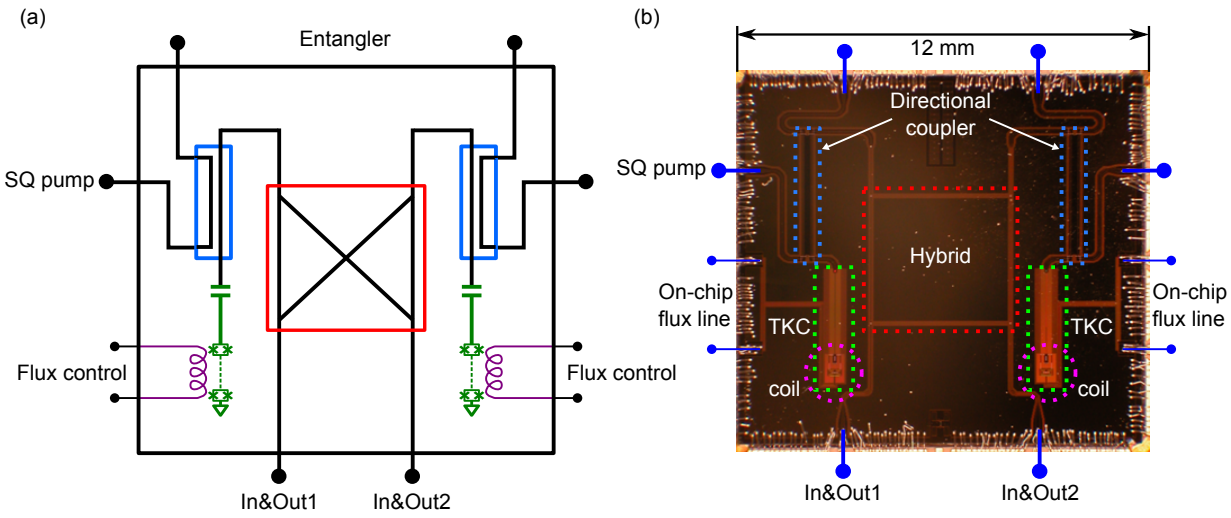

Figure 7.2: Entangler chip. (a) Microwave circuit diagram of the entangler chip. It integrates a quadrature hybrid (red) for entangling the two modes and two 20 dB directional couplers (blue) along with two TKCs (green) that constitute two SQs. The TKC is a $\lambda/4$ coplanar waveguide resonator terminated with a SQUID array with 20 squids. The resonance frequency of the TKC is tuned by applying an external magnetic flux (purple) to the squids' loop. (b) Image of the entangler chip. It shows the physical images of the hybrid (red), directional couplers (blue), and TKCs (green). For the flux controls of the TKCs, I can either use the on-chip flux bias lines or the superconducting magnetic coils directly held above the two squid arrays of the TKCs (magenta).

couplers, two TKCs, and a microwave quadrature hybrid as shown in Fig. 7.2. The directional couplers and the TKCs together with the off-chip circulators form two SQs. By operating both SQs, I can, in principle, inject two squeezed states into the two inputs of the hybrid. For the current experiment, I operate only one SQ to reduce the experimental complexity; the other SQ is not pumped, and its resonance frequency is tuned at least 500 MHz away from the other pump frequency. The resonance frequencies of the two SQs are tuned by an external magnetic flux. The magnetic flux can be applied either by on-chip–flux-bias lines or external superconducting magnetic coils in our experimental setup.

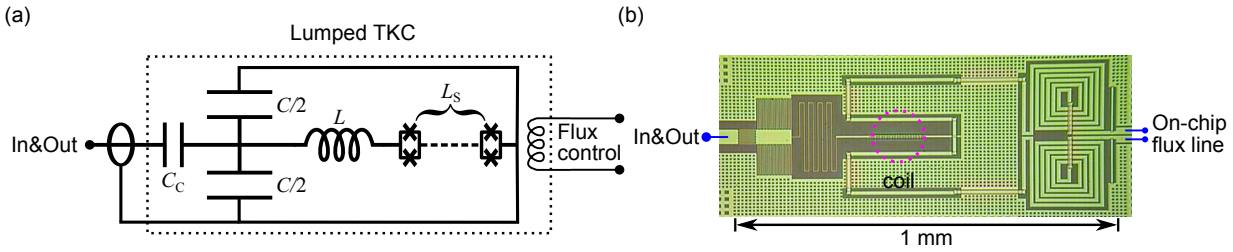

Figure 7.3: Lumped-element TKC chip. (a) Electrical circuit diagram of the lumped-element TKC. The lumped TKC is a nonlinear parallel LC oscillator coupled to the transmission line via the coupling capacitance $C_c = 24$ fF. The LC oscillator has capacitance $C = 0.24$ pF and inductance $L_{\rm tot} = L + L_s$, where $L = 1.4$ nH is the geometrical inductance and L_s is the flux-tunable Josephson inductance of the squid array with 20 squids. When no external flux is applied $L_s = 0.6$ nH. The resonance frequency can be tuned by an external magnetic flux. (b) Image of the lumped TKC chip. The TKC consists of two interdigitated capacitors and a long meander line with a squid array. The resonance frequency of the lumped TKC can also be tuned either by the on-chip flux line or an external magnetic coil (magenta).

For the entanglement verification, we implement a two-channel–quadrature-measurement apparatus where each channel uses a VER as the ultralow-noise preamplifier (Fig. 7.3). The VER is formed with a lumped-element TKC, a commercial 20 dB directional coupler, and a commercial circulator. When operating the VERs, their resonance frequencies are tuned either by the flux-bias lines on the lumped TKC chips or by external magnetic coils near the chips.

To understand the operation of the experiment, it is useful to consider the diagram of the two-mode entanglement experiment shown in Fig. 7.4. The input states of the entangler are emitted from the two 50 Ω terminations on the circulators connected to the two input/output ports of the

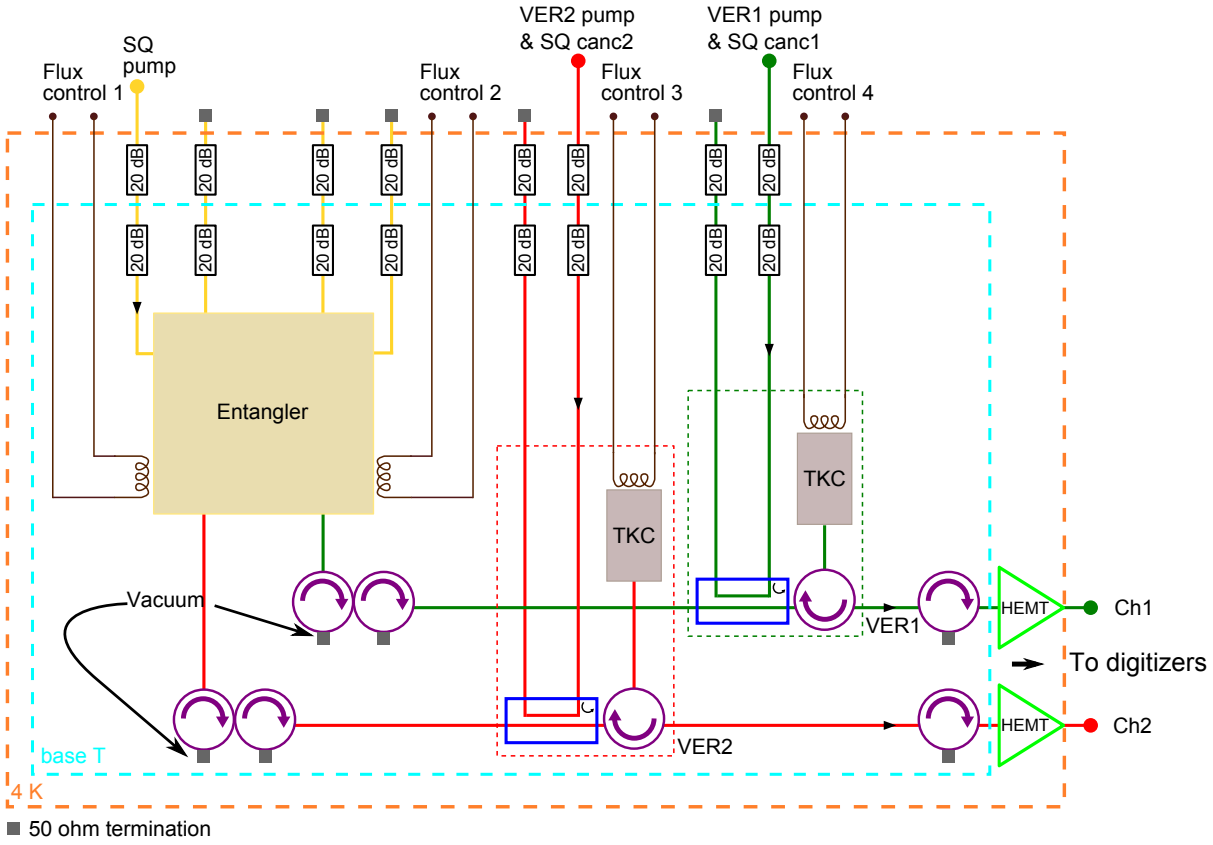

Figure 7.4: Experiment Diagram. The entangler processes the input states emitted from the 50 Ω terminations on the circulators (purple) and generates two-mode entangled states at the two output modes. To operate one of the SQs on the entangler, I inject a microwave pump field through a coaxial transmission line with 40 dB attenuation. The two output modes of the entangler are amplified by VER1 (red dashed rectangle) and VER2 (green dashed rectangle), respectively. The VER consists of a commercial 20 dB directional coupler (blue), a commercial circulator (purple), and a lumped TKC. Following the VERs are HEMT amplifiers (light green) at the 4 K stage and electronics at room temperature for further mixing and digitizing.

entangler. The two 50 Ω terminations are thermally anchored to the cryostat; thus the two inputs are in very nearly pure vacuum states (see next section).

To squeeze one of the input states, one SQ is pumped at $f_{\mathrm{s}} = 6.327$ GHz and generates a squeezed state with an approximate direct power gain of $G_{\mathrm{s}} = 3.1$ dB and a bandwidth of $B_{\mathrm{s}} = 8.5$ MHz. The squeezed state is displaced in phase space by the pump amplitude. This displaced-squeezed state and the other input state interfere in the hybrid, creating entanglement in the two output modes of the hybrid.

The output modes of the hybrid propagate in two separate coaxial cables that feed the input of VER1 or VER2, located about 10 cm apart, forming the first stages of the amplification of the two quadrature measurements. To ensure that the VERs are not saturated, I null the SQ pump tone at the input of the VERs with a weakly coupled coherent field. In addition, to isolate the SQ stage from the VERs' pumps and to isolate the VERs from each others' pumps, I install three circulators between the entangler outputs and VER inputs, providing more than 50 dB of isolation. VERs are operated with an approximate direct power gain of $G_{\mathrm{v}} = 22$ dB and a bandwidth of $B_{\mathrm{v}} = 2.3$ MHz. The VERs' outputs are further amplified by conventional microwave amplifiers and mixed down with copies of the VERs pump tones as the mixers' local oscillators.

Finally, the mixers' intermediate frequency outputs are filtered with a 1.9 MHz low pass filter and sampled at 10 MHz, yielding new measurements of $W_1(\theta_1)$ and $W_2(\theta_2)$ every 100 ns. The phases θ_1 and θ_2 can be independently adjusted relative to each other and relative to the squeezed quadrature of SQ. In practice, to adjust θ_1 and θ_2, I set the pump frequencies of VER1 and VER2 to be 1 kHz and 50 kHz above the SQ pump frequency respectively. In 1 ms, I acquire 10,000 samples covering the full range of both θ_1 and θ_2. I acquire data for 1 s, yielding 1,000 independent realizations of $(\theta_1, W_1(\theta_1), \theta_2, W_2(\theta_2))$.

7.2 Vacuum Calibration

In the two-mode entanglement experiment, I acquire not only the quadrature measurements $V_{i,\mathrm{on}}$ of the two-mode entangled state for modes $i = 1, 2$, but also the quadrature measurements

$V_{i,\mathrm{off}}$ for the input thermal (nearly vacuum) state by bypassing the SQ. I bypass the SQ by turning off its pump and operating it as a noiseless $G_s = 1$ amplifier. The variances $\mathrm{Var}(V_{i,\mathrm{off}})$ correspond to the fluctuations of the input states emitted from the terminations thermally anchored to the cryostat at temperature T_{f}. Generally, I do not assume the temperature T_{in} of the terminations to be equal to T_{f}. Thus, to express the variances in units of quantum vacuum at the input of the experiment, I need to measure T_{in}. Furthermore, I do not assume that the VERs are perfectly linear, but rather introduce two parameters g_1 and g_2 to model the possible small changes in VERs' gains when bypassing SQ. In this section, I present the thermal sweep experiment to measure T_{in} and explain how I extract the parameters g_1 and g_2 by jointly fitting the model equations to the measured variances.

7.2.1 Input variance calibration

When I demonstrate the two-mode entanglement experiment, I feed the entangler with two input states emitted from the two 50 Ω terminations thermally anchored to the cryostat. In additional to these two input states, more thermal (nearly vacuum) modes dilute the entangled state through the losses of the commercial microwave components, such as directional couplers and circulators. The temperatures of the input states and the loss modes are assumed to be equal to T_{in}. To measure T_{in}, I inject a series of known thermal states into the two measurement chains without pumping SQ. States of known noise are created by varying the temperature of the cryostat and therefore the 50 Ω terminations that feed the entangler. I then calculate the variances $\mathrm{Var}(V_1)$ and $\mathrm{Var}(V_2)$ of the two output measurements for each thermal input. I then fit the model

$$\mathrm{Var}(V) = G\left[\frac{1}{2}\coth\left(\frac{hf_s}{2k_{\mathrm{B}}T_{\mathrm{in}}}\right) + A(T_{\mathrm{F}})\right], \tag{7.6}$$

to the measured variances, where G and $A(T_{\mathrm{F}})$ are the power gain and the added noise of the measurement chain. In this model, $T_{\mathrm{in}} = \sqrt{T_{\mathrm{F}}^2 + T_{\mathrm{e}}^2}$ represents the input states temperature. T_{F} is the cryostat temperature, and I add one parameter T_{e} to allow for the possibility that the terminations equilibrate at a higher temperature than T_{F}. I also include a temperature dependent

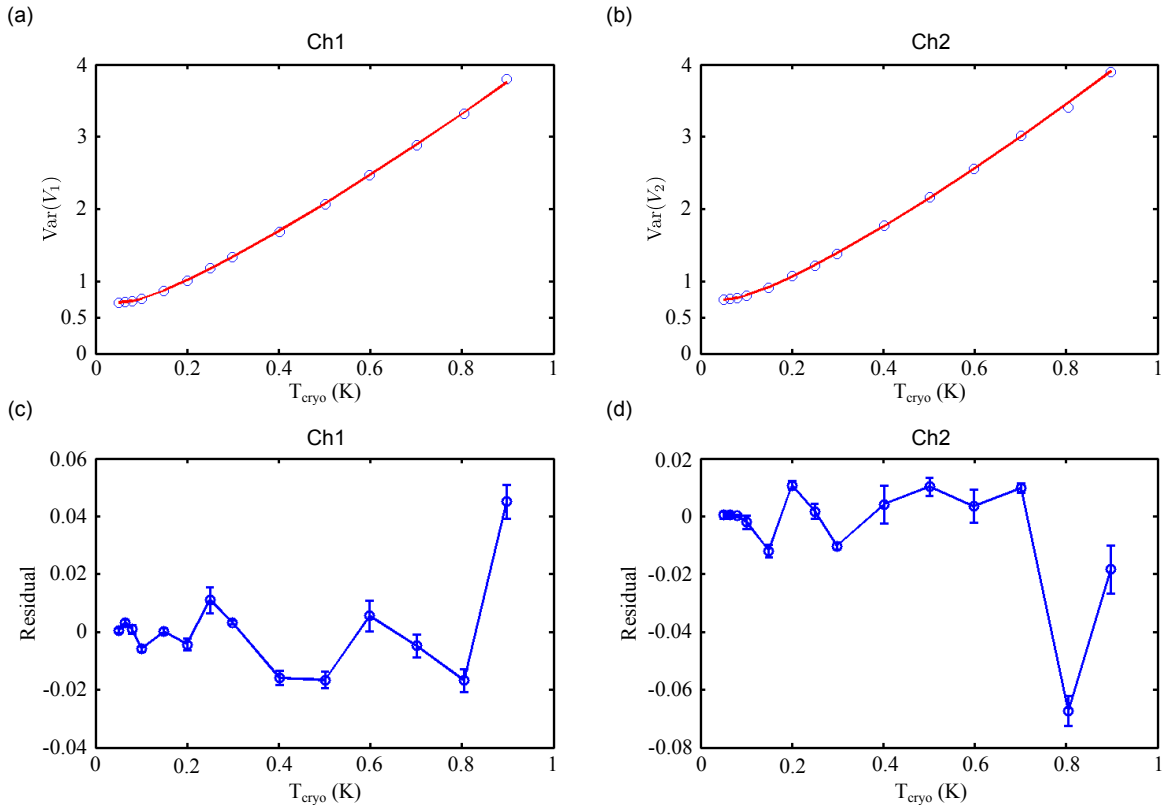

Figure 7.5: Thermal sweep experiment. The measured single-quadrature variances of the thermal sweep experiment (blue circles) and fit to Eq. (7.6) (red solid line) for channel 1 (a) and channel 2 (b) are plotted. The residuals of the two fits are plotted in (c) and (d) where the error bars show the standard deviation of five independent measurements made at each temperature point.

added noise $A(T_{\rm F}) = A_0 + A_2 T_{\rm F}^2$ in the model, because of the possible flux noise from the on-chip flux line. From the fit (Fig. 7.5), I extract $0 < T_{\rm e} < 16.1$ mK. Because the entanglement generation is performed with the cryostat below 25 mK, I have $T_{\rm in} < 29.7$ mK, which means the input variance is indistinguishable from vacuum in our experiments.

The origin of the temperature-dependent added noise in our JPAs can be caused by the presence of the resistive filters in the on-chip bias lines. The power spectral density of the thermal noise current $I_{\rm th}$ generated by the shunt resistors in the bias line is proportional to the temperature T of the resistors, $S_{I_{\rm th}} \propto T$. Thus, the magnetic flux Φ biasing the TKC also has a noise spectral density proportional to the temperature, $S_\Phi \propto T$. Furthermore, if I operate the TKC near its maximum frequency $\omega_{f,\rm max}$ with an external flux Φ_0, I can Taylor expand the resonance frequency ω_f with respect to Φ_0

$$\omega_f \approx \omega_f(\Phi_0) + \frac{1}{2}\omega_f''(\Phi_0)(\Phi - \Phi_0)^2 = \omega_f(\Phi_0) + \delta\omega_f, \tag{7.7}$$

which shows that the dominant term contributes to the fluctuation of the resonance frequency is the Φ^2 term. Consequently, the fluctuation of the resonance frequency is proportional to T^2, $\delta\omega_f \propto T^2$, which justifies our temperature-dependent added noise model $[A(T) = A_0 + A_2 T^2]$.

7.2.2 Parametric gain variations

The experiment's data set contains amplified quadrature measurements $V_{i,\rm off}$ (measured by bypassing SQ) of the vacuum state and quadrature measurements $V_{i,\rm on}$ of the entangled state for modes $i = 1, 2$. Those variances, measured by digitizing the amplified voltages at room temperature, must be calibrated in units of quantum vacuum at the input of the experiment. To calibrate the variances of the measurements in units of vacuum, I first normalize the quadrature measurements of the two entangled modes by the variances of the vacuum states to get $U_1(\theta_1)$ and $U_2(\theta_2)$

$$U_1(\theta_1) = \frac{V_{1,\rm on}(\theta_1)}{\sqrt{\rm Var}(V_{1,\rm off})} \quad \text{and} \quad U_2(\theta_2) = \frac{V_{1,\rm on}(\theta_2)}{\sqrt{\rm Var}(V_{2,\rm off})}. \tag{7.8}$$

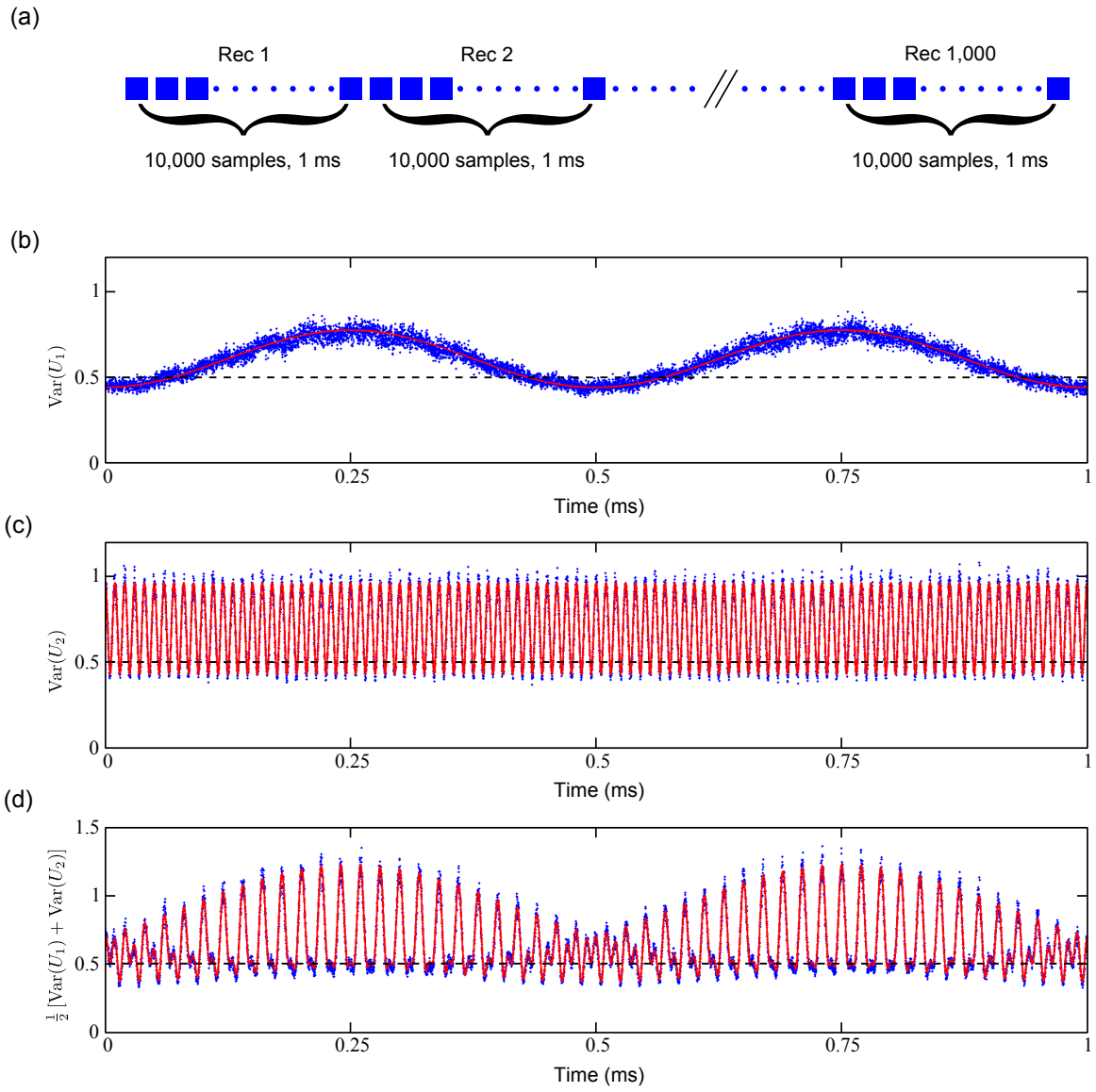

Figure 7.6: Joint fit of the model to the measured variances. (a) The cartoon diagram represents the timing of the quadrature measurements. Each measurement is a one second long time trace with each channel at 10 MSamples/s. Because the pumps of VER1 and VER2 are detuned from the SQ pump by 1 kHz and 50 kHz, respectively, the two VERs amplify the measured states at 10,000 different quadrature phase combinations every 1 ms (one record). In a 1 s long time trace, I thus have 1000 records, or realizations at each quadrature phase pair. The variance at each quadrature phase pair is then calculated from the corresponding data points in each record. The measured variances of (b) $U_1(\theta_1)$, of (c) $U_2(\theta_2)$, and of (d) $1/2\,[U_1(\theta_1) + U_2(\theta_2)]$ are plotted versus time in each measurement record (blue dot) along with the joint fit of Eqs. (7.9)–(7.11) to all of the measured variances (red solid line). The model and data show good agreement with each other and I observe moderate squeezing below vacuum fluctuation (0.5) in the variance of each mode [(b) and (c)], and enhanced squeezing from (d).

Furthermore, I derive the equations for variances of $U_1(\theta_1)$, of $U_2(\theta_2)$, and of $U_1(\theta_1) \pm U_2(\theta_2)$ from the single-squeezer model

$$\mathrm{Var}\left[U_1(\theta_1)\right] = g_1 \left[1 + \frac{1}{2}\frac{(s-1)^2}{s}\alpha + \frac{1}{2}\frac{s^2-1}{s}\alpha\cos(2\theta_1 + 2\phi_1)\right], \tag{7.9}$$

$$\mathrm{Var}\left[U_2(\theta_2)\right] = g_2 \left[1 + \frac{1}{2}\frac{(s-1)^2}{s}\beta + \frac{1}{2}\frac{s^2-1}{s}\beta\cos(2\theta_2 + 2\phi_2)\right], \tag{7.10}$$

$$\begin{aligned}\mathrm{Var}\left[U_1(\theta_1) \pm U_2(\theta_2)\right] &= \mathrm{Var}(U_1) + \mathrm{Var}(U_2) \\ &\pm \sqrt{g_1 g_2}\left[\frac{s^2-1}{s}\sqrt{\alpha\beta}\cos(\theta_1 + \theta_2 + \phi_1 + \phi_2) + \frac{(s-1)^2}{s}\sqrt{\alpha\beta}\cos(\theta_2 - \theta_1 + \phi_2 - \phi_1)\right],\end{aligned} \tag{7.11}$$

where s is the squeezing parameter such that the variance of the squeezed quadrature is $1/(2s)$. The parameters α and β combine the hybrid power coupling coefficient t and the two measurement efficiencies η_1 and η_2

$$\alpha = t\eta_1 \quad \text{and} \quad \beta = (1-t)\eta_2.$$

I do not assume that the VERs are perfectly linear, but rather introduce two parameters g_1 and g_2 to model the changes in VERs' gains when bypassing SQ:

$$g_1 = \frac{g_{1,\mathrm{on}}}{g_{1,\mathrm{off}}} \quad \text{and} \quad g_2 = \frac{g_{2,\mathrm{on}}}{g_{2,\mathrm{off}}},$$

where $g_{1,\mathrm{on}}$ and $g_{1,\mathrm{off}}$ are quadrature power gains of mode 1 for SQ is operated or bypassed and the same for mode 2. Finally, from the joint fit of the model equations [Eqs. (7.9)–(7.11)] to the measured $\mathrm{Var}(U_1)$, $\mathrm{Var}(U_2)$, and $\mathrm{Var}(U_1 \pm U_2)$ [Figs. 7.6(b)–(d)], I extract $s = 5.41 \pm 0.03$, $\alpha = 0.1304 \pm 0.0007$, $\beta = 0.202 \pm 0.001$, $\phi_1 = -1.070 \pm .0.002$, $\phi_2 = -0.176 \pm 0.001$, $g_1 = -1.70 \pm 0.07\%$, and $g_2 = 2.04 \pm 0.08\%$. I then are able to use g_1, g_2, and T_{in} to calibrate the quadrature measurements in units of vacuum:

$$W_1(\theta_1) = \frac{U_1(\theta_1)}{\sqrt{g_1}}\frac{\sigma}{0.5} \quad \text{and} \quad W_2(\theta_2) = \frac{U_2(\theta_2)}{\sqrt{g_2}}\frac{\sigma}{0.5},$$

where $\sigma = (1/2)\coth(hf_s/2k_{\mathrm{B}}T_{\mathrm{in}})$.

7.3 Results and analysis

In this section, I first present the measurement results of the quadrature variances calibrated in units of vacuum. Then, I extract the SSM parameters by the joint fitting of the model equations to the measured quadrature variances and then calculate the covariance matrix from the extracted parameters. After obtaining the covariance matrix, I can calculate the entanglement witness and the negativity to demonstrate entanglement.

7.3.1 Measured variances of two-mode measurements

I first examine the quadrature variances measured separately at the outputs of the two measurement chains. From the measured quadrature variance of each mode, $\mathrm{Var}(W_1)$ and $\mathrm{Var}(W_2)$ [Fig. 7.7(a) and (b)], I observe an approximate minimum variance 15% below vacuum fluctuation, i.e. 15% squeezing below vacuum. Furthermore, $\mathrm{Var}(W_1)$, only depends on the measurement phase θ_1 and is independent of the measurement phase θ_2; likewise, $\mathrm{Var}(W_2)$ depends only on θ_2. These plots demonstrate that the two VERs are unaffected by the phases of the other's pump and by the phase of the SQ pump, indicating that the two channels are well decoupled and the SQ pump is successfully nulled at the input of the VERs.

By making joint measurements of the two output modes, I detect the correlations between them and reveal that they are entangled. In Fig. 7.7(c) I plot the measured joint variance $(1/2)\mathrm{Var}(W_1 + W_2)$, and in Fig. 7.7(d) I show the expected joint variance predicted by the single squeezer model in Fig. 7.1. Because the squeezing I observe from separate measurements is diluted with vacuum (Fig. 7.1), I anticipate that the joint measurements will show more squeezing than the separate measurements. Indeed, $(1/2)\mathrm{Var}(W_1 + W_2)$ has an approximate minimum variance 25% below vacuum fluctuation. The hybrid generates a two-mode entangled state, distributing the nonclassical correlation present in the input squeezed state into the two output modes. By inverting the hybrid's action, the two input states can be reconstructed from the joint measurements. For example, only the squeezed input contributes to the variance measured along the magenta-diamond

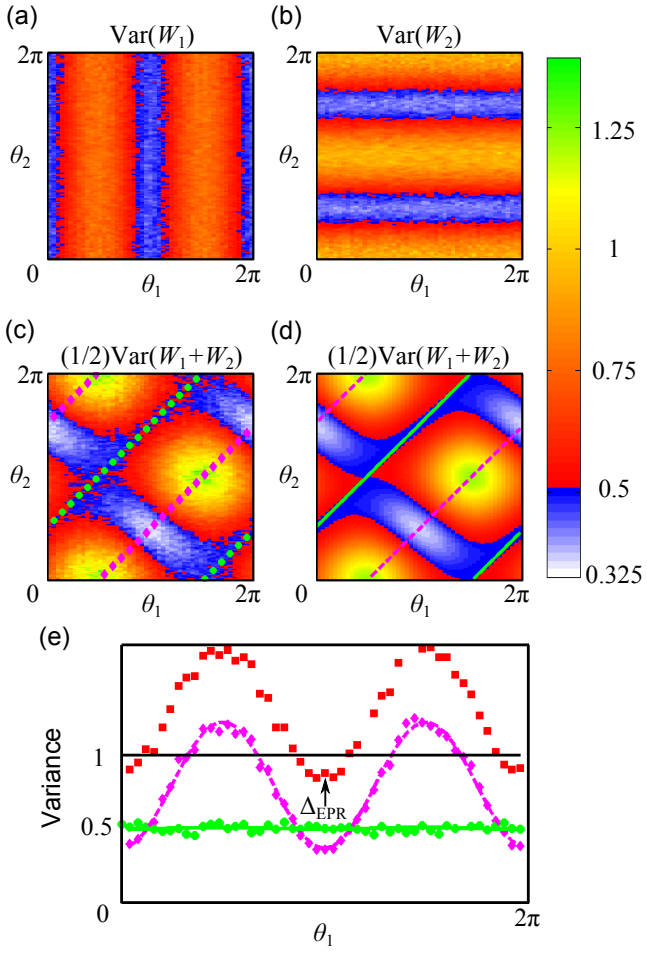

Figure 7.7: Separate and joint variances. Shown are intensity plots of the measured variances of (a) $W_1(\theta_1, \theta_2)$, of (b) $W_2(\theta_1, \theta_2)$, and of (c) $\frac{1}{2}\left[W_1(\theta_1, \theta_2) + W_2(\theta_1, \theta_2)\right]$ calibrated in units of the vacuum versus the two quadrature phases θ_1 and θ_2. (d) An expectation of (c) predicted by the single squeezer model represented by Fig. 7.1. (e) The variances along the corresponding annotated lines in (c) and (d) are plotted versus quadrature phase θ_1 of channel 1. The red squares are the sum of the green-circle line and the magenta-diamond line, where the green-circle line is shifted by $\frac{\pi}{2}$ in θ_1. The arrow indicates the observed value of $\Delta_{\mathrm{EPR}} < 1$.

line in Fig. 7.7(c); likewise, only the vacuum input contributes to the variance measured along the green-circle line [Fig. 7.7(e)].

To intuitively understand the relation between the entanglement witness E_{w} (Eq. 2.87) and the joint variance $(1/2)\mathrm{Var}(W_1 + W_2)$, I first rewrite Eq. 2.87 as

$$E_{\mathrm{W}} = \min_{a,\theta_1,\theta_2} \{ \mathrm{Var}\left[|a|\, W_1(\theta_1) + \frac{1}{a} W_2(\theta_2)\right] + \mathrm{Var}\left[|a|\, W_1(\theta_1 + \frac{\pi}{2}) - \frac{1}{a} W_2(\theta_2 + \frac{\pi}{2})\right] - \left(a^2 + \frac{1}{a^2}\right)\Big\}, \tag{7.12}$$

where $E_{\mathrm{W}} < 0$ is evidence of entanglement. In the above expression, I optimize the entanglement witness over phase rotations θ_1 and θ_2 and the number a. I then define a quantity Δ_{EPR} for the choice of $a = 1$

$$\Delta_{\mathrm{EPR}} = \frac{1}{2}\mathrm{Var}\left[W_1(\theta_1) + W_2(\theta_2)\right] + \frac{1}{2}\mathrm{Var}\left[W_1\left(\theta_1 + \frac{\pi}{2}\right) - W_2\left(\theta_2 + \frac{\pi}{2}\right)\right], \tag{7.13}$$

which gives evidence of entanglement when $\Delta_{\mathrm{EPR}} < 1$. One method of estimating Δ_{EPR} is to sum the respective green circles and magenta diamonds in Fig. 7.7(e). Thus, by direct inspection of the joint variance, this $\Delta_{\mathrm{EPR}} < 1$ from the measured joint variances already suggests that the two modes are entangled.

7.3.2 Entanglement witness and negativity

From the joint fit of the measured variances, I not only extract the gain variation parameters g_1 and g_2, but also extract the SSM parameters as already shown in Sec. 7.2.2. With these extracted parameters, I can calculate the covariance matrix of the two-mode state by using Eq. 7.5. Consistent with the measured variances (Fig. 7.7), the elements of the covariance matrix show both modest squeezing within each mode, and stronger intermode correlations (Fig. 7.8).

Given a covariance matrix Σ, I compute the value of the entanglement witness E_{W} shown in Eq. 7.12 by

$$E_{\mathrm{W}} = \min_{a,\theta_1,\theta_2} \left[{a_x}^{\mathrm{T}} P(\theta_1,\theta_2)\Sigma P(\theta_1,\theta_2)^{\mathrm{T}} a_x + {a_y}^{\mathrm{T}} P(\theta_1,\theta_2)\Sigma P(\theta_1,\theta_2)^{\mathrm{T}} a_y - \left(a^2 + \frac{1}{a^2}\right)\right], \tag{7.14}$$

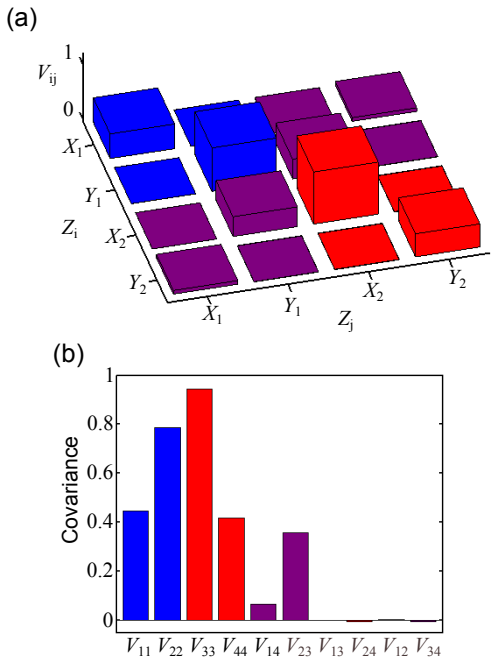

Figure 7.8: Covariance matrix of the two-mode state. (a) The covariance matrix calculated from the single squeezer model parameter extracted by joint fitting of measured variances. (b) The 10 independent elements of the covariance matrix are shown for the same data as (a). The reference phases has been adjusted in the same manner as in Fig. 7.7.

where ${a_x}^{\mathrm{T}} = (|a|, 0, 1/a, 0)$, ${a_y}^{\mathrm{T}} = (0, |a|, 0, -1/a)$, and $P(\theta_1, \theta_2)$ is the phase rotation matrix Eq. (7.3). In fact, E_{W}'s only dependence on θ_1 and θ_2 appears in the form $\theta_1 - \theta_2$, so it is only necessary to minimize over one phase.

To compute the entanglement negativity from a covariance matrix, I follow the treatment given in [88]. Through the application of linear optical devices and squeezing (the symplectic transformations), any two-mode covariance matrix Σ can be transformed into the covariance matrix of a thermal state, which has the form $\mathrm{diag}(\nu_1, \nu_1, \nu_2, \nu_2)$. ν_1 and ν_2 are called the symplectic eigenvalues of Σ. According to the Heisenberg Uncertainty Principle, ν_1 and $\nu_2 \geq 1/2$. If the quantum state ρ with covariance matrix Σ is separable, then covariance matrix $\tilde{\Sigma}$ of the partial transpose of ρ will also have symplectic eigenvalues $\tilde{\nu_1}$ and $\tilde{\nu_2} \geq 1/2$. If $\tilde{\nu_1}$ or $\tilde{\nu_2} < 1/2$, ρ must be entangled. To compute the symplectic eigenvalues of $\tilde{\Sigma}$, I divide Σ into 2×2 blocks:

$$\Sigma = \begin{pmatrix} A & \Gamma \\ \Gamma^{\mathrm{T}} & B. \end{pmatrix} \tag{7.15}$$

The quantities $|\Sigma|$ and $\Delta(\Sigma) = |A| + |B| + 2|\Gamma|$ are invariant under the symplectic transformations. ($|\cdot|$ denotes the determinant.) From them I calculate the symplectic eigenvalues:

$$\nu_i = \sqrt{\frac{1}{2}\left(\Delta(\Sigma) \pm \sqrt{[\Delta(\Sigma)]^2 - 4|\Sigma|}\right)}, \tag{7.16}$$

where I use $i = 1$ for the $-$ case and $i = 2$ for the $+$ case. The partial transposition of ρ has the effect of reversing the sign of the Y quadrature of the transposed mode, so that $\Delta(\tilde{\Sigma}) = |A| + |B| - 2|\Gamma|$, but $|\tilde{\Sigma}| = |\Sigma|$. The symplectic eigenvalues of $\tilde{\Sigma}$ are

$$\tilde{\nu_i} = \sqrt{\frac{1}{2}\left(\Delta(\tilde{\Sigma}) \pm \sqrt{[\Delta(\tilde{\Sigma})]^2 - 4|\Sigma|}\right)}, \tag{7.17}$$

If $\tilde{\nu_1} < 1/2$, ρ is an entangled state. Finally, the negativity is

$$N = \max\left(0, \frac{\frac{1}{2} - \tilde{\nu_1}}{2\tilde{\nu_1}}\right). \tag{7.18}$$

Note that our formula for N is slightly different from that in [88], because that paper uses the convention that the variance of the vacuum state is 1, whereas I use vacuum variance of $1/2$.

From the covariance shown in Fig. 7.8, I obtain the entanglement witness $E_{\mathrm{W}} = -0.263 \pm 0.001$ with $a = 1.11$ and the negativity $N = 0.0824 \pm 0.0004$. The uncertainties of E_{W} and N are estimated from a parametric bootstrap method. In the bootstrap procedure, 20 simulated data sets are generated from the measured covariance matrix. I estimated statistical uncertainties as equal to the standard deviation of the 20 estimates E_{W} and N found by analyzing the simulated data sets in the same manner used for analyzing real data.

To demonstrate the repeatability and stability of the entanglement generation, I perform 100 trials of the experiment. The distribution of E_{W} and N calculated from 100 trials appear to be Gaussian with a mean $\pm$ standard deviation of $E_{\mathrm{W}} = -0.264 \pm 0.002$ and $N = 0.0820 \pm 0.0007$ as shown in Fig. 7.9.

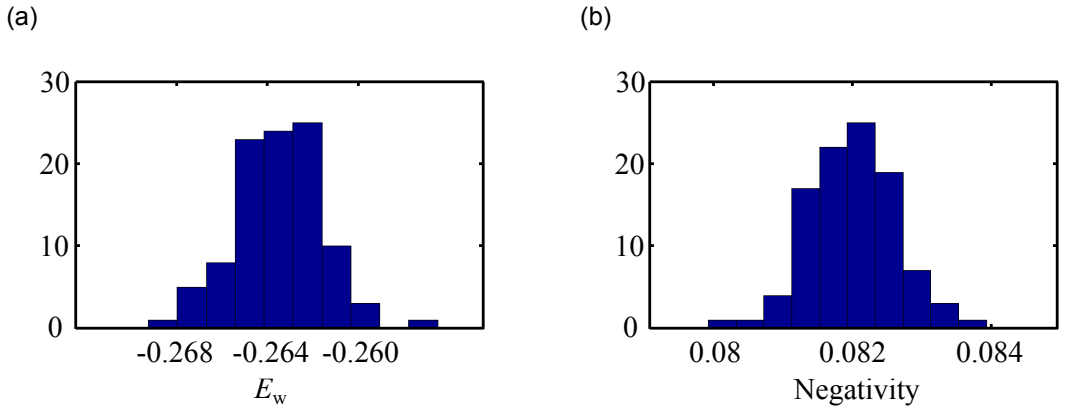

Figure 7.9: Histograms of the entanglement witness and the negativity. The histograms of 100 trials of (a) the entanglement witness E_{W} and (b) the negativity N appear to be Gaussian with $E_{\mathrm{W}} = -0.264 \pm 0.002$ and $N = 0.0820 \pm 0.0007$.

Because I acquire a large data set in a short time, the statistical uncertainties of E_{W} and N are low compared to the systematic errors. I estimate the systematic errors by analyzing experimental data with a general Gaussian model (see appendix A). Whereas the single squeezer model restricts possible estimated covariance matrices to those generated by a single mode squeezer, beam splitter, and loss, the Gaussian model allows any two-mode state described by a Gaussian Wigner function. Using this Gaussian model, I found that $E_{\mathrm{W}} = -0.297 \pm 0.002$ and $N = 0.0921 \pm 0.0004$, where the

uncertainties are based on a similar parametric bootstrap method to that described above. The discrepancy between the parameters estimated by the single squeezer model and the Gaussian model reveals a systematic error that is significantly larger than any statistical uncertainty and uncertainty in the variances of the calibration state. Considering this systematic error, I conclude that the state in our experiment has $E_{\mathrm{W}} = -0.263^{+0.001}_{-0.036}$ and $N = 0.0824^{+0.0101}_{-0.0004}$, where the uncertainties include the estimates from both models.

The observed negativity is small compared to $N = 0.55 \pm 0.04$ from [76], but that negativity is an inference of the negativity in the absence of measurement inefficiency. In contrast to Ref. [76, 83, 84], I state the negativity without correcting for inefficiency. In comparison to the approximately 2% efficiency achieved in a measurement apparatus using HEMTs as the first stage of amplification, our apparatus achieves measurement efficiencies at least $\eta_1 = 26 \pm 0.1\%$ and $\eta_2 = 40 \pm 0.2\%$ (To quote these efficiencies, I assume $t = 0.51$ based on the calibrated measurements of the hybrid [90]). The efficiencies include any noise in the squeezed state's generation and any loss along the entire path from state generation to measurement, in other words, the quoted values are lower bounds of the detection efficiencies. Because I know only lower bounds on the detection efficiencies I am unable to estimate the negativity (or other properties) of the generated state in the absence of measurement inefficiency.

In conclusion, I demonstrate a two-channel, single-quadrature quantum measurement apparatus in the microwave regime, where each channel of the apparatus uses a JPA as its first stage amplifier. A two-mode entangled state, which is generated by combining a squeezed state and vacuum on a microwave hybrid, is measured with improved efficiency and independent choices of each mode's measured quadratures. Entanglement is demonstrated by showing the two-mode state violates the separability criterion. Our integration of JPAs for both the preparation and measurement of an entangled state is a substantial addition to the toolbox for manipulating continuous variable quantum states of microwave modes. The measurement scheme is promising for demonstrating protocols exploiting entanglement.

Chapter 8

Conclusion and future works

In the thesis, I have presented our approach to achieving our goals on generating and verifying entanglement between itinerant microwave fields. We first separately design and characterize the required Josephson parametric amplifiers (JPAs) and linear passive components. We then combine them to demonstrate on-demand generation of entangled pairs of propagating microwave fields. We also develop a two-channel measurement apparatus that allows us to verify the entangled states with efficient and independent joint measurements.

In this section, I review the major experimental results and discuss future work on improving the amount of entanglement generated and the detection efficiency. I also discuss a possible scheme for performing teleportation of quantum states of itinerant microwave fields using our current experimental techniques.

8.1 Conclusion

In this thesis, I present the research project of generating and verifying distributable microwave entanglement. We first perform state tomography of an itinerant squeezed state of the microwave field prepared by a Josephson parametric amplifier (JPA). In this tomography experiment, we use a second JPA as a preamplifier to improve the quantum efficiency of the quadrature measurement from 2% to $36 \pm 4\%$. Without correcting for the detection inefficiency, we observe a minimum quadrature variance of $68^{+9}_{-7}\%$ of the variance of the vacuum. We also use maximum-likelihood quantum state tomography to deconvolve the measurement inefficiency in order to pre-

cisely characterize the state generated.

We then design, simulate, and measure two superconducting passive microwave components: a quadrature hybrid and a 20 dB directional coupler. For the hybrid performance, we measure an isolation of 20 dB and an insertion loss of 0.3 dB in a 10% band around 6.5 GHz. For the coupler, we measure a return loss and an isolation of 20 dB, and an insertion loss 0.3 dB in a 2 GHz band around 6 GHz. These components are designed to be integrated with JPAs for generating entanglement and performing efficient quadrature measurements.

Finally, we design and fabricate an integrated entangler chip to generate distributable entanglement. The entangler is capable of combining a squeezed propagating microwave field and a vacuum field on a hybrid and then generating entanglement between its two output modes. By employing JPAs based on amplifier chains, we verify the entangled state by making independent single-quadrature measurements of the two output modes with efficiencies at least $26 \pm 0.1\%$ and $40 \pm 0.2\%$, respectively. Entanglement is demonstrated by showing that the two-mode state violates the separability criterion with an entanglement witness $E_{\mathrm{W}} = -0.263^{+0.001}_{-0.036}$. We also calculate the negativity $N = 0.0824^{+0.0101}_{-0.0004}$. Our integration of JPAs for both the preparation and measurement of an entangled state is a substantial addition to the toolbox for manipulating continuous-variable quantum states of microwave modes. The measurement scheme is promising for demonstrating protocols exploiting entanglement.

8.2 Future work

After gaining the ability to generate entanglement and performing efficient measurements, the next step for microwave continuous-variable quantum information processing could be demonstrating a quantum teleportation protocol. Quantum teleportation is a reliable scheme for transferring quantum information to distant places. While it is impossible to transfer a general quantum state from a sender to a distant receiver solely via classical channels, a quantum teleportation protocol utilizes the shared entanglement between the two parties to accomplish the task. One such protocol was first proposed by Bennett in 1993 for the discrete qubit system [16] and later by Vaidman

in 1994 for a continuous-variable system [17]. By considering the finite quantum correlation and nonideal detection efficiency, Braunstein and Kimble proposed an experimental implementation for the teleportation of a continuous-variable system [18].

The general idea of the protocol to transfer an unknown quantum state $|\Psi\rangle$ from the sender (Alice) to the receiver (Bob) consists of the following four steps (Fig. 8.1):

(1) Alice and Bob share an ancillary entangled state (EPR state).

(2) Alice performs a joint measurement on the state $|\Psi\rangle$ and her half of the entangled pair (Bell measurement).

(3) Alice sends the measurement outcome to Bob via classical communication channels.

(4) Bob performs unitary transformations on his half of the entangled pair based on the received classical information, and then $|\Psi\rangle$ reappears in Bob's place.

By performing these steps, the unknown state $|\Psi\rangle$ is destroyed in Alice's station and then is transferred to Bob's place.

The experimental techniques we developed for generating two-mode entanglement and performing efficient quantum measurements are important building blocks for implementing quantum teleportation in a microwave system (Fig. 8.2). The required EPR pair in the protocol step (1) would be the two-mode entangled state generated by combining two squeezed states, which are generated independently from two Josephson parametric amplifiers, on a microwave hybrid. The input mode is coupled to Alice's EPR mode on a hybrid, and then two quadrature measurements are performed on its two output modes, respectively, to complete the Bell measurement in step (2). The two measurement results are sent to Bob via classical communication. Finally, Bob can displace his EPR mode in phase space based on the knowledge received from Alice. This phase-space displacement can be performed by coupling the classical signals to Bob's EPR mode via a directional coupler.

Generally, the fidelity of a teleportation protocol is improved with a larger amount of the

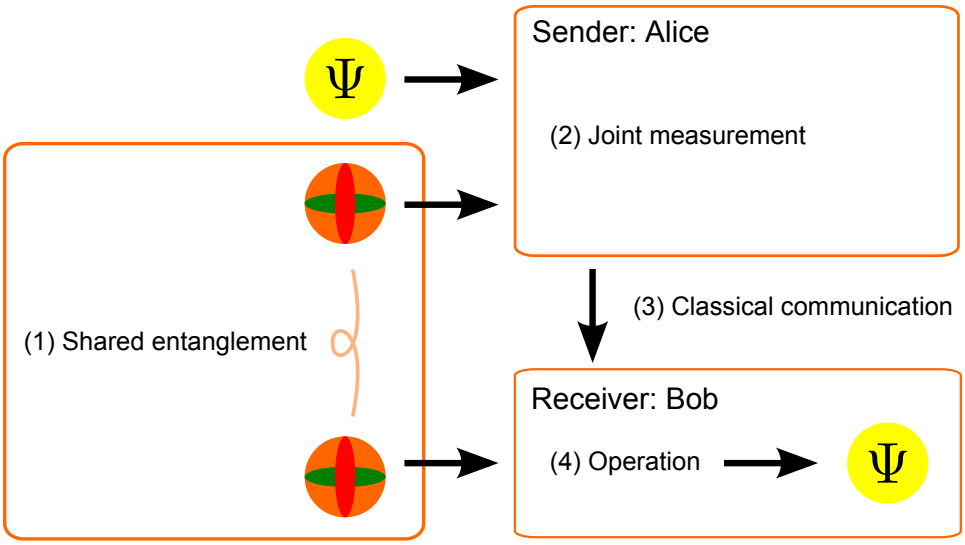

Figure 8.1: Principle of quantum teleportation. An unknown quantum state $|\Psi\rangle$ is teleported from the sender to the receiver in the four steps (1–4) shown here. The central resource of the protocol is the shared entanglement between the sender and the receiver. By using classical information from the sender, which are the outcomes of joint measurements made by the sender, the receiver transforms the entangled state to regenerate the input state $|\Psi\rangle$.

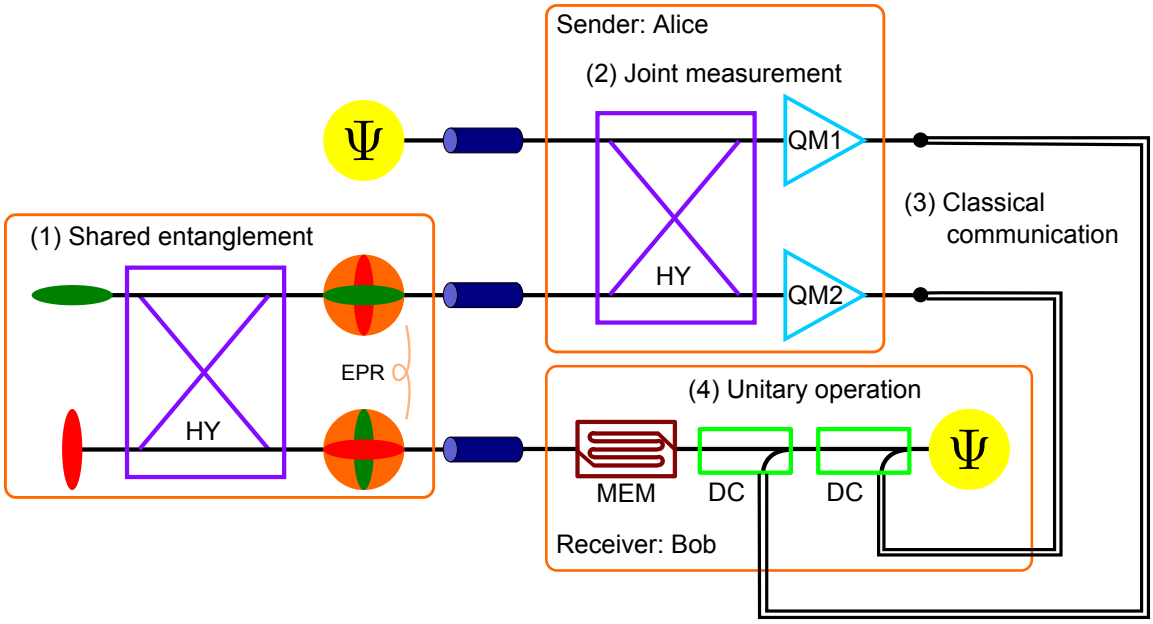

Figure 8.2: Microwave implementation of quantum teleportation. The quantum teleportation protocol can be implemented with available microwave superconducting technology. The shared entanglement (EPR) is generated by combining squeezed states on a hybrid (HY). The joint measurement can be performed with coupling the input $|\Psi\rangle$ and half of the entangled pair on a HY following two quadrature measurements (QM1 and QM2). The receiver (Bob) stores his half of the entangled pair in a memory mechanical oscillator (MEM). After receiving the measurement outcomes from the sender, he displace his entangled state using directional couplers (DCs) to regenerate the input $|\Psi\rangle$.

shared entanglement and a higher detection efficiency. Thus our future direction towards demonstrating quantum teleportation will be to work on increasing the degree of entanglement and improving the measurement's quantum efficiency.

In our current demonstration, the entangled state is generated by combining a single squeezed state with vacuum, which results in a two-mode state only correlated in one quadrature. This simpler method reduces the amount of generated entanglement. The logical next step is to send two squeezed states to the hybrid to generate a two-mode state that is correlated in two orthogonal quadratures, hence having more entanglement.

Although our current entangler design allows us to combine two squeezed states on the hybrid, the cross coupling between the two TKCs prevents us from operating both SQs simultaneously. The nonlinear nature of the resonators makes it much more difficult to pump both TKCs properly to have parametric gains. Thus, it is important to design a next-generation entangler that has much less coupling between the two TKCs. Specifically, when both TKCs are on resonance at same frequency, the cross coupling rate needs to be smaller than the JPA bandwidth.

One possible coupling mechanism is coupling via a chip resonance mode. The entangler chip is 1.2 cm $\times$ 1.2 cm in size, and its top surface is mostly covered by superconducting niobium metal. Thus, the niobium top surface and the back metal ground plane can support parallel plate modes, which are in our working frequency range. Thus, to suppress the chip-mode coupling, we will design lumped-element passive components to be integrated with the lumped JPA. With a much smaller chip size, we will make frequencies of the chip modes out of the range we are interested in and expect to decrease the cross coupling between the two TKC resonators.

The pump cross coupling can also be caused by the reflections that occur at the interface between the chip and the circuit board. The entangler chip is electrically connected to the circuit board via wire bonds. These inductive wire bonds can cause approximately 10–20 dB reflections. Hence the pump of the TKC resonator can be reflected back and coupled to the other resonator via the hybrid. To improve the transmission at the interface, we will develop better interconnection techniques such as direct-contact launchers to the chip or flip-chip designs [135].

The detection efficiency of our quadrature measurements is limited by the losses of commercial microwave components and coaxial cables connecting them. Thus, one direction for improving the detection efficiency is to develop on-chip–low-loss components and integrate the tunable Kerr circuit with them on one chip. The biggest challenge of this strategy is the lack of on-chip circulators. Circulators, or isolators, usually rely on magnetic materials to achieve non-reciprocity and hence are incompatible with superconducting circuits. There are proposals of an on-chip circulator based on Josephson junction devices [136]. In our group, we are developing Josephson junction based circulators, where the nonreciprocity is achieved through time-varying reactances. Josephson junction arrays with time-varying flux, of the same type used in the JPA circuits, form the reactances.

Another problem of the on-chip design is caused by the significant reflections occurring at the wire bonds connecting the chip and the circuit board. These reflections can result in poor effective directivity of the coupler and decrease the performance of the JPA chip. To suppress this unwanted effect is one more motivation for developing better interconnections between the chip and the circuit board.

In addition to being able to generate a two-mode entangled state and perform efficient quadrature measurements, we want to develop the ability to delay or even store Bob's entangled mode while a waiting the information from Alice's measurements. This memory device could be a macroscopic mechanical oscillator that is compatible with superconducting quantum circuits. In our group, we have demonstrated that the state of an itinerant microwave field can be coherently transferred into, stored in, and retrieved from a mechanical oscillator [137]. Furthermore, the EPR entangled pair can be directly generated between an oscillator's phonons and microwave photons [138]. Thus, we can integrate this mechanical-oscillator memory with our entanglement generation and quadrature measurement apparatus to demonstrate quantum teleportation of propagating microwave fields.

Bibliography

[1] A. Einstein, B. Podolsky, and N. Rosen, "Can Quantum-Mechanical Description of Physical Reality Be Considered Complete?," Phys. Rev., vol. 47, pp. 777–780, May 1935.

[2] J. S. Bell, "On The Einstein Podolsky Rosen Paradox," Physics, vol. 1, no. 3, p. 195, 1964.

[3] M. A. Nielsen and I. L. Chuang, Quantum Computation and Quantum Information. New York: Cambridge University Press, 2010.

[4] S. L. Braunstein and P. van Loock, "Quantum information with continuous variables," Rev. Mod. Phys., vol. 77, pp. 513–577, June 2005.

[5] C. Weedbrook, S. Pirandola, R. García-Patrón, N. J. Cerf, T. C. Ralph, J. H. Shapiro, and S. Lloyd, "Gaussian quantum information," Rev. Mod. Phys., vol. 84, pp. 621–669, May 2012.

[6] A. K. Ekert, "Quantum cryptography based on Bells theorem," Phys. Rev. Lett., vol. 67, pp. 661–663, Aug. 1991.

[7] N. J. Cerf and P. Grangier, "From quantum cloning to quantum key distribution with continuous variables: a review (Invited)," J. Opt. Soc. Am. B, vol. 24, no. 2, p. 324, 2007.

[8] V. Scarani, H. Bechmann-Pasquinucci, N. Cerf, M. Dušek, N. Lütkenhaus, and M. Peev, "The security of practical quantum key distribution," Rev. Mod. Phys., vol. 81, pp. 1301–1350, Sept. 2009.

[9] C. H. Bennett and S. J. Wiesner, "Communication via one- and two-particle operators on Einstein-Podolsky-Rosen states," Phys. Rev. Lett., vol. 69, pp. 2881–2884, Nov. 1992.

[10] M. Ban, "Quantum dense coding via a two-mode squeezed-vacuum state," J. Opt. B Quantum Semiclassical Opt., vol. 1, pp. L9–L11, Dec. 1999.

[11] S. L. Braunstein and H. J. Kimble, "Dense coding for continuous variables," Phys. Rev. A, vol. 61, p. 042302, Mar. 2000.

[12] M. Żukowski, A. Zeilinger, M. Horne, and A. Ekert, "Event-ready-detectors Bell experiment via entanglement swapping," Phys. Rev. Lett., vol. 71, pp. 4287–4290, Dec. 1993.

[13] R. Polkinghorne and T. Ralph, "Continuous Variable Entanglement Swapping," Phys. Rev. Lett., vol. 83, pp. 2095–2099, Sept. 1999.

[14] S. Tan, "Confirming entanglement in continuous variable quantum teleportation," Phys. Rev. A, vol. 60, pp. 2752–2758, Oct. 1999.

[15] P. van Loock and S. L. Braunstein, "Unconditional teleportation of continuous-variable entanglement," Phys. Rev. A, vol. 61, p. 010302, Dec. 1999.

[16] C. H. Bennett, G. Brassard, C. Crépeau, R. Jozsa, A. Peres, and W. K. Wootters, "Teleporting an unknown quantum state via dual classical and Einstein-Podolsky-Rosen channels," Phys. Rev. Lett., vol. 70, pp. 1895–1899, Mar. 1993.

[17] L. Vaidman, "Teleportation of quantum states," Phys. Rev. A, vol. 49, pp. 1473–1476, Feb. 1994.

[18] S. L. Braunstein and H. J. Kimble, "Teleportation of Continuous Quantum Variables," Phys. Rev. Lett., vol. 80, pp. 869–872, Jan. 1998.

[19] P. W. Shor, "Scheme for reducing decoherence in quantum computer memory," Phys. Rev. A, vol. 52, pp. R2493–R2496, Oct. 1995.

[20] A. Steane, "Error Correcting Codes in Quantum Theory," Phys. Rev. Lett., vol. 77, pp. 793–797, July 1996.

[21] S. L. Braunstein, "Quantum error correction for communication with linear optics," Nature, vol. 394, pp. 47–49, July 1998.

[22] W. Dür and H.-J. Briegel, "Entanglement Purification for Quantum Computation," Phys. Rev. Lett., vol. 90, p. 067901, Feb. 2003.

[23] L. Jiang, J. Taylor, A. Sørensen, and M. Lukin, "Distributed quantum computation based on small quantum registers," Phys. Rev. A, vol. 76, p. 062323, Dec. 2007.

[24] M. Reid and P. Drummond, "Quantum Correlations of Phase in Nondegenerate Parametric Oscillation," Phys. Rev. Lett., vol. 60, pp. 2731–2733, June 1988.

[25] W. Louisell, A. Yariv, and A. Siegman, "Quantum Fluctuations and Noise in Parametric Processes. I.," Phys. Rev., vol. 124, pp. 1646–1654, Dec. 1961.

[26] J. Gordon, W. Louisell, and L. Walker, "Quantum Fluctuations and Noise in Parametric Processes. II," Phys. Rev., vol. 129, pp. 481–485, Jan. 1963.

[27] B. Mollow and R. Glauber, "Quantum Theory of Parametric Amplification. I," Phys. Rev., vol. 160, pp. 1076–1096, Aug. 1967.

[28] B. Mollow and R. Glauber, "Quantum Theory of Parametric Amplification. II," Phys. Rev., vol. 160, pp. 1097–1108, Aug. 1967.

[29] A. I. Lvovsky and M. G. Raymer, "Continuous-variable optical quantum-state tomography," Rev. Mod. Phys., vol. 81, pp. 299–332, Mar. 2009.

[30] R. Slusher, L. Hollberg, B. Yurke, J. Mertz, and J. Valley, "Observation of Squeezed States Generated by Four-Wave Mixing in an Optical Cavity," Phys. Rev. Lett., vol. 55, pp. 2409–2412, Nov. 1985.

[31] L.-A. Wu, H. Kimble, J. Hall, and H. Wu, "Generation of Squeezed States by Parametric Down Conversion," Phys. Rev. Lett., vol. 57, pp. 2520–2523, Nov. 1986.

[32] D. Smithey, M. Beck, M. Raymer, and A. Faridani, "Measurement of the Wigner distribution and the density matrix of a light mode using optical homodyne tomography: Application to squeezed states and the vacuum," Phys. Rev. Lett., vol. 70, pp. 1244–1247, Mar. 1993.

[33] S. Schiller, G. Breitenbach, S. Pereira, T. Müller, and J. Mlynek, "Quantum Statistics of the Squeezed Vacuum by Measurement of the Density Matrix in the Number State Representation," Phys. Rev. Lett., vol. 77, pp. 2933–2936, Sept. 1996.

[34] G. Breitenbach, S. Schiller, and J. Mlynek, "Measurement of the quantum states of squeezed light," Nature, vol. 387, pp. 471–475, May 1997.

[35] Z. Y. Ou, S. F. Pereira, H. J. Kimble, and K. C. Peng, "Realization of the Einstein-Podolsky-Rosen paradox for continuous variables," Phys. Rev. Lett., vol. 68, pp. 3663–3666, June 1992.

[36] C. Silberhorn, P. K. Lam, O. Weiß, F. König, N. Korolkova, and G. Leuchs, "Generation of Continuous Variable Einstein-Podolsky-Rosen Entanglement via the Kerr Nonlinearity in an Optical Fiber," Phys. Rev. Lett., vol. 86, pp. 4267–4270, May 2001.

[37] T. Eberle, V. Händchen, J. Duhme, T. Franz, R. F. Werner, and R. Schnabel, "Strong Einstein-Podolsky-Rosen entanglement from a single squeezed light source," Phys. Rev. A, vol. 83, p. 052329, May 2011.

[38] A. Furusawa, "Unconditional Quantum Teleportation," Science, vol. 282, pp. 706–709, Oct. 1998.

[39] H. Yonezawa, S. Braunstein, and A. Furusawa, "Experimental Demonstration of Quantum Teleportation of Broadband Squeezing," Phys. Rev. Lett., vol. 99, p. 110503, Sept. 2007.

[40] T. Aoki, G. Takahashi, T. Kajiya, J.-i. Yoshikawa, S. L. Braunstein, P. van Loock, and A. Furusawa, "Quantum error correction beyond qubits," Nat. Phys., vol. 5, pp. 541–546, June 2009.

[41] T. C. Zhang, K. W. Goh, C. W. Chou, P. Lodahl, and H. J. Kimble, "Quantum teleportation of light beams," Phys. Rev. A, vol. 67, p. 033802, Mar. 2003.

[42] M. Lassen, M. Sabuncu, A. Huck, J. Niset, G. Leuchs, N. J. Cerf, and U. L. Andersen, "Quantum optical coherence can survive photon losses using a continuous-variable quantum erasure-correcting code," Nat. Photonics, vol. 4, pp. 700–705, July 2010.

[43] B. Yurke, "Squeezed-state generation using a Josephson parametric amplifier," J. Opt. Soc. Am. B, vol. 4, p. 1551, Oct. 1987.

[44] B. Yurke, P. Kaminsky, R. Miller, E. Whittaker, A. Smith, A. Silver, and R. Simon, "Observation of 4.2-K equilibrium-noise squeezing via a Josephson-parametric amplifier," Phys. Rev. Lett., vol. 60, pp. 764–767, Feb. 1988.

[45] B. Yurke, L. Corruccini, P. Kaminsky, L. Rupp, A. Smith, A. Silver, R. Simon, and E. Whittaker, "Observation of parametric amplification and deamplification in a Josephson parametric amplifier," Phys. Rev. A, vol. 39, pp. 2519–2533, Mar. 1989.

[46] R. Movshovich, B. Yurke, P. Kaminsky, A. Smith, A. Silver, R. Simon, and M. Schneider, "Observation of zero-point noise squeezing via a Josephson-parametric amplifier," Phys. Rev. Lett., vol. 65, pp. 1419–1422, Sept. 1990.

[47] B. Josephson, "The discovery of tunnelling supercurrents," Rev. Mod. Phys., vol. 46, pp. 251–254, Apr. 1974.

[48] A. Wallraff, D. I. Schuster, A. Blais, L. Frunzio, R.-S. Huang, J. Majer, S. Kumar, S. M. Girvin, and R. J. Schoelkopf, "Strong coupling of a single photon to a superconducting qubit using circuit quantum electrodynamics.," Nature, vol. 431, pp. 162–7, Sept. 2004.

[49] A. A. Clerk, M. H. Devoret, S. M. Girvin, F. Marquardt, and R. J. Schoelkopf, "Introduction to quantum noise, measurement, and amplification," Rev. Mod. Phys., vol. 82, pp. 1155–1208, Apr. 2010.

[50] B. Yurke, M. L. Roukes, R. Movshovich, and A. N. Pargellis, "A low-noise series-array Josephson junction parametric amplifier," Appl. Phys. Lett., vol. 69, no. 20, p. 3078, 1996.

[51] I. Siddiqi, R. Vijay, F. Pierre, C. M. Wilson, M. Metcalfe, C. Rigetti, L. Frunzio, and M. H. Devoret, "RF-Driven Josephson Bifurcation Amplifier for Quantum Measurement," Phys. Rev. Lett., vol. 93, p. 207002, Nov. 2004.

[52] T. Yamamoto, K. Inomata, M. Watanabe, K. Matsuba, T. Miyazaki, W. D. Oliver, Y. Nakamura, and J. S. Tsai, "Flux-driven Josephson parametric amplifier," Appl. Phys. Lett., vol. 93, no. 4, p. 042510, 2008.

[53] M. A. Castellanos-Beltran, K. D. Irwin, G. C. Hilton, L. R. Vale, and K. W. Lehnert, "Amplification and squeezing of quantum noise with a tunable Josephson metamaterial," Nat. Phys., vol. 4, pp. 929–931, Oct. 2008.

[54] N. Roch, E. Flurin, F. Nguyen, P. Morfin, P. Campagne-Ibarcq, M. H. Devoret, and B. Huard, "Widely Tunable, Nondegenerate Three-Wave Mixing Microwave Device Operating near the Quantum Limit," Phys. Rev. Lett., vol. 108, p. 147701, Apr. 2012.

[55] A. Narla, K. M. Sliwa, M. Hatridge, S. Shankar, L. Frunzio, R. J. Schoelkopf, and M. H. Devoret, "Wireless Josephson amplifier," Appl. Phys. Lett., vol. 104, p. 232605, June 2014.

[56] J. Y. Mutus, T. C. White, R. Barends, Y. Chen, Z. Chen, B. Chiaro, A. Dunsworth, E. Jeffrey, J. Kelly, A. Megrant, C. Neill, P. J. J. O'Malley, P. Roushan, D. Sank, A. Vainsencher, J. Wenner, K. M. Sundqvist, A. N. Cleland, and J. M. Martinis, "Strong environmental coupling in a Josephson parametric amplifier," Appl. Phys. Lett., vol. 104, p. 263513, June 2014.

[57] F. Mallet, F. R. Ong, A. Palacios-Laloy, F. Nguyen, P. Bertet, D. Vion, and D. Esteve, "Single-shot qubit readout in circuit quantum electrodynamics," Nat. Phys., vol. 5, pp. 791–795, Sept. 2009.

[58] B. Abdo, F. Schackert, M. Hatridge, C. Rigetti, and M. Devoret, "Josephson amplifier for qubit readout," Appl. Phys. Lett., vol. 99, no. 16, p. 162506, 2011.

[59] D. Ristè, J. G. van Leeuwen, H. S. Ku, K. W. Lehnert, and L. DiCarlo, "Initialization by Measurement of a Superconducting Quantum Bit Circuit," Phys. Rev. Lett., vol. 109, p. 050507, Aug. 2012.

[60] Z. R. Lin, K. Inomata, W. D. Oliver, K. Koshino, Y. Nakamura, J. S. Tsai, and T. Yamamoto, "Single-shot readout of a superconducting flux qubit with a flux-driven Josephson parametric amplifier," Appl. Phys. Lett., vol. 103, no. 13, p. 132602, 2013.

[61] K. W. Murch, S. J. Weber, C. Macklin, and I. Siddiqi, "Observing single quantum trajectories of a superconducting quantum bit.," Nature, vol. 502, pp. 211–4, Oct. 2013.

[62] E. A. Sete, A. Galiautdinov, E. Mlinar, J. M. Martinis, and A. N. Korotkov, "Catch-Disperse-Release Readout for Superconducting Qubits," Phys. Rev. Lett., vol. 110, p. 210501, May 2013.

[63] C. A. Regal, J. D. Teufel, and K. W. Lehnert, "Measuring nanomechanical motion with a microwave cavity interferometer," Nat. Phys., vol. 4, pp. 555–560, May 2008.

[64] J. D. Teufel, T. Donner, M. A. Castellanos-Beltran, J. W. Harlow, and K. W. Lehnert, "Nanomechanical motion measured with an imprecision below that at the standard quantum limit.," Nat. Nanotechnol., vol. 4, pp. 820–3, Dec. 2009.

[65] J. D. Teufel, T. Donner, D. Li, J. W. Harlow, M. S. Allman, K. Cicak, A. J. Sirois, J. D. Whittaker, K. W. Lehnert, and R. W. Simmonds, "Sideband cooling of micromechanical motion to the quantum ground state.," Nature, vol. 475, pp. 359–63, July 2011.

[66] M. Hatridge, R. Vijay, D. H. Slichter, J. Clarke, and I. Siddiqi, "Dispersive magnetometry with a quantum limited SQUID parametric amplifier," Phys. Rev. B, vol. 83, p. 134501, Apr. 2011.

[67] E. M. Levenson-Falk, R. Vijay, N. Antler, and I. Siddiqi, "A dispersive nanoSQUID magnetometer for ultra-low noise, high bandwidth flux detection," Supercond. Sci. Technol., vol. 26, p. 055015, May 2013.

[68] D. Ristè, C. C. Bultink, K. W. Lehnert, and L. DiCarlo, "Feedback Control of a Solid-State Qubit Using High-Fidelity Projective Measurement," Phys. Rev. Lett., vol. 109, p. 240502, Dec. 2012.

[69] R. Vijay, C. Macklin, D. H. Slichter, S. J. Weber, K. W. Murch, R. Naik, A. N. Korotkov, and I. Siddiqi, "Stabilizing Rabi oscillations in a superconducting qubit using quantum feedback.," Nature, vol. 490, pp. 77–80, Oct. 2012.

[70] D. Ristè, M. Dukalski, C. A. Watson, G. de Lange, M. J. Tiggelman, Y. M. Blanter, K. W. Lehnert, R. N. Schouten, and L. DiCarlo, "Deterministic entanglement of superconducting qubits by parity measurement and feedback.," Nature, vol. 502, pp. 350–4, Oct. 2013.

[71] J. Kerckhoff, R. W. Andrews, H. S. Ku, W. F. Kindel, K. Cicak, R. W. Simmonds, and K. W. Lehnert, "Tunable Coupling to a Mechanical Oscillator Circuit Using a Coherent Feedback Network," Phys. Rev. X, vol. 3, p. 021013, June 2013.

[72] C. Bockstiegel, J. Gao, M. R. Vissers, M. Sandberg, S. Chaudhuri, A. Sanders, L. R. Vale, K. D. Irwin, and D. P. Pappas, "Development of a Broadband NbTiN Traveling Wave Parametric Amplifier for MKID Readout," J. Low Temp. Phys., vol. 176, pp. 476–482, Jan. 2014.

[73] T. M. Shokair, J. Root, K. A. Van Bibber, B. Brubaker, Y. V. Gurevich, S. B. Cahn, S. K. Lamoreaux, M. A. Anil, K. W. Lehnert, B. K. Mitchell, A. Reed, and G. Carosi, "Future directions in the microwave cavity search for dark matter axions," Int. J. Mod. Phys. A, vol. 29, p. 1443004, July 2014.

[74] C. Eichler, D. Bozyigit, C. Lang, M. Baur, L. Steffen, J. M. Fink, S. Filipp, and A. Wallraff, "Observation of Two-Mode Squeezing in the Microwave Frequency Domain," Phys. Rev. Lett., vol. 107, p. 113601, Sept. 2011.

[75] E. Flurin, N. Roch, F. Mallet, M. H. Devoret, and B. Huard, "Generating Entangled Microwave Radiation Over Two Transmission Lines," Phys. Rev. Lett., vol. 109, p. 183901, Oct. 2012.

[76] E. P. Menzel, R. Di Candia, F. Deppe, P. Eder, L. Zhong, M. Ihmig, M. Haeberlein, A. Baust, E. Hoffmann, D. Ballester, K. Inomata, T. Yamamoto, Y. Nakamura, E. Solano, A. Marx, and R. Gross, "Path Entanglement of Continuous-Variable Quantum Microwaves," Phys. Rev. Lett., vol. 109, p. 250502, Dec. 2012.

[77] C. Eichler, C. Lang, J. M. Fink, J. Govenius, S. Filipp, and A. Wallraff, "Observation of Entanglement between Itinerant Microwave Photons and a Superconducting Qubit," Phys. Rev. Lett., vol. 109, p. 240501, Dec. 2012.

[78] C. Lang, C. Eichler, L. Steffen, J. M. Fink, M. J. Woolley, A. Blais, and A. Wallraff, "Correlations, indistinguishability and entanglement in HongOuMandel experiments at microwave frequencies," Nat. Phys., vol. 9, pp. 345–348, May 2013.

[79] H. Paik, D. I. Schuster, L. S. Bishop, G. Kirchmair, G. Catelani, A. P. Sears, B. R. Johnson, M. J. Reagor, L. Frunzio, L. I. Glazman, S. M. Girvin, M. H. Devoret, and R. J. Schoelkopf, "Observation of High Coherence in Josephson Junction Qubits Measured in a Three-Dimensional Circuit QED Architecture," Phys. Rev. Lett., vol. 107, p. 240501, Dec. 2011.

[80] E. P. Menzel, F. Deppe, M. Mariantoni, M. A. Araque Caballero, A. Baust, T. Niemczyk, E. Hoffmann, A. Marx, E. Solano, and R. Gross, "Dual-Path State Reconstruction Scheme for Propagating Quantum Microwaves and Detector Noise Tomography," Phys. Rev. Lett., vol. 105, p. 100401, Aug. 2010.

[81] M. Mariantoni, E. P. Menzel, F. Deppe, M. A. Araque Caballero, A. Baust, T. Niemczyk, E. Hoffmann, E. Solano, A. Marx, and R. Gross, "Planck Spectroscopy and Quantum Noise of Microwave Beam Splitters," Phys. Rev. Lett., vol. 105, p. 133601, Sept. 2010.

[82] D. Bozyigit, C. Lang, L. Steffen, J. M. Fink, C. Eichler, M. Baur, R. Bianchetti, P. J. Leek, S. Filipp, M. P. da Silva, A. Blais, and A. Wallraff, "Antibunching of microwave-frequency photons observed in correlation measurements using linear detectors," Nat. Phys., vol. 7, pp. 154–158, Dec. 2010.

[83] M. P. da Silva, D. Bozyigit, A. Wallraff, and A. Blais, "Schemes for the observation of photon correlation functions in circuit QED with linear detectors," Phys. Rev. A, vol. 82, p. 043804, Oct. 2010.

[84] C. Eichler, D. Bozyigit, and A. Wallraff, "Characterizing quantum microwave radiation and its entanglement with superconducting qubits using linear detectors," Phys. Rev. A, vol. 86, p. 032106, Sept. 2012.

[85] S. L. Braunstein, C. A. Fuchs, H. J. Kimble, and P. van Loock, "Quantum versus classical domains for teleportation with continuous variables," Phys. Rev. A, vol. 64, p. 022321, July 2001.

[86] L.-M. Duan, G. Giedke, J. I. Cirac, and P. Zoller, "Inseparability Criterion for Continuous Variable Systems," Phys. Rev. Lett., vol. 84, pp. 2722–2725, Mar. 2000.

[87] R. Simon, "Peres-Horodecki Separability Criterion for Continuous Variable Systems," Phys. Rev. Lett., vol. 84, pp. 2726–2729, Mar. 2000.

[88] G. Adesso, A. Serafini, and F. Illuminati, "Extremal entanglement and mixedness in continuous variable systems," Phys. Rev. A, vol. 70, p. 022318, Aug. 2004.

[89] F. Mallet, M. A. Castellanos-Beltran, H. S. Ku, S. Glancy, E. Knill, K. D. Irwin, G. C. Hilton, L. R. Vale, and K. W. Lehnert, "Quantum State Tomography of an Itinerant Squeezed Microwave Field," Phys. Rev. Lett., vol. 106, p. 220502, June 2011.

[90] H. S. Ku, F. Mallet, L. R. Vale, K. D. Irwin, S. E. Russek, G. C. Hilton, and K. W. Lehnert, "Design and Testing of Superconducting Microwave Passive Components for Quantum Information Processing," IEEE Trans. Appl. Supercond., vol. 21, pp. 452–455, June 2011.

[91] H. S. Ku, W. F. Kindel, F. Mallet, S. Glancy, K. D. Irwin, G. C. Hilton, L. R. Vale, and K. W. Lehnert, "Generating and verifying entangled itinerant microwave fields with efficient and independent measurements," Submitted to Phys. Rev. A.

[92] C. Gerry and P. Knight, Introductory Quantum Optics. Cambridge: Cambridge University Press, 2005.

[93] Y.-F. Chen, D. Hover, S. Sendelbach, L. Maurer, S. T. Merkel, E. J. Pritchett, F. K. Wilhelm, and R. McDermott, "Microwave Photon Counter Based on Josephson Junctions," Phys. Rev. Lett., vol. 107, p. 217401, Nov. 2011.

[94] R. Glauber, "Coherent and Incoherent States of the Radiation Field," Phys. Rev., vol. 131, pp. 2766–2788, Sept. 1963.

[95] J. Klauder and B. Skagerstam, Coherent States: Applications in Physics and Mathematical Physics. Singapore: World Scientific, 1985.

[96] W.-M. Zhang, D. H. Feng, and R. Gilmore, "Coherent states: Theory and some applications," Rev. Mod. Phys., vol. 62, pp. 867–927, Oct. 1990.

[97] Y. Yamamoto and H. A. Haus, "Preparation, measurement and information capacity of optical quantum states," Rev. Mod. Phys., vol. 58, pp. 1001–1020, Oct. 1986.

[98] R. Slusher and B. Yurke, "Squeezed light for coherent communications," J. Light. Technol., vol. 8, pp. 466–477, Mar. 1990.

[99] C. Caves, "Quantum-mechanical noise in an interferometer," Phys. Rev. D, vol. 23, pp. 1693–1708, Apr. 1981.

[100] E. Wigner, "On the Quantum Correction For Thermodynamic Equilibrium," Phys. Rev., vol. 40, pp. 749–759, June 1932.

[101] U. Leonhardt, Measuring the Quantum State of Light, vol. 24. Cambridge: Cambridge University Press, 2005.

[102] H. Weyl, The Theory of Groups and Quantum Mechanics. New York: Courier Dover Publications, 1950.

[103] N. N. Bogoliubov, "On the Theory of Superfluidity," J. Phys., vol. 11, p. 23, 1947.

[104] M. S. Kim, W. Son, V. Bužek, and P. L. Knight, "Entanglement by a beam splitter: Nonclassicality as a prerequisite for entanglement," Phys. Rev. A, vol. 65, p. 032323, Feb. 2002.

[105] D. Walls, Quantum Optics. Berlin: Springer Science & Business Media, 2008.

[106] R. Werner, "Quantum states with Einstein-Podolsky-Rosen correlations admitting a hidden-variable model," Phys. Rev. A, vol. 40, pp. 4277–4281, Oct. 1989.

[107] G. Vidal and R. Werner, "Computable measure of entanglement," Phys. Rev. A, vol. 65, p. 032314, Feb. 2002.

[108] A. Peres, "Separability Criterion for Density Matrices," Phys. Rev. Lett., vol. 77, pp. 1413–1415, Aug. 1996.

[109] B. Josephson, "Possible new effects in superconductive tunnelling," Phys. Lett., vol. 1, pp. 251–253, July 1962.

[110] T. V. Duzer and C. W. Turner, Principles of Superconductive Devices and Circuits. Upper Saddle River: Prentice Hall, 1999.

[111] W. H. Louisell, Radiation and Noise in Quantum Electronics. New York: McGraw Hill, 1964.

[112] B. Yurke and J. Denker, "Quantum network theory," Phys. Rev. A, vol. 29, pp. 1419–1437, Mar. 1984.

[113] S. Renaud, E. Giacobino, and J. Zinn-Justin, Fluctuations Quantiques: Les Houches, Session LXIII. Amsterdam: Elsevier, 1997.

[114] B. Yurke and E. Buks, "Performance of Cavity-Parametric Amplifiers, Employing Kerr Nonlinearites, in the Presence of Two-Photon Loss," J. Light. Technol., vol. 24, pp. 5054–5066, Dec. 2006.

[115] C. Gardiner and M. Collett, "Input and output in damped quantum systems: Quantum stochastic differential equations and the master equation," Phys. Rev. A, vol. 31, pp. 3761–3774, June 1985.

[116] C. Wen, "Coplanar-Waveguide Directional Couplers," IEEE Trans. Microw. Theory Tech., vol. 18, pp. 318–322, June 1970.

[117] C.-H. Ho, L. Fan, and K. Chang, "Broad-band uniplanar hybrid-ring and branch-line couplers," IEEE Trans. Microw. Theory Tech., vol. 41, no. 12, pp. 2116–2125, 1993.

[118] R. N. Simons, Coplanar Waveguide Circuits, Components, and Systems. New York: John Wiley & Sons, 2004.

[119] I. Wolff, Coplanar Microwave Integrated Circuits. Hoboken: John Wiley & Sons, 2006.

[120] D. M. Pozar, Microwave Engineering, 4th Edition, vol. 4. Hoboken: John Wiley & Sons, 2011.

[121] T. Weller, R. Henderson, S. Robertson, and L. Katehi, "Optimization of MM-wave distribution networks using silicon-based CPW," in 1998 IEEE MTT-S Int. Microw. Symp. Dig. (Cat. No.98CH36192), vol. 2, pp. 537–540, IEEE, 1998.

[122] J. Sauvageau, C. Burroughs, P. Booi, M. Cromar, R. Benz, and J. Koch, "Superconducting integrated circuit fabrication with low temperature ECR-based PECVD SiO/sub 2/ dielectric films," IEEE Trans. Appiled Supercond., vol. 5, pp. 2303–2309, June 1995.

[123] G. Engen and C. Hoer, "Thru-Reflect-Line: An Improved Technique for Calibrating the Dual Six-Port Automatic Network Analyzer," IEEE Trans. Microw. Theory Tech., vol. 27, pp. 987–993, Dec. 1979.

[124] B. A. Mazin, Microwave Kinetic Inductance Detectors. PhD thesis, California Institute of Technology, 2004.

[125] M. A. Castellanos-Beltran, Development of a Josephson Parametric Amplifier for the Prepar-ation and Detection of Nonclassical States of Microwave Fields. PhD thesis, University of Colorado, 2010.

[126] V. Manucharyan, E. Boaknin, M. Metcalfe, R. Vijay, I. Siddiqi, and M. Devoret, "Microwave bifurcation of a Josephson junction: Embedding-circuit requirements," Phys. Rev. B, vol. 76, p. 014524, July 2007.

[127] J. A. B. Mates, G. C. Hilton, K. D. Irwin, L. R. Vale, and K. W. Lehnert, "Demonstration of a multiplexer of dissipationless superconducting quantum interference devices," Appl. Phys. Lett., vol. 92, no. 2, p. 023514, 2008.

[128] U. Leonhardt and H. Paul, "High-Accuracy Optical Homodyne Detection with Low-Efficiency Detectors: "Preamplification" from Antisqueezing," Phys. Rev. Lett., vol. 72, pp. 4086–4089, June 1994.

[129] M. A. Castellanos-Beltran and K. W. Lehnert, "Widely tunable parametric amplifier based on a superconducting quantum interference device array resonator," Appl. Phys. Lett., vol. 91, no. 8, p. 083509, 2007.

[130] M. A. Castellanos-Beltran, K. D. Irwin, L. R. Vale, G. C. Hilton, and K. W. Lehnert, "Bandwidth and Dynamic Range of a Widely Tunable Josephson Parametric Amplifier," IEEE Trans. Appl. Supercond., vol. 19, pp. 944–947, June 2009.

[131] U. Leonhardt and H. Paul, "Realistic optical homodyne measurements and quasiprobability distributions," Phys. Rev. A, vol. 48, pp. 4598–4604, Dec. 1993.

[132] M. Paris and J. Řeháček, eds., Quantum State Estimation, vol. 649 of Lecture Notes in Physics. Berlin, Heidelberg: Springer Berlin Heidelberg, 2004.

[133] S. Glancy, Innovations in Maximum Likelihood Quantum State Tomography. PIRSA - Perim. Inst. Rec. Semin. Arch., 2009.

[134] R. Simon, N. Mukunda, and B. Dutta, "Quantum-noise matrix for multimode systems: U(n) invariance, squeezing, and normal forms," Phys. Rev. A, vol. 49, pp. 1567–1583, Mar. 1994.

[135] C. Schaffauser and C. Drevon, Flip Chip for microwave applications. Alcatel Space, 2005.

[136] A. Kamal, J. Clarke, and M. H. Devoret, "Noiseless non-reciprocity in a parametric active device," Nat. Phys., vol. 7, pp. 311–315, Jan. 2011.

[137] T. A. Palomaki, J. W. Harlow, J. D. Teufel, R. W. Simmonds, and K. W. Lehnert, "Coherent state transfer between itinerant microwave fields and a mechanical oscillator.," Nature, vol. 495, pp. 210–4, Mar. 2013.

[138] T. A. Palomaki, J. D. Teufel, R. W. Simmonds, and K. W. Lehnert, "Entangling mechanical motion with microwave fields.," Science, vol. 342, pp. 710–3, Nov. 2013.

[139] J. Řeháček, S. Olivares, D. Mogilevtsev, Z. Hradil, M. Paris, S. Fornaro, V. DAuria, A. Porzio, and S. Solimeno, "Effective method to estimate multidimensional Gaussian states," Phys. Rev. A, vol. 79, p. 032111, Mar. 2009.

Appendix A

Gaussian state estimation

As a check for systematic errors, we implemented a second method to estimate the quantum state produced in this experiment. We call this method "Gaussian state estimation", because its range is all two-mode states that have Gaussian Wigner functions. As inputs, the method accepts the calibrated quadrature measurements $W_i(\theta_i)$ for $i = 1, 2$ and returns the Gaussian state's vector of quadrature expected values $\mu = (\mu_{x1}, \mu_{y1}, \mu_{x2}, \mu_{y2})^T = \mathrm{E}[(X_1, Y_1, X_2, Y_2)^T]$, where $\mathrm{E}[x]$ is the expectation value of x. and the covariance matrix Σ whose elements are the covariances between the random variables $(X_1, Y_1, X_2, Y_2)^T$. We will label the elements of Σ with subscripts indicating the quadrature variable and mode: $\Sigma_{ai,bj}$, where a and $b \in \{x, y\}$ and i and $j \in \{1, 2\}$. Note that the Gaussian state estimation requires the use of the squeezer model described in Sec. 7.2.2 to produce correctly calibrated quadrature measurements. The data set consists of the n instances of the quadruplet containing two phases and two quadrature measurements: $\{(\theta_1^{(k)}, W_1^{(k)}, \theta_2^{(k)}, W_2^{(k)}) | k = 1, ..., n\}$ in which k labels the measurement instance. Although in the experiment θ_1 and θ_2 are scanned continuously and quadratures are measured at regular intervals, in this section we treat the phases as random variables uniformly distributed over $[0, 2\pi)$ with a probability distribution of $P(\theta_i) = 1/(2\pi)$.

Consider the expected value

$$\mathrm{E}[W_i \cos\theta_i] = \mathrm{E}[(X_i \cos\theta_i + Y_i \sin\theta_i) \cos\theta_i].$$

Because θ_i is independent of X_i and Y_i,

$$\begin{aligned}
\mathrm{E}[W_i \cos\theta_i] &= \mathrm{E}[\mu_{xi}\cos^2\theta_i + \mu_{yi}\sin\theta_i\cos\theta_i] \\
&= \int_0^{2\pi} \left(\mu_{xi}\cos^2\theta_i + \mu_{yi}\sin\theta_i\cos\theta_i\right) P(\theta)\mathrm{d}\theta \\
&= \mu_{xi}/2.
\end{aligned}$$

By the Law of Large Numbers, we can estimate μ_{xi} with

$$\widehat{\mu_{xi}} = 2\overline{W_i\cos\theta_i} = \frac{1}{n}\sum_{k=1}^{n} W_i^{(k)}\cos\theta_i^{(k)},$$

where we use the hat to denote the estimate of a parameter and the overline to denote the sample mean. Similarly, we can estimate μ_{yi} with $\widehat{\mu_{yi}} = 2\overline{W_i\sin\theta_i}$. Applying this treatment to both modes gives us $\widehat{\mu}$.

To estimate Σ, consider the expected value

$$\mathrm{E}[W_i^2\cos^2\theta_i] = \mathrm{E}[(X_i\cos\theta_i + Y_i\sin\theta_i)^2\cos^2\theta_i].$$

Using the independence of θ_i from X_i and P_i and the uniformity of $P(\theta_i)$, we obtain

$$\begin{aligned}
\mathrm{E}[W_i^2\cos^2\theta_i] &= \mathrm{E}\left[\frac{1}{8}(3X_i^2 + P_i^2)\right] \\
&= \frac{1}{8}(3\mu_{xi}^2 + \Sigma_{xi,xi} + \mu_{yi}^2 + \Sigma_{yi,yi}).
\end{aligned}$$

One can similarly show that

$$\mathrm{E}[W_i^2\sin^2\theta_i] = \frac{1}{8}(\mu_{xi}^2 + \Sigma xi, xi + 3\mu_{yi}^2 + 3\Sigma_{yi,yi}),$$

and

$$\mathrm{E}[W_i^2\cos\theta_i\sin\theta_i] = \frac{1}{4}(\mu_{xi}\mu_{yi} + \Sigma_{xi,yi}).$$

Solving these three equations for the elements of Σ and applying the Law of Large Numbers gives us the estimates

$$\begin{aligned}
\widehat{\Sigma_{xi,xi}} &= 3\overline{W_i^2\cos^2\theta_i} - \overline{W_i^2\sin^2\theta_i} - \widehat{\mu_{xi}}^2, \\
\widehat{\Sigma_{yi,yi}} &= 3\overline{W_i^2\sin^2\theta_i} - \overline{W_i^2\cos^2\theta_i} - \widehat{\mu_{yi}}^2, \\
\widehat{\Sigma_{xi,yi}} &= 4\overline{W_i^2\cos\theta_i\sin\theta_i} - \widehat{\mu_{xi}}\widehat{\mu_{yi}}.
\end{aligned}$$

Estimates for the cross-mode elements of Σ are given by

$$\begin{aligned}
\widehat{\Sigma_{x1,x2}} &= 4\overline{W_1 \cos\theta_1 W_2 \cos\theta_2} - \widehat{\mu_{x1}\mu_{x2}}, \\
\widehat{\Sigma_{x1,y2}} &= 4\overline{W_1 \cos\theta_1 W_2 \sin\theta_2} - \widehat{\mu_{x1}\mu_{y2}}, \\
\widehat{\Sigma_{y1,x2}} &= 4\overline{W_1 \sin\theta_1 W_2 \cos\theta_2} - \widehat{\mu_{y1}\mu_{x2}}, \\
\widehat{\Sigma_{y1,y2}} &= 4\overline{W_1 \sin\theta_1 W_2 \sin\theta_2} - \widehat{\mu_{y1}\mu_{y2}}.
\end{aligned}$$

Thus, we estimate the expected values μ and covariance matrix Σ by computing sample means of simple functions of the quadrature and phase measurements. Because the computation is so simple, our method is well suited for large data sets. The maximum-likelihood method developed by Řeháček and co-authors might give lower statistical uncertainty at the cost of greater computation time [139]. Our method does not impose a constraint on Σ to enforce the Heisenberg Uncertainty Principle [134]. Although it is possible for the estimate to be unphysical, all states found in our analysis are valid quantum states.